NMAMIT

NITTE

Annual Research Journal

Volume 5 October 2015 ISSN 2249-0426

Published by:
NMAM Institute of Technology
Nitte - 574 110
www.research.nitte.edu.in

EDITORIAL

The research at higher technical Institutions in India used to be the preserve of IITs. However, it is slowly and steadily entering the portals of tier 3 and lesser known institutions in the form of producing Ph.Ds. But, for the research to take firm hold in smaller Institutions, research beyond Ph.D must happen. For that, the departments must be staffed with number of faculty members more than the current AICTE requirement. That way there is less teaching/lab load on the faculty members and they can devout more time to research. I do foresee a scenario where in the faculty members are required to carry out research which has relevance to the societal problems, unlike just producing few research publications. Days are not too far off when the career advancement in higher technical Institutions will be mainly based on research related performance. It will not be wishful thinking if faculty members will be asked to generate income for themselves by way of carrying out consultancy for which they need to equip themselves well and be more relevant which is possible by carrying out research keeping in view the problems of the society. I am happy to note that couple of papers published in this journal respond to these requirements. I thank all the authors for their contribution. Happy and prosperous New Year 2015.

Dr. Sudesh Bekal
Editor

NMAMIT

Annual Research Journal

Volume 5

October 2015

ISSN 2249-0426

Published by:

NMAM Institute of Technology

An Autonomous Institution Under VTU, Belgaum

(A Unit of Nitte Education Trust)

NITTE - 574 110, UDUPI DIST., KARNATAKA

www.nitte.edu.in/nmamit

NMAMIT Annual Research Journal Volume No. 5

October 2015

ISSN : 2249-0426

Published by :

NMAM Institute of Technology

Nitte, 574 110

Udupi district, Karnataka State, India

Printed by :

Praveena Mudrana

Karkala 574104,

Udupi district, Karnataka State

email: praveenamudrana@gmail.com

Heavy metals remediation in stale foundry effluent with Activated Charcoal-250

[*a]Samson Ojoawo, [b]Rajan Kumar, [b]Vashisth Kumar, [b]Prasadh Hallur and [b]Vikash H.V

[a]*Department of Civil Engineering,*
Ladoke Akintola University of Technology, P.M.B 4000,
Ogbomoso, Nigeria
soojoawo@lautech.edu.ng

[b]*Department of Civil Engineering,*
NMAM Institute of Technology, Nitte-574110, Udupi District,
Karnataka, India

Abstract

The menace of wastewater pollution in the 21st century is becoming alarming. Application of the low-cost adsorbents for wastewater treatment has received more attention this moment in environmental history than never. Therefore, remediating stale foundry wastewater with Activated Carbon, AC-250 is the focus of this study.

Wastewater samples were collected from Lamina Foundry, Nitte, Karnataka State, India and were subjected to Atomic Absorption Spectrophotometry (AAS) analysis. The analysis identified the prominent heavy metals (Zn, Cu, Mg, and Pb) present in the stale foundry effluent, determined their respective concentrations and treated them using the commercially sourced activated charcoal, AC-250. Effects of four (4) factors viz: adsorbent dosage, contact time, stirring speed and pH on the adsorption process during the wastewater treatment were studied. Optimum conditions required for the most efficient treatment of the wastewater and the treatment cost estimates were determined.

The AC-250 is found as efficient in adsorption of the heavy metals from foundry wastewater. In some of the cases a 100% removal is possible, especially with Pb. The analysis of the major experiments on effects of adsorbent dosage, contact time rotating speed and pH on the adsorption process, gave the optimum conditions for removal under which the most efficient treatment of the wastewater containing studied heavy metals was possible. For the optimum treatment conditions, an adsorbent dosage of 1 g, a contact time of 120 minutes, a rotating/agitation speed of 350 rpm and a pH value of 6 are established. An average cost of treating 1 litre of stale foundry wastewater is Rs 23 or 0.4 USD.

This study therefore recommends AC-250 as an efficient adsorbent at the given optimum conditions for stale foundry wastewater. The reuse of AC-250 via the process of thermal reactivation at 800^0C is encouraged as a means of waste management.

Keywords: Activated Carbon-250, remediation, wastewater, heavy metals

1.0 Introduction

Discharging industrial wastewater containing different pollutants can lead to the contamination of environment and disorder in its ecosystem. Increment and development of the alloy and leather industries, metal galvanizations, laundries, electroplating firms, all result in significant increase of heavy metals ion concentration in the industrial wastewater. Accumulation of these metals ion in human body can lead to severe disorders in the performance of kidneys, liver, sexual organs, brain and nervous systems. Direct discharge of wastewater containing heavy metals into municipal waste water collection system can equally damage biological treatment units and produce active sludge which in turn can destroy the agricultural products. Since heavy metals are non-biodegradable, they are stored in the living tissues and enter the food chain of plants, animals and human beings. Therefore with regard to the numerous disadvantages of heavy metals, their removal from industrial wastewater is an essential environmental requirement.

In recent times, efforts have been made to employ cheaper and more effective organic materials, agricultural wastes, and related compounds as adsorbents [1]. Activated Carbon (AC) is one of the most applicable adsorbents in common use for wastewater treatment processes since 1883. AC, also called activated charcoal, activated coal, or *carbo activatus*, is a form of carbon processed to have small, low-volume pores that increase the surface area available for adsorption or chemical reaction [2]. AC is usually derived from charcoal and high-porosity bio-char. Due to its high degree of micro porosity, just one gram of activated carbon has a surface area in excess of 500 m^2, as determined by gas adsorption. An activation level sufficient for useful application may be attained solely from high surface area; however, further chemical treatment often enhances adsorption properties. AC is used as an appropriate adsorbent in removing different pollutants, particularly heavy metals.

Activated charcoal is good at trapping other carbon-based impurities as well as things like chlorine. Many other chemicals are not attracted to carbon at all sodium, nitrates, etc., so they pass right through. This means that an activated charcoal filter will remove certain impurities while ignoring others [3]. Nowadays, activated carbon finds wide application in the treatment of wastewater generated from industries such as food, textile, chemical, pharmaceutical, pesticides and herbicides production, coke plant, munitions factories, petroleum refineries and storage installations, organic pigments and dyes, mineral processing plants, insecticides, pesticides, resins, detergents, explosives, and dyestuffs. It is also employed in the treatment of sanitary and hazardous landfill leachates [4].

This study identified the heavy metals present in the stale foundry effluent, determined their respective amounts and treated them using the commercially sourced activated charcoal, AC-250. Also examined were the effects of various factors such as adsorbent dosage, contact time, stirring speed and pH on the adsorption process during the treatment of the wastewater. And finally it established the optimum conditions required for the most efficient treatment of the wastewater. The sampling station was the outlet sump of the Lamina Foundry, Nitte, Karnataka State, India. The effluent was kept at room temperature for 4 weeks before the commencement of the study to ensure it was stale.

2.0 Methodology

(a) AAS analysis for initial concentration of foundry effluent: The untreated Lamina Foundry effluent sample was subjected to AAS (Atomic Absorption Spectroscopy) analysis conducted in the Flame atomic absorption spectroscope of the Department of Biotechnology Engineering, NMAM Institute of Technology, Nitte, Karnataka State, India. The AAS experiment on the untreated lamina foundry effluent gave information regarding the heavy metals present in them and their amount.

Figure 1: AAS Analysis of the untreated Effluent

3.0 One-factor-at-a-time (OFAT) treatment experiments: The effluent was treated using the purified AC. Four different types of experiments were conducted in order to determine the effect of contact time, pH, adsorbent dosage and rotating/stirring speed on the adsorption of heavy metals by the AC-250.

(i) Experimental study of the adsorbent dosage effect on the treatment process: Five conical flasks of 100ml volume were taken and were labelled from 1 to 5.Then in each of the flasks 50ml of the untreated foundry effluent were put. After this 0.2, 0.4, 0.6, 0.8 and 1.0 g of the AC were added to the 5 respective conical flasks.

Figure 2. Foundry effluent being treated with different adsorbent dosages

The flasks were then placed in a rotary incubator shaker and agitated at a speed of 150 rpm for 1 hour at a room temperature of 32^0C. The filtrate from each flask was collected in a test tube and the mouth of the test tube and subjected to AAS analysis.

Figure 3. Foundry effluent being rotated at 150 rpm in mechanical shaker

(ii) Experimental study of the contact time effect on the treatment process:

Six conical flasks had 50 ml of the untreated foundry effluent added to each of them, and with 0.2g of AC-250. The flasks were placed in a mechanical shaker one after the other and were agitated at 150 rpm for different selected contact times of 20, 40, 60, 80, 100 and 120 min. The filtrate from the content of each flask was collected and subjected to AAS analysis.

(iii) Experimental study of the rotating speed effect on the treatment process:

1 g each of the AC was added 5 conical flasks of 50 ml wastewater. The conical flasks were placed in a mechanical shaker in turns and rotated at the desired speed ranging from 150 to 350 rpm.

Figure 4: Foundry effluent being rotated at different speed

(iv) Experimental study of pH effect on the treatment process:

The effect of pH on the adsorption of metal ions was studied over a pH range of 2 to 6. Three conical flasks were filled with 50 ml of the untreated foundry effluent. 1 g of the AC-250 was added to each of them. The pH of the contents in the three conical flasks was adjusted and maintained at 2, 4 and 6 respectively. The flasks contents were agitated in a mechanical shaker at 150 rpm for an hour. The filtrate of each flask was then subjected to AAS analysis.

3.0. Results and Discusion

The results of laboratory experiments/analyses are as presented and discussed below:

(a) Untreated foundry effluent:

The AAS analysis conducted on the untreated Lamina foundry effluent showed the presence of Zn, Cu, Mg and Pb. The concentration levels of these metals obtained are presented in Table 1. Figure 5 shows that Mg is dominant while the presence of Pb is at the minimum level.

Table 1: Concentration levels of the heavy metals in untreated wastewater

Metals	*Zn*	*Cu*	*Mg*	*Pb*
Concentration (mg/L)	0.552	1.283	2.647	0.068

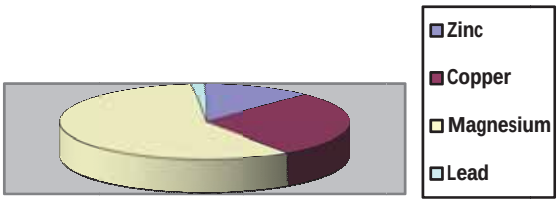

Figure 5: Representation of the heavy metals in the untreated wastewater

(b) Adsorption study on the wastewater

Table 2 and Figure 6 contain the results and graphical representation respectively, of the adsorption.

In all the dosage concentrations Cu was totally adsorbed by AC-250. At the 0.2 g dosage, 100% of Cu was removed while the complete adsorption of Pb commenced from 0.6 g dosage. Zn and Mg were equally removed with Mg having the least removal efficiency of 60% in all concentrations. The maximum efficiency in AC-250 treatment of the stale foundry effluent was obtained at an adsorbent dosage of 1 g. The efficiency of treatment increases with the adsorbent dosage.

Table 2: Results obtained from the absorbent dosage study

Adsorbent dosage used in treatment (in grams)	***Concentration of metals present after treatment (in mg/L)***			
	Zn	***Cu***	***Mg***	***Pb***
0.2	0.101	0.00	1.106	0.008
0.4	0.072	0.00	1.101	0.007
0.6	0.060	0.00	1.069	0.00
0.8	0.023	0.00	0.843	0.00
1.0	0.019	0.00	0.806	0.00

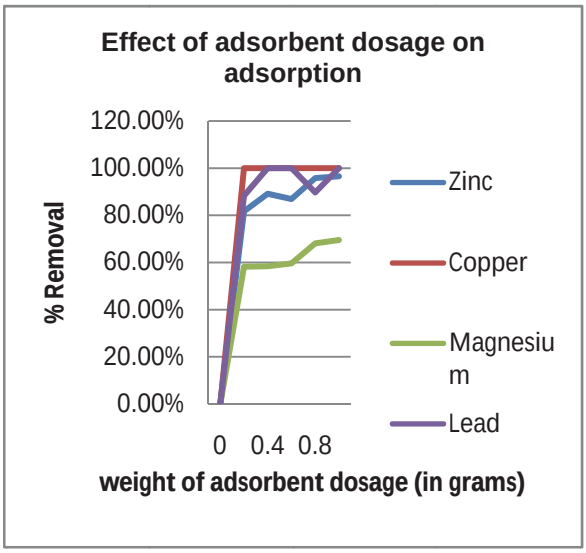

Figure 6: The removal percentage based on the adsorbent dosage

(c) Effect of contact time on the treatment process

The pattern of treatment based on the effect of contact time of the adsorbent with wastewater is as shown on Table 3 and Figure 7.

It is observed that in virtually all the treatment cases the removal efficiencies increase with the contact time. Pb however had 100% removal right from the 60 mins contact time. The maximum efficiency in the treatment was obtained at a contact time of 120 minutes for all the studied metals.

Table 3: Results of the effect of contact time on the treatment

Contact time (in minutes)	*Concentration of metals after treatment (in mg/L)*			
	Zn	*Cu*	*Mg*	*Pb*
20	0.079	0.222	1.063	0.026
40	0.043	0.186	1.101	0.116
60	0.072	0.318	0.954	0.00
80	0.024	0.084	0.364	0.00
100	0.024	0.00	0.287	0.00
120	0.00	0.00	0.044	0.010

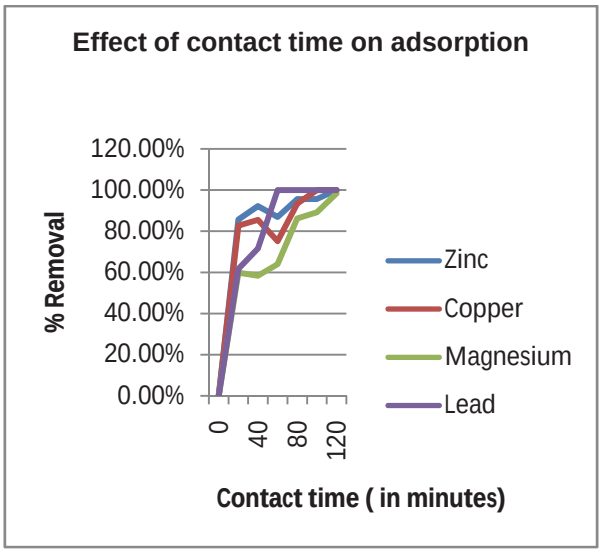

Figure 7: Percent removal of metals due to contact time of AC-250

(d) Effect of rotating/stirring speed on the treatment process:

Results of the rotating speed and the metal remediation are presented on Table 4 and Figure 8. Pb was totally removed right from 200 rpm while other metals show percent increase in removal with the agitation increase. Mg was however least removed with increasing stirring speed.

Table 4: Results on effect of the rotating speed on the treatment

Rotating/Stirring speed (in RPM)	*Concentration of metals after treatment (in mg/L)*			
	Zn	*Cu*	*Mg*	*Pb*
150	0.045	0.243	1.560	0.031
200	0.029	0.222	1.682	0.00
250	0.063	0.364	1.854	0.00
300	0.040	0.255	1.669	0.00
350	0.047	0.159	1.182	0.00

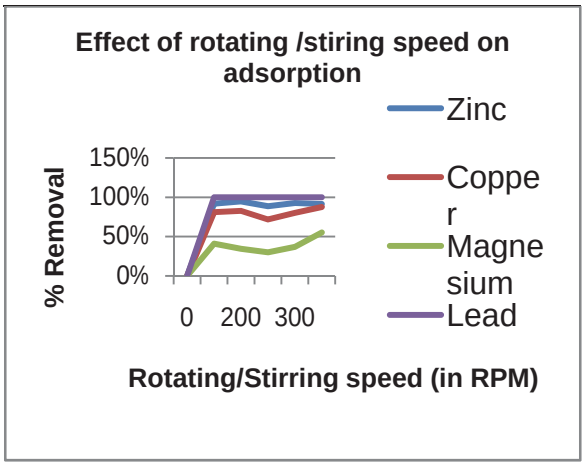

Figure 8: Effect of rotating speed on the adsorption process

(e) Effect of pH on the treatment process

The effects of pH on the adsoption process using AC-250 are presented on Table 6 and in Figure 9. The metal removal efficiency is observed to increase with pH increase except in the case of Pb where the pattern appears undefined.

Table 6: Effect of pH on the treatment

pH value maintained	*Concentration of metals after treatment (in mg/L)*			
	Zn	*Cu*	*Mg*	*Pb*
2	0.344	0.318	3.708	0.00
4	0.054	0.177	3.281	0.057
6	0.084	0.404	2.148	0.00

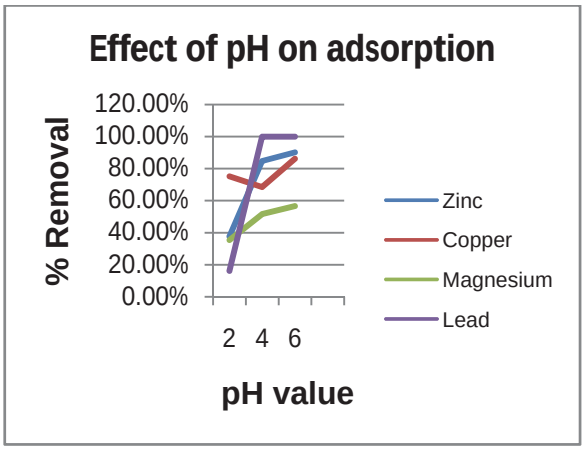

Figure 9: Representation of the effect of pH on the treatment

(e) Optimum foundry wastewater treatment conditions for the AC-250

The activated charcoal-250 is found as an efficient adsorbent in treating the stale foundry wastewater. The optimum conditions in required for the most efficient treatment of 50mL of the studied Lamina foundry effluent containing Zn, Cu, Mg and Pb present in 0.552, 1.283, 2.647 and 0.068 mg/L respectively are:

1. An adsorbent dosage of 1 gram
2. A contact time of 120 minutes
3. A rotating/agitation speed of 350 rpm and
4. A pH value of 6.

(f) Cost Estimate for the treatment process:

For 50ml foundry effluent, the dosage quantity required is 1gm of activated charcoal-250.
Therefore, 1ml = 1/50 g,

And 1000ml = 1000/ 50g,
Therefore for treating 1 Litre of foundry wastewater containing heavy metals we require 20g of activated carbon-250

Cost of 500 g = Rs 572/-
Cost of 1 g of AC-250 = Rs (572/500)
= Rs 1.144
Therefore, the average cost of treating 1 litre of foundry wastewater = Rs 1.144x20

= Rs 22.88

or 0.38 USD

4. Conclusion and Recommendation

The Activated Charcoal (AC-250) was found as efficient in adsorption of the heavy metals consisting of Zn, Cu, Mg and Pb from foundry wastewater. In some of the cases a 100% removal is possible, especially with Pb. The analysis of the major experiments on effects of adsorbent dosage, contact time rotating speed and pH on the adsorption process, gave the optimum conditions for removal under which the most efficient treatment of the wastewater containing studied heavy metals was possible. For the optimum treatment conditions, an adsorbent dosage of 1 g, a contact time of 120 minutes, a rotating/agitation speed of 350 rpm and a pH value of 6 are established. An average cost of treating 1 litre of stale foundry wastewater is Rs 23 or 0.4 USD. This study therefore recommends AC-250 as an efficient adsorbent at the given optimum conditions for stale foundry wastewater. The reuse of AC-250 via the process of thermal reactivation at 800^0C is encouraged as a means of waste management.

5. References

[1] Ojoawo, S.O and Udayakumar, G "Remediation of Zn, Cu, Mg and Pb from fresh foundry wastewater with Activated Carbon as adsorbent", Proceedings of the 4th International Conference, Ladoke Akintola University of Technology, Ogbomoso, Nigeria, 2015.
[2] Bansal, R.P. and Goyal, M. Activated Carbon Adsorption, CRC Press, Taylor & Francis Group, 6000 Broken Sound Parkway NW, Suite 300 Boca Raton, FL, USA 33487–2742, 2005.
[3] Encyclopedia Britannica.
[4] Cecen, F. snd Aktas, O. "Activated carbon for water and waste water treatment", 2013.

Performance Analysis of Scheduling Algorithm for Cloud Computing

Akshay M Murshilli[#], Sarojadevi Hande*
[#]*PG student, Department of Computer Science and Engineering,*
NMAMIT, Nitte, Karkala, Udupi, Karnataka - 574-110, Affiliated to VTU – Belgaum.
[1]ak.murshilli@gmail.com

**Professor, Department of Computer Science and Engineering,*
NMAMIT, Nitte, Karkala, Udupi, Karnataka - 574-110, Affiliated to VTU – Belgaum.
[2]sarojadevi@nitte.edu.in

Abstract— Cloud Computing is considered has the delivery of services, like mainly computing services over the Internet. Cloud computing at present aims to provide the data centers and it enables application service providers to lease there data center capabilities mainly for deploying applications over the cloud, depending on the user Quality of Service requirements. Cloud applications will be having different configurations, compositions and deployment requirements. Measuring the performance of the resource allocation policies and of application scheduling algorithms at finer details is one of the challenging problems to tackle in Cloud computing environments. In this paper the CloudSim architecture, CloudSim life cycle is explained and also the scheduling methods like Time-Space shared scheduling method, FIFO based scheduling and Priority based scheduling methods are proposed and evaluated. This analysis helps in virtual to real deployment and would be easier and accurate.

***Keywords*-CloudSim, Cloud Computing, Cloud Applications, Application Scheduling.**

I. INTRODUCTION

Cloud Computing is one of the technologies which provides secured and efficient services over the internet. Cloud computing at present generation aims to provide the data centers and it enables the application service providers to lease there data center capabilities mainly for deploying applications over the cloud, depending on the user Quality of Service requirements. Cloud services which are now available allow businesses and individuals to use software and hardware which are managed by third parties somewhere located at remote locations. Cloud Computing is mainly used for providing a service to the consumer, it is “pay as per use” service. Cloud Computing provides services such as Platform as a service (PaaS), Software as a Service (SaaS) and Infrastructure as a service (IaaS). Now a day’s the internet is fast growing, the individuals and big organizations are finding new ways to reduce the cost of implementation, storage or communication.

Cloud Computing has mainly has two parts, the First part is of mainly the Client Side and the second part is mainly the Server Side. The Client Side requests to the Servers and the Server responds back to the Clients. The request from the client firstly goes to the Server Side Master Processor. The Master Processor will be having many Slave Processors; the Master Processor will be sending that request to any one of the Slave Processor which are free at that time. All Processors will be busy in their assigned job and none of the Processor gets Idle.

In Cloud Computing Job Scheduling is a very difficult due to its parallel and distributed environment. The order in which work is performed in the computer system is called Scheduling. Job may be distributed among more than one virtual machine, so it is difficult to determine the job completion time.

To host an application in cloud environment requires complex deployment and composition and to evaluate the implemented model in repeated manner is very tedious and costly process. So simulation tools like CloudSim are used to model Cloud Computing systems and application environment. The CloudSim is an extensible simulation toolkit that enables simulation and modeling of Cloud Computing environments. The CloudSim toolkit supports for modeling and creation of virtual machines (may be one or more VM’s) on a simulated node of a Data Center, jobs and their mapping to suitable VMs. It allows simulation of multiple Data Centers which enables in a study on federation and associated policies for migration of Virtual Machines for reliability and also for automatic scaling up of applications.

CloudSim provides lots of benefits to IT companies or an individual who wants to deploy his services through cloud. CloudSim has the following important properties [09]:

- CloudSim helps to simulate and model the data center, Cloud Computing environments.
- CloudSim provides a self-contained platform for modelling clouds, provisioning, service brokers and allocation policies.

- CloudSim provides support for simulation of connections like network connections mainly among the simulated system resources.
- CloudSim provides facility for simulation of cloud environments, mainly like federated cloud environments that inter-network resources.

These features show that CloudSim aids in developing the cloud environments and it uses sequential algorithms [10] like FCFS to allocate the resources. This sequential way may not match with the real world requirements because there are different types of requirement in the real world that must be categorized and allocation should be done based on different categories. So there is need to refine the algorithm and architecture of CloudSim so that every experiment using this simulator can be compared directly to the physical set up of cloud environment. By doing this the cost and time of cloud implementation can be reduced.

CloudSim Simulation Environment: CloudSim frame work does the following things, firstly entity will be created which is named as CIS (Cloud Information Service), and this is the kind of registry that contains the resources that are available on the cloud. So CIS takes care of registry of the data center. Now data center is required to be registered and this registration process will be done with the CIS. Data center will be having some characteristics. Characteristics are basically for the hosts, each host will have some hardware configurations like number of processing elements, RAM, Bandwidth etc.

The cloud environment basically works on virtualization which differs from other technologies like parallel computing, grid computing etc. So virtualization says that the host will be virtualized into the number of machines, so each virtual machine will have the parameter.

It requires registering the datacenter with the CIS, as per the CloudSim frame work. Once above all process is done, it is required to have the broker which will submit tasks to the data centers. Broker is basically an entity which at the initial stage talks to CIS and retrieves the resource information which is registered with the CIS about data centers, so the information so passed is called data center characteristics, now the broker will be having all the characteristics of the data centers. Refer to the **Figure 01** below:

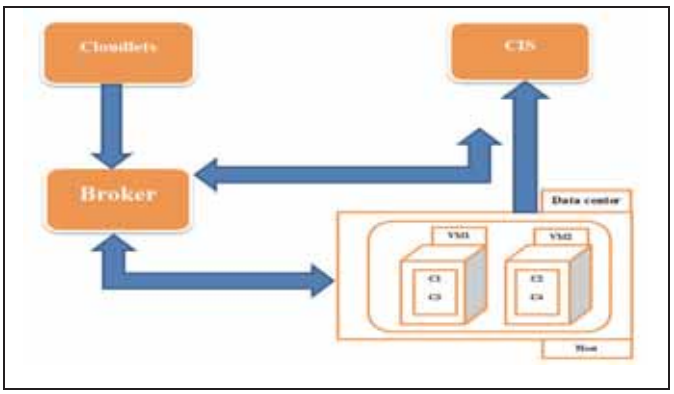

Figure 01: CloudSim Simulation Environment

Broker will have some tasks which are named as **Cloudlet(s)**, so set of cloudlets will be submitted to the broker. The broker directly interacts with the data center and assigns the cloudlet to some of the virtual machines which are running on the host. This is the basic framework or basic model which the CloudSim simulation tool which provides us. CloudSim simulation tool takes care of lot of behavior's which are connected to all of the components, so the components are basically called as Entities.

The above model works on various kinds of policies. We can submit more than one task to the virtual machines but overall processing is to be done is on the physical machine because the virtual machines share the resource of the physical machine. All the resources will be provided to the virtual machines on the basis of the policies i.e. virtual machine scheduler policies. So there are three different kinds of policies.

1. VM allocation policy.
2. VM scheduler policy.
3. Cloudlet scheduler policy.

So all the policies are either time shared or space shared.

II. RELATED WORK

Harjit Singh has discussed about the evolution process of cloud computing, characteristics of Cloud, current technologies adopted in cloud computing and they also presented a comparative study of cloud computing platforms (Amazon, Google and Microsoft), and its challenges. Cloud computing is the delivery of computing services over the Internet [01].

Qi Zhang has presented a survey of cloud computing, highlighting its key concepts, architectural principles and state-of-the-art implementation as well as research challenges. The aim of the paper is to provide a better understanding of the design challenges of cloud computing and identify important research directions in this increasingly important area [02].

Monica Gahlawat, Priyanka Sharma have described about the basic information about the Cloud Computing and its various services and models like SaaS, IaaS and PaaS. They also described about the deploying models of Cloud Computing and Virtualization services [03].

Rodrigo N. Calheiros, Rajiv Ranja, Anton Beloglazov, Rajkumar Buyya, A. F. De Rose have described about the various web based application related to Cloud Computing [04].

Anthony Sulistio, Rajkumar Buyya have described about the Scheduling. They said Scheduling is a process of finding the efficient mapping of tasks to the suitable resources so that execution can be completed such as minimization of execution time as specified by customers. They described various types of Scheduling like Static, Dynamic, Centralized, Hierarchical, Distributed, Cooperative, Non- Cooperative Scheduling. They also described Scheduling problem in Cloud and the types of users like CCU (Cloud Computing

Customers) and CCSP (Cloud Computing Service Providers) [05].

Catalin L. Dumitrescu, Ian Foster have described about the Simulation techniques and the CloudSim. They described the various features of CloudSim like it supports for modeling and simulation for large scale of cloud computing infrastructure including data centers on a single physical computing node [06].

Henri Casanova, Arnaud Legrand have described about the optimization criterion that is used when making scheduling decision and represents the goals of the scheduling process. The criterion is expressed by the value of objective function which allows us to measure the quality of computed solution and compare it with different solution [07].

Saul Berman, Lynn Kesterson-Townes, Anthony Marshall and Rohini Srivathsa have described about the Quality of Service that is the ability to provide different jobs and users, or to guarantee a certain level of performance to a job. If the QoS mechanism is supported it allows the user to specify desired performance for their jobs. In system with limited resources the QoS support results in additional cost which is related to the complexity of QoS requests and the efficiency of the scheduler when dealing with them [08].

III. SIMULATION WORK

Here it is explained about how actually the simulation works and for each module the code is included. Initially it is required to set the number of users; this will directly correlates with the broker count.

1. Requires the initialization of common variables.
   CloudSim.*init* (num_user, calendar, trace_flag);
2. Data center must be created, this in turn will lead to the creation of host, characteristics (Parameters: Processing Elements, RAM, BW etc.)
   Datacenter datacenter0 = *createDatacenter* ("Datacenter_0");
3. Datacenter broker instance is required to be created.
   DatacenterBroker broker = *createBroker* ();
   int brokerId = broker.getId ();
4. Virtual machines (Parameters: Processing Elements, RAM, BW etc.) instances is required to be created.
   Vm vm1 = **new** Vm (vmid, brokerId, mips, pesNumber, ram, bw, size, vmm, **new** CloudletSchedulerSpaceShared());
5. Virtual machines which are created are submitted to the broker.
   broker.submitVmList (*vmlist*);
6. Requires specifying the cloudlet(s) which are created with the certain parameters.
   Cloudlet cloudlet = **new** Cloudlet (id, length, pesNumber, fileSize, outputSize, utilizationModel, utilizationModel, utilizationModel);
7. Cloudlets which are created are submitted to the broker. So now broker has both Cloudlets and Virtual machines. Cloudlets will be mapped to the virtual machines through broker.
   broker.submitCloudletList (*cloudletList*);
   broker.bindCloudletToVm (cloudlet.getCloudletId(),vm.getId());
8. Start Simulation function is called.
9. Stop Simulation function is called.
10. Prints the status of the simulation.

Data Center consists of Hosts i.e. different Hosts and it (Hosts) manages the Virtual Machine Scheduler and VM's. Cloudlet Scheduler mainly determines about how the available CPU resources of VM are divided among Cloudlets. There are two types of policies:

1**] Space-Shared** (Cloudlet Scheduler Space Shared): This is used for assigning specific cores like CPU cores to specific Virtual Machines.

2] **Time-Shared** (Cloudlet Scheduler Time Shared): This is used mainly to dynamically distribute the capacity of a core among Virtual Machines.

Whenever the cloudlets are deployed on VMs, both the Time shared and Space Shared is incorporated.

IV. PROPOSED FRAMEWORK

In the CloudSim simulation toolkit, the VMs are created and are allocated based on the requirement of the hosts. An application is developed which simulates the cloud and performs the Allocation i.e. Task Allocation to the Virtual Machines on the basis of First-Come-First-Served (FCFS) Scheduling Policy in the Cloud.

The proposed architecture is given as **Figure 02**:

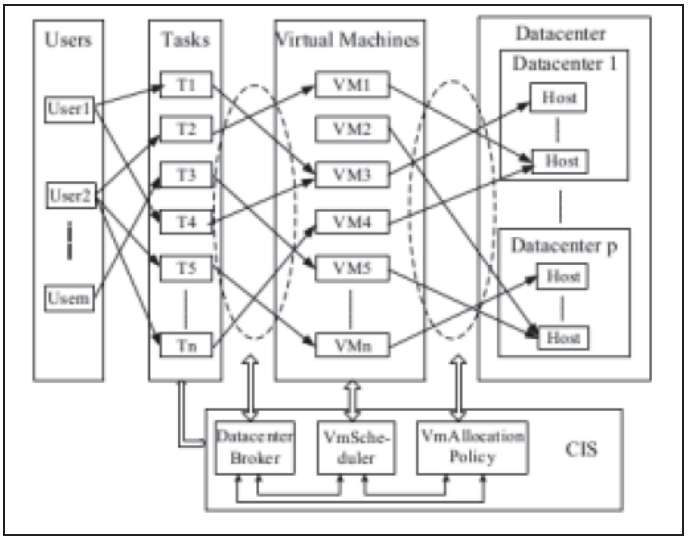

Figure 02: FCFS task allocation in CloudSim

Our First Come First Serve scheduling will be having a Datacenter Broker that implements the First Come First Serve Task Scheduling Policy. The Entities used in the application are:

- First Come First Serve i.e. FCFS
- Broker i.e. FCFS Broker
- Datacenter i.e. Datacenter Creator
- Virtual Machine Creator i.e. VM's Creator
- Creator i.e. Tasks or Cloudlet Creator

FCFS: This FCFS entity is used for creating the Datacenter and for creating the VM's and for creating the Cloudlets or Tasks by calling the other respective entities. Once all of these are created Virtual Machines and Tasks are submitted to the broker First Come First Serve Broker.

FCFS Broker: This Entity is Datacenter Broker and it is used for scheduling the tasks to the VM's on the basis of First Come First Serve policy. The tasks are obtained from the First Come First Serve Entity.

Datacenter Creator: This is used for creating the Datacenter(s).

VMs Creator: This entity is used for creating the specified number of Virtual Machines given by the user.

Cloudlet Creator: This is used for creating the specified number of tasks.

Thus, we can perform task allocation to the Virtual Machines on the basis of First-Come-First Served (FCFS) Scheduling Policy in the Cloud.

Cloud computing is a "pay as you go" service. It is not that much easy to deploy the simulated work directly to the real world because the cloud services are layered services and it takes additional scenarios

also into consideration. For example when we are providing a service as cloud, we will be having several tasks that will be having higher priorities and are needed to be finished first and there will also be some other tasks which are defined earlier and are needed to be performed according to the scheduled time. These are the scenarios that differs the simulated work with the real world.

In the CloudSim simulation toolkit, the Virtual Machines are created and are allocated in First Come First Serve manner which is based on the requirement of the hosts. The proposed architecture for implementing priority based implementation is given in **Figure 03:**

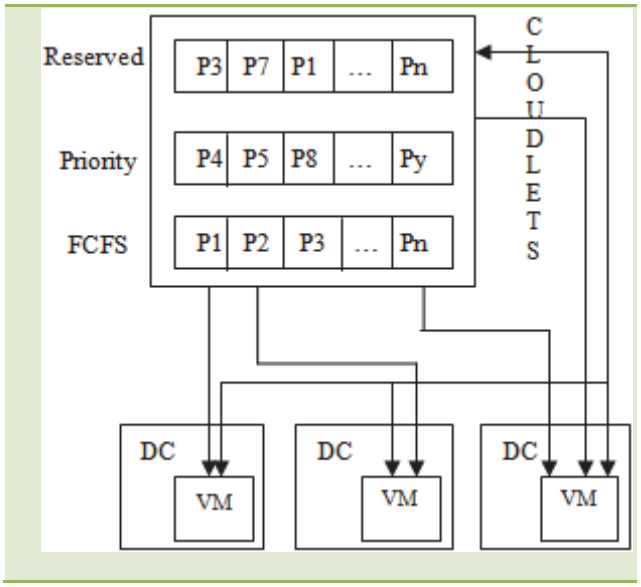

Figure 03: Priority based task allocation in CloudSim

To map the simulation in real world more effectively so firstly the cloudlets are divided into different types of jobs. Based on that the tasks assigned to the Virtual Machines to the hosts and for this assignment there a need to use priority scheduling rather than First Come First Scheduling in data center's scheduling algorithm [8]. There are also some other entities that are needed to be taken care while making changes in scheduling algorithm. The algorithm is needed to be changed in three parts of the data center code that is given as a pseudo code here:

Pseudo Code for resource scheduling

```
1. If (cloudlet_list == empty)
2. New cloudlet_list = cloudlet(id, name, length, file size,
priority) ;
3. If (priority == 0)
4. {
5.        Q_fcfs[] = Cloudleti ;
6. }
7. Elseif (priority == 1)
8. {
9.        Q_priority[] = Cloudleti ;
10. }
11. Else {Q_reserve = Cloudleti;}
12. DataCenterScheduler = get_cloudlet_List();
13. If ((cloudlet_property <= VM_property) &&(priority==
high))
14. {
15.   bindcloudletToVm( cloudlet_id, vm_id);
16. }
17. Else {wait || create new vm || suspend_current_proc;} //if
possible
18. If (cloudlet_work== over && vm == free)
19. {
20.   Destroy_vm(id);
21. }
22. Repeat step 1 to 20 till all requests completed.
23. endif.
```

In this way priority based scheduling helps in deployment of cloud environment as hypotheses during experiment or simulation and thus helps to save large amount of money and time for the organizations and researchers.

V. RESULTS AND ANALYSIS

The type of scheduling policy used here is Time shared /Space Shared allocation policy. The simulation gives the timing performance as shown in the **Table 01,** referring to this table and considering the cloudlet performance of 3200sec, compared to the one without multiple cloudlets sharing the work, we get a speed up of 2. The speed up is given by the ratio of timing measurement without using multiple cloudlets sharing the work, over the timing with sharing.

Therefore Speedup = 800*8/3200
= 6400/3200
= 2

Table 1: Timing performance of different number of cloudlets.

Total No. of Cloudlets	Timing Performance (Sec)
1	800
2	1600
8	3200

Speed up obtained is low compared to the ideal speed up. Therefore alternate mechanisms for improving performance such as FCFS method and priority based method are experimented in CloudSim.

The FCFS based scheduling and priority based method is implemented and comparison of which is made with the performance of Time-Space shared scheduling of 8 cloudlets is given in **Table 02.** These simulation runs are carried out for **8 cloudlets** and **2 VMs**.

Table 2: Time taken to execute the cloudlets based on the scheduling policy.

Scheduling Policy	Timing(Sec)
Time-Space Shared Scheduling	3200
FCFS	20.1
Priority	10.1

The FCFS Scheduling takes 20.1sec for executing all 8 cloudlets. We have improved the execution time by using the scheduling policy like priority based scheduling policy. **Screen Shots** for the Simulation runs corresponding to the results shown in **Table 02** are given below in **Figure 03**, **Figure 04 and Figure 05.**

The simulation output displays the following information. The CloudSim toolkit is initialized and then datacenters are started, broker will be starting, Entities are started. Broker creates the VMs in the Datacenter and is created in the particular Host. Broker sends the cloudlets to the VMs. Cloudlets get executed and time at which the cloudlets got executed is sent back to broker. After when all cloudlets are executed all VMs are destroyed. Broker shuts down. Cloud Information Service (CIS) notifies to all entities to shut down. Simulation gets completed and status about the simulation is displayed.

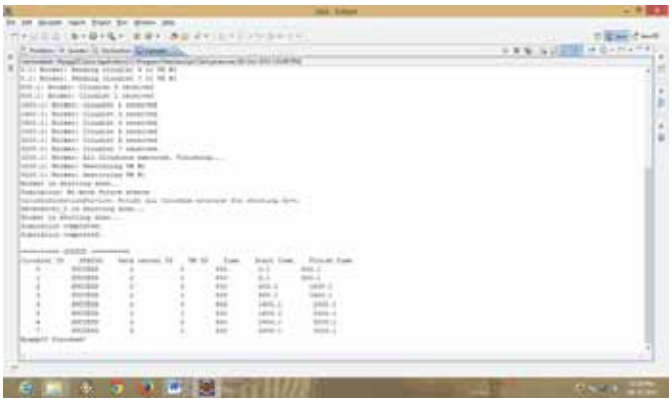

Figure 03: Time-Space Shared Scheduling

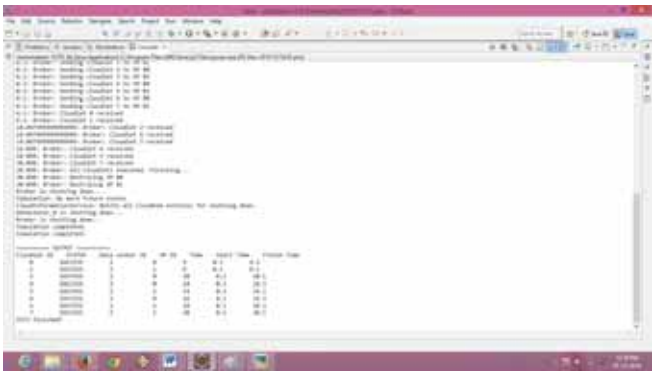

Figure 04: FCFS Based Scheduling

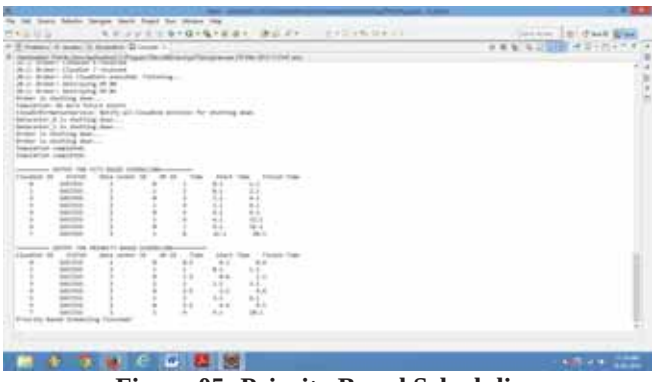

Figure 05: Priority Based Scheduling

VI. CONCLUSION

Recently many efforts have been done in cloud technology to develop various techniques and have been presented to make it more efficient. CloudSim has been developed to help the organization and researcher to evaluate their experimental model before deployment in the real world. If the deployment is different from what we hypothyse then it causes heavy implementation and cost time. So in this paper simulation strategy is defined in real world manner so that the experiment what is being executed using CloudSim can be deployed directly in the cloud environment. Approaches to improve the performance of applications in Cloud Computing are discussed in this paper. An evaluation of the Scheduling mechanisms such as FCFS based Scheduling Priority based Scheduling and Time-Space Scheduling are done in CloudSim environment. The results obtained indicate the scope for further improvement of the performance.

REFERENCES

[1] *Harjit Singh*, "Current Trends in Cloud Computing a Survey of Cloud Computing Systems", 2009.

[2] *Qi Zhang*, "Cloud computing: state-of-the-art and Research Challenges", 2010.

[3] Monica Gahlawat, Priyanka Sharma, "Analysis and Performance Assessment of CPU Scheduling Algorithms in Cloud using CloudSim", International Journal of Applied Information Systems (IJAIS) – ISSN: 2249-0868, 2013.

[4] Rodrigo N. Calheiros, Rajiv Ranja, Anton Beloglazov, Rajkumar Buyya, A. F. De Rose, "CloudSim: a toolkit for modelling and simulation of cloud computing environments and evaluation of resource provisioning algorithms", 2010.

[5] Anthony Sulistio, Rajkumar Buyya, "A Grid Simulation Infrastructure Supporting Advance Reservation".

[6] Catalin L. Dumitrescu, Ian Foster, "GangSim: A Simulator for Grid Scheduling Studies", 2005.

[7] Henri Casanova, Arnaud Legrand, Martin Quinson, "SimGrid: a Generic Framework for Large-Scale Distributed Experiments", 2006.

[8] Saul Berman, Lynn Kesterson-Townes, Anthony Marshall and Rohini Srivathsa, "The power of cloud: Driving business model innovation", IBM Global Business Services Executive Report.

[9] Akshay M Murshilli, Dr. Sarojadevi H, "Approaches to Improve Cloud Computing Performance Using CloudSim Toolkit" 2015.

[10] Monica Gahlawat, Priyanka Sharma, "Analysis and Performance Assessment of CPU Scheduling Algorithms in Cloud using CloudSim", International Journal of Applied Information Systems (IJAIS) – ISSN: 2249-0868, 2013.

Noise Removal and Estimation of SNR for Musical and Speech Noisy Signals

Srinidhi S Shetty [#], Sarojadevi Hande*

[#]*PG student, Department of Computer Science and Engineering,*
NMAMIT, Nitte, Karkala, Udupi, Karnataka - 574-110, Affiliated to VTU – Belgaum.
[1]srinidhishetty15@gmail.com

*Professor, *Department of Computer Science and Engineering,*
NMAMIT, Nitte, Karkala, Udupi, Karnataka - 574-110, Affiliated to VTU – Belgaum.
[2]sarojadevi@nitte.edu.in

***Abstract*— Non diagonal method for removing noise from audio signals is discussed in this paper. Noise is reduced by adaptive time-frequency block thresholding procedure using Short Time Fourier Transform (STFT) to obtain better SNR of the audio signal. The STFT coefficients of noisy audio signals are grouped in blocks and then these coefficients are attenuated. Window functions used are Hann window and Hamming window during STFT. Results of block thresholding when Hann window is used and when Hamming window is used are compared.**

***Keywords*— Non diagonal, SNR, thresholding**

I. INTRODUCTION

Audio is contaminated by various types of noise during its acquisition [5]. Noise removal aims at reducing the noise from audio without changing the original signal. There are numerous applications such as music and speech restoration. Each spectrogram coefficient is processed independently in diagonal time frequency audio denoising algorithms [1], [2]. This is done with power subtraction, empirical Wiener or thresholding operators. The performance of these algorithms is limited. Due to the lack of time frequency regularity these algorithms create isolated time frequency structures [1], [2]. Musical noise is produced because of this isolated time frequency structures. Non diagonal time frequency estimators strongly reduce the musical noise. This non diagonal time frequency estimators regularize the estimation by recursively grouping time frequency coefficients. Block thresholding which is the non diagonal audio denoising method does not produce musical noise because isolated time frequency structures are not created by this algorithm [1], [2]. A short time Fourier transform of the noisy audio signal is computed and the resulting coefficients is processed to attenuate the noise. The window functions used are Hann window and Hamming window during short time Fourier transform. The short time Fourier transform is invertible that is inverse short time Fourier transform is used to recover the original signal from the transform [3]. Both speech and music are generally not stationary [4]. To recover the original signal power of the noisy signal has to be reduced which gives better Signal to Noise Ratio (SNR).

II. TIME – FREQUENCY AUDIO NOISE REDUCTION

Short time Fourier transform of the noisy audio signal is computed by time frequency audio noise reduction procedure
and the resulting coefficients is processed to reduce the noise [2]. The audio signal is corrupted by noise and the noisy audio signal is [2]:

$$n[x] = s[x] + \varepsilon[x], \qquad x = 0,1, \ldots\ldots, N-1 \qquad (1)$$

where $n[x]$ - Noisy Audio Signal, $s[x]$ – Audio Signal, $\varepsilon[x]$ - Noisy Signal.

The resulting coefficients after time frequency transform of the audio signal is [2]

$$N[t,f] = \langle n, j_{t,f} \rangle = \sum_{x=0}^{N-1} n[x] j^*_{t,f}[x] \qquad (2)$$

Where t and f are time and frequency localization indices and * denotes the conjugate.

Hann window and Hamming window are the window functions used during STFT. The equation used to compute coefficients of a Hann window is [6]

$$w(n) = 0.5\left(1 - cos\left(2\pi \frac{n}{N}\right)\right), 0 \le n \le N \qquad (3)$$

The length of the window is $L = N + 1$

The equation used to compute coefficients of a Hamming window is [7]

$$w(n) = 0.54 - 0.46cos\left(2\pi \frac{n}{N}\right), 0 \le n \le N \qquad (4)$$

The length of the window is $L = N + 1$

III. TECHNIQUES FOR ESTIMATING NOISE

Diagonal Estimation Technique and Non Diagonal Estimation Technique are two techniques for estimating noise [1], [2].

A. Diagonal Estimation Technique

Each attenuation factor $a[t,f]$ is computed only from the corresponding noisy coefficient $N[t,f]$ by simple time frequency denoising algorithms. These are called diagonal estimators. These algorithms has limited performance and produce musical noise. For minimizing the quadratic estimation risk the expression is [1]

$$r = E\{\|s - \hat{s}\|^2\} \leq 1 /A \sum_{t,f} E\left\{\left|S[t,f] - \hat{S}[t,f]\right|^2\right\} \quad (5)$$

Optimal attenuation factor is [1]

$$a[t,f] = 1 - \frac{1}{\xi[t,f] + 1} \quad (6)$$

where

$$\xi[t,f] = S^2[t,f]/\sigma^2[t,f] \quad (7)$$

Posteriori SNR defined by [1]

$$\gamma[t,f] = |N[t,f]|^2/\sigma^2[t,f] \quad (8)$$

This posteriori SNR is used for computing diagonal estimators of the SNR $\xi[t,f]$.

And an unbiased estimator [1]

$$\hat{\xi}[t,f] = \gamma[t,f] - 1 \quad (9)$$

B. Non Diagonal Estimation Technique

The task is to estimate the a priori SNR $\xi[t,f]$ with a time frequency regularization of the a posteriori SNR $\gamma[t,f]$ to reduce musical noise as well as the estimation risk [1], [2]. The resulting attenuation factors $a[t,f]$ depend upon the data values $N[t',f']$ for (t',f') in a whole neighborhood of (t,f) and the resulting estimator can be written as [1]

$$\hat{s}[x] = 1/A \sum_{t,f} a[t,f]\, N[t,f] j_{t,f}[x] \quad (10)$$

Musical noise and estimation risk is reduced by regularization of the SNR estimation and estimation risk is [1]

$$r = E\{\|\hat{s} - s\|^2\} \quad (11)$$

IV. BLOCK THRESHOLDING

Segmentation of the time-frequency plane (t, f) in to I blocks B_i is done and shape of these blocks is chosen arbitrarily [1]. The signal estimator $\hat{s}$ is calculated from the noisy data n and for every block B_i constant attenuation factor a_i is used.

$$\hat{s}[x] = \sum_{i=1}^{I} \sum_{(t,f)\in B_i} a_i N[t,f] j_{t,f}[x] \quad (12)$$

$$N[t,f] = S[t,f] + \varepsilon[t,f] \quad (13)$$

Attenuation factor chosen to minimize this is

$$a_i = 1 - \frac{1}{\xi_i + 1} \quad (14)$$

Average a priori SNR in B_i is

$$\xi_i = \ddot{S}_i^2/\ddot{\sigma}_i^2 \quad (15)$$

Where $\ddot{\sigma}_i^2$ is variance

Average a priori SNR in B_i is calculated from

$$\ddot{S}_i^2 = 1/B_i^{\#} \sum_{(t,f)\in B_i} |S[t,f]|^2 \quad (16)$$

$$\ddot{\sigma}_i^2 = 1/B_i^{\#} \sum_{(t,f)\in B_i} \sigma^2[t,f] \quad (17)$$

which are the average signal energy and noise energy in B_i and $B_i^{\#}$ is the number of coefficients $(t,f) \in B_i$.

The block thresholding estimators that estimate the SNR over each B_i by averaging the noisy signal energy

$$\hat{\xi}_i = \frac{\ddot{N}_i^2}{\ddot{\sigma}_i^2} - 1 \quad (18)$$

where $\hat{\xi}_i$ is an unbiased estimator

$$\ddot{N}_i^2 = 1/B_i^{\#} \sum_{(t,f)\in B_i} |N[t,f]|^2 \quad (19)$$

And attenuation factor is

$$a_i = \left(1 - \frac{\lambda}{\hat{\xi}_i + 1}\right) \quad (20)$$

All coefficient in every block is used for calculating attenuation factor.

V. ADAPTIVE BLOCK THRESHOLDING

All parameters are adapted to the time-frequency regularity of the audio signal by an adaptive audio block thresholding algorithm [1], [2]. Stein Unbiased Risk Estimator is calculated from the data. The adaptation is performed by minimizing this Stein Unbiased Risk Estimator. The time frequency plane disjoint rectangular blocks of length L_i in time and width W_i in frequency are block thresholding segments. Block size is the choice of block size and shapes among a collection of possibilities. An estimate of

the risk is minimized and sizes are chosen by adaptive block thresholding.
The Risk estimator [1]

$$R_i = \ddot{\sigma}_i^{\,2}\left(B_i^{\#} + \left(\lambda^2 B_i^{\#} - 2\lambda\left(B_i^{\#} - 2\right)\right) / \left(\ddot{N}_i^2/\ddot{\sigma}_i^2\right) + B_i^{\#}\left(\ddot{N}_i^2/\ddot{\sigma}_i^2 - 2\right)\right) \quad (21)$$

Macroblocks size is set to be equal to 8×16 which is maximum block size.
The SNR is defined as [1]

$$SNR = 10\log_{10}\sum_{x=0}^{N-1} s^2[x] / \sum_{x=0}^{N-1}(s[x] - \hat{s}[x])^2 \quad (22)$$

A. Selection of threshold level λ

Different block size $B_i^{\#}$ and their respective thresholding level λ [1] is shown in Table I

TABLE 1
BLOCK SIZE $B_i^{\#}$ AND THRESHOLDING LEVEL λ [1]

$B_i^{\#}$	4	8	16	32	64	128
λ	4.7	3.5	2.5	2.0	1.8	1.5

Let the rectangular block size be $B_i^{\#} = L_i \times W_i$ where $L_i \geq 2$ and $W_i \geq 2$. L_i is block length in time W_i is block width in frequency.

B. Selection of block

The size of the block is $B_i^{\#} = L_i \times W_i$ where L_i is block length in time and W_i is block width in frequency. The coefficients are grouped in blocks by adaptive block thresholding [1], [2]. The block sizes L×W are adjusted to minimize the Stein risk estimate and coefficients in those blocks are attenuated by adaptive block thresholding. Each of the macroblock is segmented. Fifteen possible block sizes are used with a combination of block length L=8, 4, 2 and block width W=16, 8, 4, 2, 1.

VI. IMPLEMENTATION DETAILS AND RESULTS

Audio noise removal scheme is shown in Fig. 1. Noisy audio signal is obtained by adding Gaussian white noise to original audio signal. Using STFT the noisy audio signal is transformed to time frequency domain. Hann/Hamming window is used during STFT. Block Thresholding is applied which groups the STFT coefficients of noisy audio signal in blocks and then the coefficients are attenuated. Inverse STFT (ISTFT) is applied to get denoised audio signal in time domain. This project is implemented in MATLAB 7.14.0.739

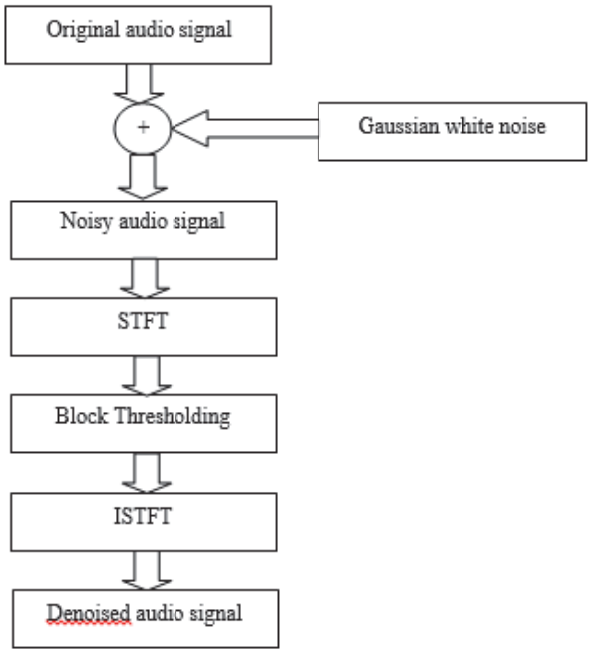

Fig. 1 Audio Noise Removal

Table 2 and Table 3 shows the performance of the Block Thresholding (BT) algorithm which is decided with the help of Signal to Noise Ratio (SNR). Sampling rate of audio signals (Music and Speech) is 11 kHz and audio signals are contaminated by Gaussian white noise. Better SNR of the noisy musical and speech signals is obtained after applying block thresholding algorithm. The SNR ratio of block thresholding when Hamming window is used is greater than SNR ratio of block thresholding when Hann window is used for low input SNR ratio because Hann window has sharp cut-off compared to Hamming window. Also SNR ratio of block thresholding when time window of 100ms is used is greater than SNR ratio of block thresholding when time window of 50ms is used for low input SNR ratio.

Table 2
PERFORMANCE of BLOCK THRESHOLDING ALGORITHM (50ms TIME WINDOW)

Signal	Input SNR (in dB)	BT (Hann window)	BT (Hamming window)
Music	-5	2.99	3.31
	0	9.07	9.44
	2	12.08	12.12
	4	14.47	13.90
	5	15.32	14.45
	10	12.97	11.44
Speech	-5	0.89	1.17
	0	4.16	4.32
	2	6.10	6.47
	4	8.61	8.86
	5	9.73	9.97
	10	15.01	14.26

TABLE 3
PERFORMANCE of BLOCK THRESHOLDING ALGORITHM (100ms TIME WINDOW)

Signal	Input SNR (in dB)	BT (Hann window)	BT (Hamming window)
Music	-5	5.48	5.77
	0	11.90	11.83
	2	13.84	13.16
	4	13.59	11.72
	5	11.86	9.99
	10	11.33	10.16
Speech	-5	1.69	1.85
	0	4.86	5.12
	2	7.32	7.67
	4	9.73	9.94
	5	10.89	10.94
	10	13.72	12.31

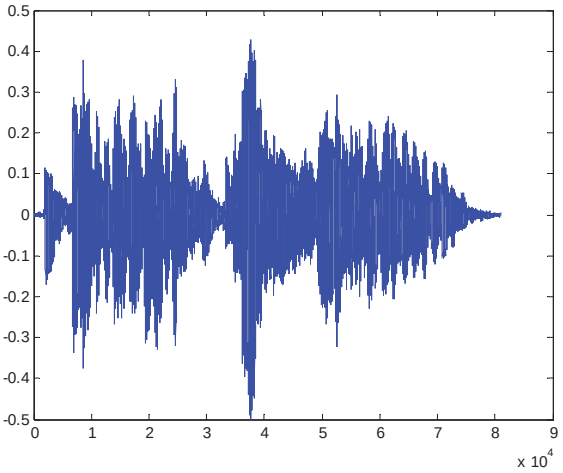

Fig. 2 Graph of original musical signal

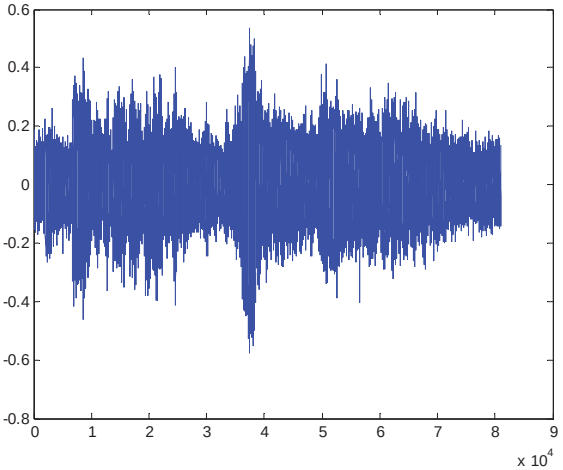

Fig. 3 Graph of noisy musical signal (4 dB SNR)

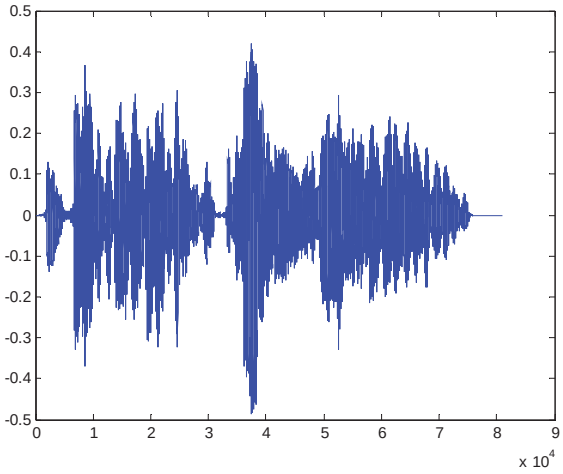

Fig. 4 Graph of denoised musical signal

VII. CONCLUSIONS

Adaptive block thresholding which is the non diagonal estimation technique is used to reduce noise from musical and speech noisy signals. Short time Fourier transform of the noisy audio signal is computed and the resulting coefficients is processed to reduce the noise. Gaussian white noise is used to contaminate the audio signals. Results show that better SNR ratio of audio signals is obtained after performing block thresholding procedure and also the SNR ratio of block thresholding when Hamming window is used is greater than SNR ratio of block thresholding when Hann window is used for low input SNR ratio. Also SNR ratio of block thresholding when time window of 100ms is used is greater than SNR ratio of block thresholding when time window of 50ms is used for low input SNR ratio.

REFERENCES

[1] K.P. Obulesu and P. Uday Kumar, "Implementation of Time Frequency Block Thresholding Algorithm in Audio Noise Reduction," International Journal of Science, Engineering and Technology Research (IJSETR), Volume 2, Issue 7, July 2013.

[2] Lalitha kumari, Karunakar Reddy, Hari Krishna and Venkata Subash, "Time-Frequency Block Thresholding Approach for Audio Denoising," International Journal of Advances in Science and Technology, Vol. 2, No. 5, 2011.

[3] http://en.wikipedia.org/wiki/Short-time_Fourier_transform

[4] S. S. Joshi and Dr. S. M. Mukane, "Comparative Analysis of Thresholding Techniques using Discrete Wavelet Transform," International Journal of Electronics Communication and Computer Engineering, Volume 5, Issue (4) July, 2014.

[5] Srinidhi S Shetty, Reeja S R, "Audio Noise Removal – The State of the Art," International Journal of Computational Engineering Research, Vol 04, Issue 12, December 2014, ISSN (e): 2250 - 3005, pages 34 -37.

[6] http://in.mathworks.com/help/signal/ref/hann.html

[7] http://in.mathworks.com/help/signal/ref/hamming.html

Surface Roughness analysis in High Speed Turning of Ti-6Al-4V

Grynal D'Mello[#1], P. Srinivasa Pai[#2], Puneet N. P.[#3]

[#]*Assistant Professor, Department of Mechanical Engineering,*
NMAMIT, Nitte, Karkala, Udupi, Karnataka - 574-110, Affiliated to VTU – Belgaum.
[1]grynal@nitte.edu.in

[#]*Professor, Department of Mechanical Engineering,*
NMAMIT, Nitte, Karkala, Udupi, Karnataka - 574-110, Affiliated to VTU – Belgaum.
[2]srinivasapai@nitte.edu.in

***Abstract*— Surface roughness of the machined work piece is an important product quality characteristic. Ti-based alloys are used in aerospace and other industries where surface finish requirement is high. This paper discusses the analysis of surface roughness parameters (R_a and R_z) in high speed turning of Ti-6Al-4V. Experiments have been conducted using coated and uncoated carbide inserts with and without the application of coolant. Multi Layered Perceptron (MLP), a widely used supervised ANN model has been investigated considering cutting parameters, tool wear, cutting tool vibration and application of coolant to model surface roughness parameters. It has been found that cutting tool vibrations have a significant effect on surface roughness and tool wear is less significant. Coated carbide inserts produced better surface finish than uncoated carbide inserts. MLP models have been successfully used to model surface roughness parameters with 100% prediction accuracy on test data.**

***Keywords*— Surface roughness, tool wear, cutting tool vibration, coolant, Artificial Neural Network**

I. INTRODUCTION

Surface roughness, dimensional precision and reliability of the product are some of the factors which can affect the performance of mechanical parts and production costs. Pal and Chakraborthy (2005) say surface roughness is one of the crucial performance parameter [1]. Achieving good surface finish during machining is a complicated process as different materials have different kinds of machining behaviour based on the composition of the material, cutting conditions, selection of tools etc. Titanium and its alloys are used in making products for aerospace, automotive, biomedical, marine, mining, railway, oil and piping industry [2]. They are considered as important engineering materials for industrial and aerospace applications because of its high strength to weight ratio, good resistance to corrosion and fatigue resistance. These materials are expensive and its properties like high thermal conductivity and chemical reactivity with cutting tools make titanium materials difficult to machine. The low machinability of titanium alloys due to the low thermal conductivity and high micro hardness of these materials leads to severe and premature tool wear in dry machining process [3]. Seikman have commented that "machining of titanium and its alloys would always be a problem, no matter what techniques are employed to transfer this metal into chips" [4]. Chemical reactivity of titanium with most of the materials results in either chemical reaction of the tool at high temperatures or rapid dissolution of the tool material in the chip [5].

Cutting tool vibration is one of the parameter that can affect the quality of surface finish. Low modulus of elasticity of titanium alloys was considered as the main cause of chatter during machining, as the deflection of titanium takes place nearly twice as much as carbon steel. This causes spring back behind the cutting edge which results in premature flank wear, vibration, and higher cutting temperatures [6]. Supply of coolant is of major concern while achieving good surface finish. High cutting temperature is generated during the high speed machining because of which there will be higher wear rate of the tool insert. Tool wear is directly dependent on the cutting velocity and the index of diffusion coefficient, followed by feed rate and the depth of cut [7].

Artificial Neural networks have been gaining lot of importance in the field of machining specially in modelling of surface roughness. Vikas Upadhyay et al. developed a neural network model considering feed rate and depth of cut along with vibration in radial and tangential directions as input and surface roughness as an output parameter [8].

With this background this work is an attempt to analyse surface roughness in high speed turning of Ti-6Al-4V using cutting vibration signals and tool wear. Coated and uncoated carbide inserts have been used during turning and its results have been compared with and without the application of coolant during machining. Multi layered perceptron (MLP) neural network models have been developed in order to understand the significance of cutting conditions, tool wear, cutting tool vibrations and the use of coolant on surface roughness parameters R_a and R_z.

II. EXPERIMENTAL SETUP AND DETAILS

A. Work Material

High speed turning experiments were performed on a high speed turning centre (HMT Make Stalion 100 SU) with

a speed range of 100 to 3500 rpm, on commercially available Ti-6Al-4V grade 5 alloy of diameter 50 mm and 200 mm length. The work material has the following chemical compositions in percentage of weight: Al – 6.02%, Cr – 0.03%, Fe – 0.13%, Mn – 0.04%, V – 3.85%, Ti – 89.93%. Typical hardness in the annealed condition is Rockwell C 30-34, and about Rockwell C 35-39 in the solution and aged condition.

B. Tool Inserts

Experiments were carried out using two types of inserts – (i)The uncoated carbide insert is 883 with MR4 chip breaker (SECO make) and (ii) the coated carbide insert is TP 2500 (SECO make). The specifications of the inserts are CNMG 12 04 08, which is flat faced and rhomboidal in shape with back and side rake angle of -6°, end cutting edge angle of 5° and tool nose radius of 0.8 mm. The tool holder used is PCLNL 2020 K12 (SECO make).

C. Experimental Conditions

Since the focus of this work has been correlating vibration signals and flank wear with surface roughness parameters using uncoated and coated carbide inserts, with and without coolant, experiments have been conducted at one speed, feed and depth of cut namely 150 m/min, 0.15 mm/rev and 0.8 mm respectively. This is considered as lower speed, feed rate and depth of cut in the complete scheme of experimentation. The depth of cut is equal to the nose radius of the inserts used. Experiments have been conducted with and without coolant. The coolant used was water-based mineral oil (Castrol Cool Edge B1) and was used in flooded condition. The coolant was supplied using a pump. A nozzle was used to direct the coolant at the interface of the tool and the workpiece in order to achieve better penetration. The discharge of the pump is 160 lpm.

D. Measurement of Flank wear

The flank wear experienced by the inserts were measured using Mitutoyo make Tool makers' microscope (TM 505 / 510) with a magnification of 15X and has a least count of 0.005 mm. The flank wear was measured after every cut (length of cut was 20 mm during machining using uncoated carbide insert and 40 mm with coated carbide insert). These studies were based on preliminary investigations. For uncoated carbide inserts, to have a better understanding of their wear behaviour, a smaller length of cut was used. But this resulted in a large number of cuts (45) to reach its limiting value. Hence for coated carbide inserts, the length of cut was increased to 40 mm, which was also based on the ability to have three machining passes for each length of the workpiece bar. Maximum flank wear (VB_{max}) was considered for measurement, which was measured at the end of every cut.

E. Measurement of cutting vibration signals

The cutting vibration signals were measured using a Model 65-10 Isotron® triaxial accelerometer (Meggitt make) fastened to the tool holder tightly using binding wire and then a cellophane tape was used to protect the accelerometer. This was fixed as close to the cutting zone as possible during the turning operations. This is not a preferred method for fixing the accelerometer, a more effective method would be fixing it through an insulation screw hole. The accelerometer sensed the vibration signals in the x, y and z directions i.e., depth of cut, speed and feed directions respectively. The signals along the cutting speed direction (v_y) are more sensitive to the flank wear and other machining phenomena during turning. Thus this has been considered for evaluation. The sensed vibration signals were sent to a DNA-PPCx and then to a PC (or laptop through Power DNA cube (UEI make)) with LABVIEW based display software (.vi) for display and storage.

F. Measurement of surface roughness parameters

Surface roughness was measured offline after the turning using a stylus type instrument, Taylor Hobson Taly Surf 50. Surface roughness parameters R_a (Arithmetic average surface roughness) and R_z (Maximum peak to valley height of the profile within a sampling length) [16] were measured for a sampling length of 2.5 mm. Surface roughness was measured at three different locations 120^0 apart on the surface of the work piece and average value has been considered.

III. RESULTS AND DISCUSSION

A. Tool Wear

As per ISO 3685, standard, a value of 0.4 mm has been considered as the limiting value for VB_{max} [9]. Machining was carried out for a length of 20mm and it took 45 cuts to reach a flank wear of 0.31mm for uncoated carbide insert. For coated inset, machining was carried out till a flank wear of 0.4 mm, which was reached in 10 cuts, which was the limiting value. Fig. 1 shows the variation of flank wear with number of cuts for coated inserts with and without coolant and fig. 2 shows the variation of flank wear with number of cuts for uncoated carbide insert with and without coolant. Only data of last 10 cuts have been considered in this study and comparison has been done.

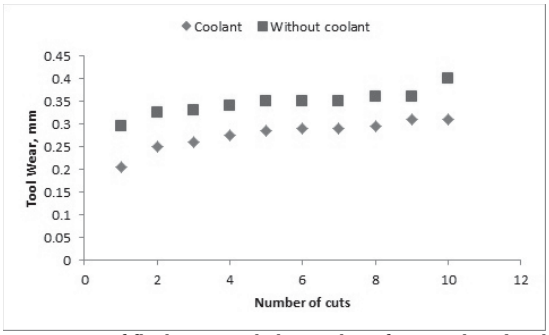

Fig. 1 Variation of flank wear with the number of cuts with and without coolant (coated carbide insert)

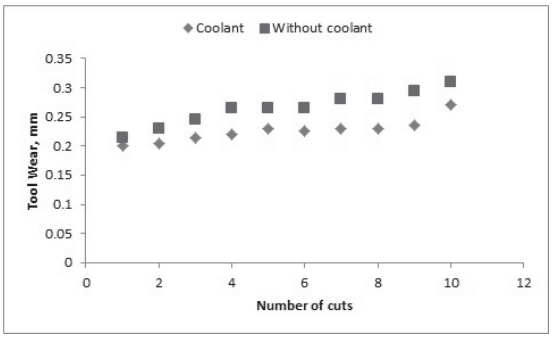

Fig. 2 Variation of flank wear with the number of cuts with and without coolant (uncoated carbide insert)

It can be seen that there is a gradual increase in flank wear with cutting time for uncoated carbide insert, whereas it is almost uniform in case of coated carbide insert. Coated carbide insert was found to reach higher flank wear, when compared to uncoated carbide insert. Wear development occurred in three stages – initial, gradual and abnormal beyond 0.4 mm, as reported by Jawaid et al., when titanium alloy was machined using coated and uncoated carbide tools [10]. This also establishes the superiority of straight tungsten carbide cutting tools in machining titanium alloys, as reviewed by Ezugwu [11].

The tool wear behaviour, using coolant is almost similar when compared to that without the use of coolant. The application of coolant has reduced the rate of flank wear for the considered speed, feed and depth of cut. Coated carbide insert is more sensitive to the use of coolant, than when using uncoated carbide insert. This shows the difference in the mechanism of tool wear, where severity is more for coated carbide inserts. The coolant is more effective, if it penetrates into the tool-chip and tool-work piece interfaces during the cutting process and high pressure coolant has been found to be more effective in machining titanium alloys [12].

B. Surface roughness and cutting tool vibration

R_a is considered as the widely used surface roughness parameter which has been analyzed by most of the researchers [13]. Fig. 3(a) to 3(d) shows the variation of surface roughness parameters and cutting tool vibrations with the number of cuts for coated carbide inserts with and without coolant. As the tool wear gradually increases (Fig. 1), the surface roughness parameter R_a shows an increasing trend. Variation of cutting tool vibration with the number of cuts follow a similar trend as that of surface roughness parameters, more particularly with R_z. R_z exhibits higher values when compared to R_a. This shows that cutting tool vibrations have a direct influence on variation in surface roughness parameters which can be caused due to the spring back effect while machining titanium alloys [17]. There is also self-excited vibration between the cutting tool and work piece [12]. But the spring back effect is more dominant. This is according to Campbell (2006) as cited in Pramanik A in a review on problems and solutions in machining titanium alloys, which reported that bouncing action takes place as the cutting edge enters the machining process under pressure [18]. Machining using coated carbide insert without coolant showed lower values of surface roughness parameters when compared to machining with the coolant.

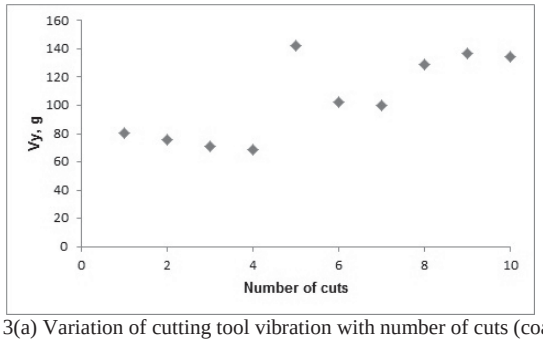

Fig. 3(a) Variation of cutting tool vibration with number of cuts (coated carbide insert with coolant)

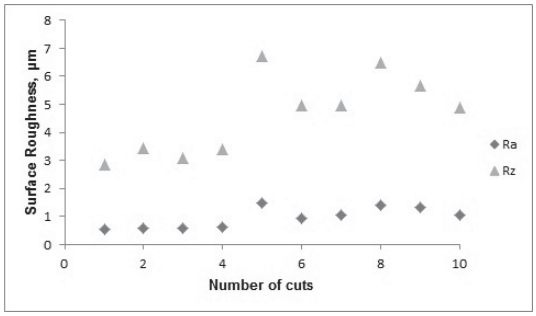

Fig. 3(b) Variation of surface roughness parameters with number of cuts (coated carbide insert with coolant)

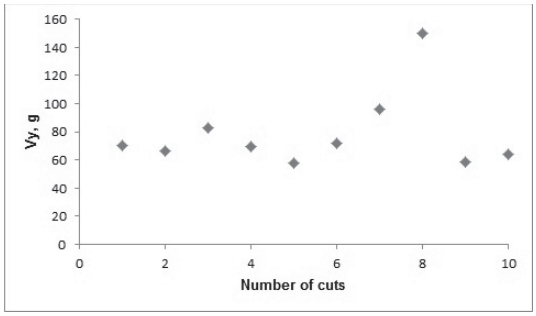

Fig. 3(c) Variation of cutting tool vibrations with number of cuts (coated carbide insert without coolant)

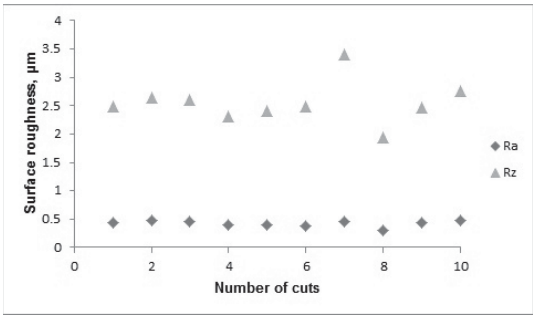

Fig. 3(d) Variation of surface roughness parameters with number of cuts (coated carbide insert without coolant)

Fig. 4(a) to 4(d) shows the variation of surface roughness parameters and cutting tool vibrations with the number of cuts for uncoated carbide inserts with and without coolant. Surface roughness show a similar behaviour as that of variation of cutting tool vibrations. Cutting tool vibrations exhibit lower values for uncoated carbide inserts when compared to coated carbide inserts for both cases of with and without coolant. As the coating in the coated carbide insert wears out, the substrate of the tool surface will be directly in contact with the work piece, which produces friction during machining generating more vibrations [14]. Surface roughness values are lower for uncoated carbide insert with coolant, whereas for without coolant, the values are higher.

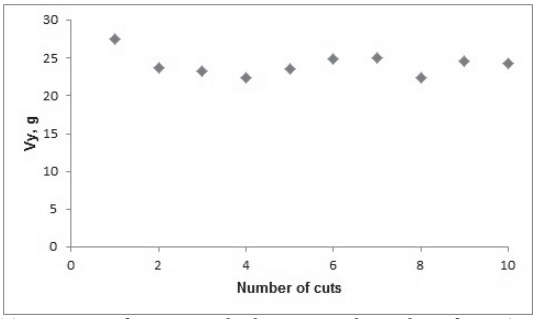

Fig. 4(a) Variation of cutting tool vibrations with number of cuts (uncoated carbide insert with coolant)

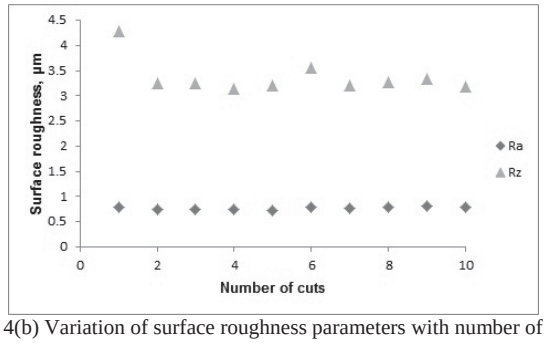

Fig. 4(b) Variation of surface roughness parameters with number of cuts (uncoated carbide insert with coolant)

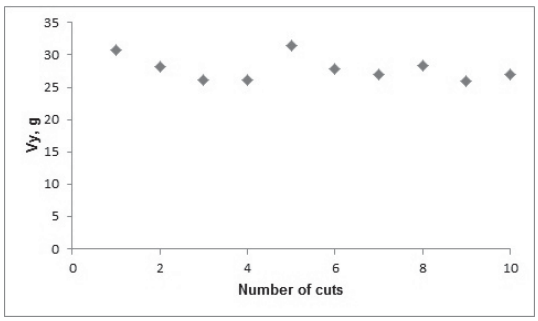

Fig. 4(c) Variation of cutting tool vibrations with number of cuts (uncoated carbide insert without coolant)

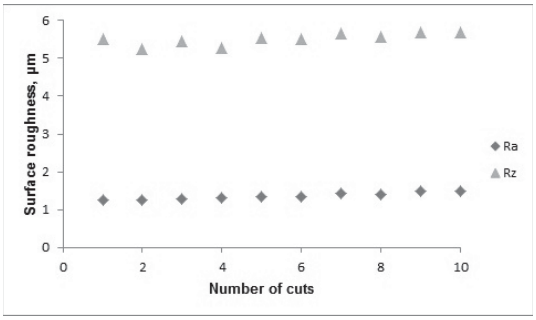

Fig. 4(d) Variation of surface roughness parameters with number of cuts (uncoated carbide insert without coolant)

IV. ARTIFICIAL NEURAL NETWORK (ANN) MODELING

Neural networks are widely used artificial intelligence tools which simulate the working of the human brain which are suitable for modelling various manufacturing functions due to their ability to learn complex non-linear and multivariable relationships between process parameters [15]. In this study feed forward multi layered neural network has been used to model the surface roughness parameters.

A. Multi Layered Perceptron (MLP)

Fig. 5 shows the most commonly used ANN architecture, a multi layered perceptron (MLP) [15]. It has three types of layers; an input, an output and the hidden layers. Hidden and output layers are composed of some number of neurons that perform nonlinear transformation of the signal. The output layer sums up the resulting vector from the hidden layer(s), thus providing the network's overall outputs.

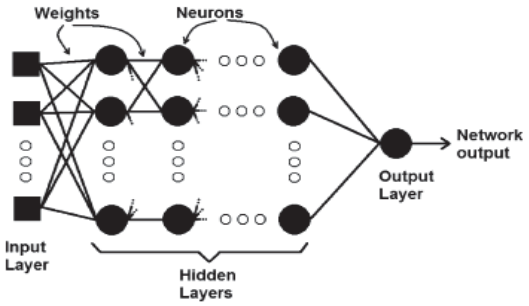

Fig. 5 The MLP ANN architecture

Each input is given to the network; the output is compared with the target value. The network is trained to perform a particular function by varying the weights between the neurons. After the output is given by the network, mean square error will be calculated between the target output and predicted output from neural network. The mean square error (MSE) can be reduced by varying the number of hidden layer neurons and simulation parameters and training the network [15].

The MSE is calculated as

$$\text{MSE} = \frac{(\textit{Predicted value} - \textit{Experimental value})^2}{2} \qquad (1)$$

In this paper, the MLP models have been developed using neural network tool box in MATLAB R2012a and comparison has been done between *tansigmoid* and *logsigmoid* transfer functions used in the hidden layer neurons. Four training algorithms have been used namely Levenberg-Marquardt (trainlm), BFGS Quasi-Newton (trainbfg), Scaled Conjugate Gradient (trainscg) and Fletcher-Powell Conjugate Gradient (traincgf) which are available in the tool box for training the neural network model. Two MLP models have been developed, one considering results for coated carbide insert with and without coolant, and other for uncoated carbide insert with and without coolant. This is mainly to understand and compare ANN modelling performance for coated and uncoated carbide inserts.

B. Model I

Cutting speed, feed rate, tool wear and cutting tool vibrations (V_y) are considered as inputs. In order to study the effect of coolant, binary representation has been used to represent the use of coolant as '1 0' and without coolant as '0 1' and surface roughness parameters R_a and R_z are the outputs, which have been evaluated individually. Twenty data has been collected from experimentation out of which 16 data has been considered as training data and remaining 4 as the test data. The hidden neurons have been varied randomly in order to obtain least mean squared error. The model has been trained individually using different training algorithms. In this study, mean squared error (MSE) of 0.001 has been taken as the desired goal and the network is trained until the target is reached. The learning rate of 0.01 and maximum number of epochs of 1000 has been selected. The number of neurons has been varied from 5 to 20.

Table 1 shows ANN modelling results considering coated carbide inserts with and without coolant for R_a and R_z. The optimum results obtained for different training algorithms along with the corresponding number of hidden neurons for the two transfer functions studied have been tabulated.

TABLE 1
MLP MODEL PERFORMANCE FOR R_A AND R_Z CONSIDERING COATED CARBIDE INSERT WITH AND WITHOUT COOLANT

R_a									
tansig					*logsig*				
Training algorithm	No. of hidden neurons	Epochs reached	Error reached	Prediction Accuracy (%)	Training algorithm	No. of hidden neurons	Epochs reached	Error reached	Prediction Accuracy (%)
trainlm	**11**	**5**	**0.000735**	**100**	*trainlm*	8	4	0.000806	100
trainbfg	19	24	0.000953	100	*trainbfg*	11	29	0.000986	100
trainscg	20	30	0.000945	100	*trainscg*	15	45	0.000991	100
traincgf	19	32	0.000944	100	***traincgf***	**6**	**34**	**0.000963**	**100**
R_z									
trainlm	**6**	**23**	**0.000937**	**75**	*trainlm*	12	27	0.000746	75
trainbfg	13	263	0.000925	50	***trainbfg***	**8**	**127**	**0.000945**	**75**
trainscg	11	1000	0.00277	75	*trainscg*	19	553	0.000989	75
traincgf	12	356	0.000958	75	*traincgf*	9	276	0.00134	75

TABLE 2
MLP MODEL PERFORMANCE FOR R_A AND R_Z CONSIDERING UNCOATED CARBIDE INSERT WITH AND WITHOUT COOLANT

R_a									
tansig					*logsig*				
Training algorithm	No. of hidden neurons	Epochs reached	Error reached	Prediction Accuracy (%)	Training algorithm	No. of hidden neurons	Epochs reached	Error reached	Prediction Accuracy (%)
trainlm	**7**	**2**	**0.000415**	**100**	*trainlm*	12	2	0.000276	100
trainbfg	9	11	0.000929	100	*trainbfg*	20	11	0.000991	100
trainscg	8	11	0.000970	100	*trainscg*	15	10	0.000763	100
traincgf	15	11	0.000997	100	***traincgf***	**5**	**10**	**0.000769**	**100**
R_z									
trainlm	**5**	**45**	**0.000981**	**100**	*trainlm*	16	4	0.000191	50
trainbfg	8	176	0.000997	100	*trainbfg*	14	94	0.000994	100
trainscg	5	853	0.000997	100	*trainscg*	10	349	0.000998	100
traincgf	9	205	0.000997	100	***traincgf***	**8**	**301**	**0.000998**	**100**

C. Model II

In this model, data obtained from experiments using uncoated carbide inserts have been considered. The modeling efforts have been made similarly as before. Twenty data were collected from experimentation out of which 16 data has been considered as training data and remaining 4 as the test data. The same simulation parameters used for model 1 have been used in model 2. Table 2 shows the ANN modelling results. The optimum results obtained for different training algorithms along with the corresponding number of hidden neurons for the two transfer functions have been tabulated.

D. Results and Discussion

From Table 1, for R_a it is seen that for both the transfer functions, the prediction accuracy is 100%. For *tansig*, *trainlm* provided a prediction accuracy of 100% with11 hidden neurons with an error of 0.000735 in 5 epochs whereas for *logsig*, *traincgf* produced a prediction accuracy of 100% with 6 hidden neurons, resulting in an error of 0.000963 for 34 epochs whereas for R_z, *tansig* with *trainlm* algorithm, the prediction accuracy has been found to be 75% which is less when compared to R_a.

Table 2 shows the model for R_a using uncoated carbide insert with and without coolant. It can be seen that for *logsig*, *traincgf* algorithm produced a prediction accuracy of 100% in 10 epochs for 5 hidden neurons with an error of 0.000769 whereas for R_z, *trainlm* algorithm with *tansig* transfer function obtained a prediction accuracy of 100% for 5 hidden neurons attaining 45 epochs with an error of 0.000981.

The results obtained from the neural network models for coated and uncoated carbide inserts with and without the application of coolants have been compared. It is seen that models developed for uncoated carbide inserts with and without the application of coolant showed better results when compared to coated carbide inserts. Also the models achieved its desired performance in less number of hidden neurons.

Fig. 6(a) and 6(b) shows the comparison of surface roughness parameters R_a and R_z both experimental and predicted using neural network for models considering coated and uncoated carbide insert with and without the application of coolant. It can be seen that in most of the cases, predicted values are closer to experimental values for uncoated carbide inserts than for coated carbide inserts.

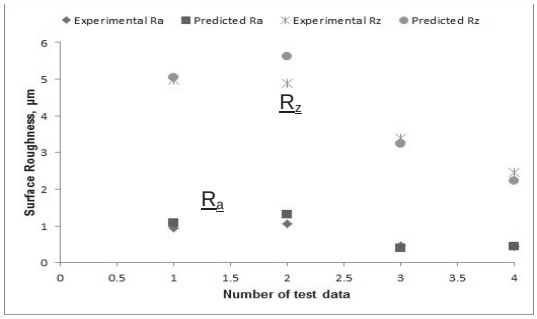

Fig. 6(a) Comparison of R_a and R_z both experimental and predicted using neural network for coated carbide insert with and without coolant

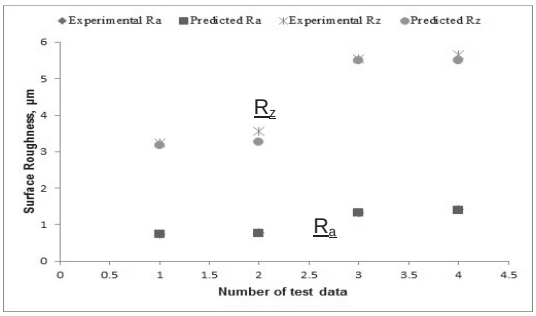

Fig. 6(b) Comparison of R_a and R_z both experimental and predicted using neural network for uncoated carbide insert with and without coolant

V. CONCLUSIONS

The present study focused on the analysis of surface roughness in high speed turning of Ti-6Al-4V using coated and uncoated carbide inserts, with and without the application of coolant. Experimental investigations have been carried out by correlating tool wear and cutting tool vibrations (V_y) with surface roughness parameters (R_a and R_z). MLP neural network models have been developed to understand the effect of cutting parameters, cutting tool vibrations, tool wear and use of coolant on surface roughness parameters using coated and uncoated carbide inserts. Different training algorithms have been used with *tansigmoid* and *logsigmoid* transfer functions to compare the prediction accuracies. The following conclusions can be made from this study:

- Tool wear has less effect on surface roughness parameters; whereas cutting tool vibrations have significant influence on surface roughness parameters.
- The effect of cutting tool vibrations on R_z is more significant than R_a.
- Application of coolant obtained good surface finish in case of uncoated carbide inserts than coated carbide inserts.
- Coated carbide inserts produced better surface finish than uncoated carbide inserts during machining without coolant.
- MLP model developed with uncoated carbide insert with and without coolant showed better performance when compared to model developed using coated carbide insert with and without coolant for modeling and prediction of R_a and R_z with 100 % prediction accuracy.

ACKNOWLEDGEMENT

The authors would like to thank AICTE, New Delhi for sponsoring this research project Ref. No.: 20/AICTE/RIFD/RPS(POLICY-1)/2012-13 under Research Promotion Scheme(RPS).

REFERENCES

[1] K. S. Pal and D. Chakraborty, "Surface roughness prediction in turning using artificial neural network", *Neural Comput & Applic*, Vol. 14, pp. 319–324, 2005.

[2] C. Bandapalli, M. B. Sutaria and V. D. Bhatt, "High Speed Machining of Ti-alloys- A critical Review", *Proceedings of the 1st International and 16th National Conference on Machines and Mechanisms (iNaCoMM2013)*, IIT Roorkee, India, Dec 18-20, 2013.

[3] M. Nouari and H. Makich, "Experimental investigation on the effect of the material microstructure on tool wear when machining titanium alloys: Ti-6Al-4V and Ti-555", *Int. Journal of Refractory Metals and Hard Materials*, Vol. 41, pp. 259-269.

[4] H. J. Siekman, "How to Machine Titanium", *Tool Engineer*, pp. 78-82, 1995.

[5] B. M. Kramer, D. Viens and S. Chin, "Theoretical consideration of rare earth metal compounds as tool materials for titanium machining", *CIRP Ann Manuf Technol*., Vol. 42, No. 1, pp. 111–114, 1993.

[6] E. O. Ezugwu and Z. M. Wang, "Titanium alloys and their machinability—a review", *J. Mater Process Technol*., Vol. 68, pp. 262–274, 1997.

[7] S. K. Choudhury and Srinivas, P., "Tool wear prediction in turning", *Journal of Materials Processing Technology*, Vol. 153–154, pp. 276–280, 2004.

[8] V. Upadhyay, P. K. Jain and N. K. Mehta,"In process prediction of surface roughness in turning of Ti-6Al-4V alloy using cutting parameters and vibration signals", *Measurement*, Vol. 46, pp. 154-160, 2013.

[9] ISO 3685, "Tool Life testing with Single-point turning tools", *ISO*, Geneva, 1993.

[10] A. Jawaid, C.H Che-Haron,. and A. Abdullah, "Tool wear characteristics in turning of titanium alloy Ti-6246", *Journal of Materials Processing Technology*, Vol. 92-93, pp. 329-334, 1999.

[11] E. O. Ezugwu, "High Speed Machining of Aero-Engine Alloys", *J. of the Braz. of Mech. Sci. & Eng.*, Vol. 26, No. 1, pp. 1-11, 2004.

[12] A. Pramanik, "Problems and solutions in machining of titanium alloys", *Int J Adv Manuf Technol.*, Vol. 70, pp. 919-928, 2014.

[13] B. Y. Lee and Y. S. Tarng, "Surface roughness inspection by computer vision in turning operations", *International Journal of Machine Tools & Manufacture*, Vol. 41, pp. 1251–1263, 2001.

[14] M. Khaisar and G. Devaputra, "Prediction of tool wear during turning of EN9 work material against coated carbide insert using vibration signal processing", *International Journal of Engineering and Research*, Vol. 3, No. 3, pp. 564-571, 2014.

[15] D. Karayel, "Prediction and control of surface roughness in CNC lathe using artificial neural network", *Journal of Materials Processing Technology*, Vol. 209, pp. 3125–3137, 2009.

[16] Taylor Hobson Precision, Measurement of Surface Finish_06/06, www.taylor-hobson.com, 2005.

[17] F. C. Campbell, "Manufacturing technology for aerospace structural materials", 1st edn. Elsevier, New York, 2006.

[18] Pramanik A., "Problems and solutions in machining of titanium alloys", *The International Journal of Advanced Manufacturing Technology*, Vol. 70, pp. 5-8, 2014.

Performance of Concrete Using Lime Sludge, Rice-Husk Ash and Foundry Sand

Nishanth K S[#], Pushparaj A Naik[*]

[#]*PG student, Department of Civil Engineering*
NMAMIT, Nitte, Karkala, Udupi, Karnataka - 574-110, Affiliated to VTU – Belgaum.
[1]ksnishanth22@gmail.com

[*]*Assistant Professor, Department of Civil Engineering*
NMAMIT, Nitte, Karkala, Udupi, Karnataka - 574-110, Affiliated to VTU – Belgaum.
[2]pushparajmanai@yahoo.com

***Abstract* — Due to increase in construction activities there is increase in demand for concrete, which leads to overuse of natural resource. Hence conservation of natural resources is necessary thing. This research work was experimentally carried out to investigate the effects of partially replacing PPC by Lime Sludge (LS), Rice-Husk Ash (RHA) and Fine aggregate by Foundry Sand (FS) in concrete at optimum replacement level which help to reduce the cost of concrete. The strength properties and water absorption of concrete were evaluated for mixes of M25 grade concrete. Incorporation of LS, RHA and FS in concrete increased water demand also strength was found to be higher for 6% replacement of PPC by RHA and 15% - 30% replacement of fine aggregate by FS. The obtained results were evaluated with respect to conventional mix.**

***Keyword* — Lime Sludge (LS), Rice-Husk Ash (RHA), Foundry Sand (FS), Pozzolanic Portland cement (PPC), Compressive Strength, Tensile Strength, Flexural Strength.**

I. INTRODUCTION

A. *General*

Concrete is second largest material consumed on the earth after water. It is the best material to achieve required qualities such as strength, durability, impermeability, fire resistance and abrasion resistance. Nowadays due to rapid growth in construction industries we are facing the scarcity of natural resources such as river sand and coarse aggregate, also the burden on the raw materials used in the manufacturing of cement. Due to growth of industrialization large amount of wastes are generated which is hazardous to environment and living beings. The wastes generated from industrial and agricultural sectors can be utilized as alternative construction material. In the present work lime sludge (LS), rice-husk ash (RHA) is used as substituent for cement and foundry sand (FS) is used as substituent for fine aggregate.

B. *Paper Mill Lime Sludge*

About 8.4 – 11.2 MT/Annum of paper are produced all around the world. In paper mill sodium hydroxide is used to convert the wood chips to pulps for paper production this process leads to formation of sodium carbonate. Calcium oxide is used to convert this sodium carbonate back to sodium hydroxide during this process calcium carbonate is produced also contains saturated hydrated lime known as lime mud or lime sludge. This industry generates a huge amount of solid waste. These solid wastes can be utilized as an additive in concrete. [1][2]

TABLE 1
Chemical Composition of LS

Insoluble Residue	1.92%
Calcium Oxide	75.59%
Silica, Alumina and Ferric Oxide	16.28%
Magnesium Oxide	0.34%
Moisture Content	0.18%

C. *Rice-Husk Ash*

Rice-husk is an agricultural waste produced in a large quantity during milling of paddy. About 22 million ton of paddy is produced per year, out of which 25% of RHA is generated when rice-husk is burnt, and it's estimated about 70million tonnes of RHA are generated annually which is a great environmental threat. This RHA contain 85% - 90% of amorphous silica (when controlled burning process adopted), which exhibits a good pozzolanic property and it can be used in concrete which contributes high strength and impermeable. [3][4]

TABLE 2
Chemical Composition of RHA

Silica	88.64%
Al_2O_3	1.23%
Fe_2O_3	1.19%
Carbon	2.33%
CaO	1.09%
MgO	1.76%
K_2O	1.98%
Other	1.78%
Moisture	1.87%

D. *Foundry Sand*

Foundry sand is a byproduct of ferrous and non-ferrous metal casting industry. It is high quality silica sand with

uniform physical characteristics which is used for molding because of its high thermal conductivity. The raw sand used is of higher quality than river sand used in construction site. Mainly this silica sand rely upon the betonites clay to act as binding material. This sand used for number of times before it becomes a byproduct, only 10% of sand is reused and rest of the sand will be dumped in to barren land. Thus the scarcity of river sand can be reduced up to some extent by using this waste sand as an alternative material which also satisfies some of the specification of fine aggregate. [5][6]

II. LITERATURE REVIEW

A. *Study on the strength of concrete by using lime sludge as a partial replacement of cement.*

- Dunster A.M (2007), had studied the potential application of paper sludge and sludge in construction products. He had investigated that the paper sludge and sludge ash are potentially useful in the production of cement and blended cement. [7]
- Rajgor M.B and Pitrodo J (2013), they had investigated the potential use of paper industry waste (hypo sludge) as a supplementary cementitious material used in concrete. They had observed a higher strength achieved at 30% replacement of cement by paper industry waste.[8]
- Sahu V and Gayathri V (2013), this paper outlines the utilization of fly ash and lime sludge together in mortar mix. They had observed increase in strength with increase in age of mortar, by increasing lime sludge in a mix simultaneously decreasing in fly ash when compared to other mix. [9]

B. *Study on the strength of concrete by using rice-husk ash as a partial replacement of cement.*

- Oyetolo E.B and Abdullahi M (2006), preliminary analysis performed on hollow sandcrete block using RHA, were cement is replaced by RHA (10% - 50%). Higher strength is achieved at 20% replacement. [10]
- Ramezanipour A.A et al. (2009), this paper provide the information about the influence of RHA in concrete. Result showed that concrete incorporating RHA had higher strength, elasticity and more durable. [11]
- Habeeb G.A and Mahmod H.B (2010), outline of this paper gives the properties of RHA produced by using ferro-cement furnace. Incorporation of RHA in concrete increases a water demand, also showed an excellent improvement in strength for 10% replacement of cement without adverse effect. [12]
- Bakar B.H.A et al. (2010), they worked on the potential use of RHA in concrete. Due to high pozzolanic activity, both strength and durability of concrete can be enriched, also make concrete highly dense and less porous. [13]
- Kumar S (2012), experimental study was carried to find the suitable alternative construction materials such as RHA, saw dust, brick bats etc. It was found that setting time of concrete increases with increase in RHA, also achieved a required strength when cement is replaced at 20% of RHA. [14]

C. *Study on the strength of concrete by using foundry sand as a partial replacement of fine aggregate.*

- Naik T.R et al. (1994), they had investigated the performance of concrete using discarded foundry sand in place of fine aggregate. Mix with used foundry sand showed a result of 20% - 30% lower strength but a mix with clean/new foundry sand showed a same result compared to control mix. [15]
- Naik T.R et al. (1996), they had investigated the performance of foundry byproduct as an alternative material in construction. They have studied the performance of concrete using foundry slag replacing fine aggregate, they had observed an acceptable strength with 100% replacement of fine aggregate. Also the strength of masonry blocks was evaluated by replacing the fine aggregate by 35% foundry sand, which had passed the ASTM requirements. [16]
- Naik T.R and Singh S.S (1997), study was carried out to evaluate the use of foundry sand on the properties of flowable slurry. This mix composed of used foundry sand with fly ash, which is evaluated for bleeding, depth of nail penetration, shrinkage and strength. The result showed that optimum strength was observed at 30% - 50% replacement of fine aggregate. [17]
- Naik T.R et al. (2003), study was performed to evaluate the strength, freezing and thawing of concrete. Fine aggregate was replaced by foundry sand and cement was replaced by fly ash. Result showed a negligible reduction in strength, freezing and thawing. But 35% of foundry sand can be used since it has achieved required strength as per ASTM. [18]
- Siddique R et al. (2008), mechanical property of concrete were evaluated by using foundry sand as partial replacement of fine aggregate. Required strength is achieved when fine aggregate was replaced by 30% foundry sand. [19]

III. AIM and OBJECTIVES of PRESENT WORK

The main objective of present work is to utilize a wastes generated from industrial and agricultural sector as an alternative material for cement and fine aggregate. So that environmental pollution can be reduced and burden on the raw materials used for manufacturing of cement can be overcome up to some extent. Scarcity of the river sand can be overcome up to some extent and make concrete quite economical.

A. *Aim of the work*

- This study attempts to determine the strength and optimum replacement of cement by lime sludge, rice-husk ash and fine aggregate by foundry sand.
- To determine the strength of concrete when foundry sand is blended with lime sludge and rice-husk ash.
- Cost comparison of concrete using lime sludge, rice-husk ash and foundry sand with conventional concrete.

IV. MATERIALS

A. *Cement*

In the present work PPC fly ash based (Ultra-Tech) cement is used throughout the work. Physical properties are as shown in Table 3. [20]

Table 3 Physical properties of PPC

Characteristics	Obtained Value	Standard Value
Normal Consistency	33%	25% - 33%
Initial Setting	100 min.	Not less than 30 min.
Final Setting	220 min.	Not grater then 600 min.
Specific Gravity	3.02	3.15
Fineness	0%	Shall not exceed 10%

B. *Fine Aggregate*

The test were conducted as per IS 2386 (part 3): 1963, 4.75mm down size fine aggregate is used. Physical properties such as specific gravity - 2.65, water absorption - 2.0%, fineness modulus - 2.71 and aggregate confirming to zone II. [21][22]

C. Coarse Aggregate

The test were conducted as per IS 2386 (part 3): 1963, 20mm and down size coarse aggregate is used. A physical property such as specific gravity - 2.67, water absorption - 0.43%, and fineness modulus – 6.42. [22]

D. *Lime Sludge*

Lime sludge is collected from Mysore Paper Mill, Bhadravathi. Specific gravity - 2.58, fineness - 16% and pale white fine powdered appearance.

E. *Rice-Husk Ash*

Rice-husk ash is obtained from Shree Shree Goursundra Rice and Oil Mill, Orissa. Specific gravity - 2.18, fineness – 0% and grey black fine powdered appearance.

F. *Foundry Sand*

Foundry sand is obtained from Lamina Foundry Ltd. Nitte. Its specific gravity - 2.31.

G. *Mix Proportion*

Mix design of concrete is done as per IS 10262:2009, shown in Table 4 and type of mixes shown in Table 5. [23][24][25]

Table 4 Mix Proportion

Grade	Cement (kg/m^3)	Fine Aggregate (kg/m^3)	Coarse Aggregate (kg/m^3)	Water ($lit./m^3$)
M25	448	625.51	1100.07	197

Table 5 Type of Mixes

Type of Mixes	Description
CC	Conventional Concrete
FS_1	Fine Aggregate is Replaced by 15% FS
FS_2	Fine Aggregate is Replaced by 30% FS
FS_3	Fine Aggregate is Replaced by 45% FS
RHA_1	Cement is Replaced by 6% RHA
RHA_2	Cement is Replaced by 12% RHA
RHA_3	Cement is Replaced by 18% RHA
LS_1	Cement is Replaced by 10% LS
LS_2	Cement is Replaced by 20% LS
LS_3	Cement is Replaced by 30% LS
LS_4	Cement is Replaced by 40% LS
BM_1	15% FS + 6% RHA
BM_2	15% FS + 10% LS
BM_3	15% FS +6% RHA +10% LS

V. TEST on CONCRETE

Testes performed on concrete specimens are as follows

- Compressive strength.
- Split tensile strength.
- Flexural strength.
- Water absorption.

The strength parameters of concrete specimens were evaluated for 7 and 28 days of curing period. Compressive testing machine with capacity of 200T is used to perform compression and split tensile tests, universal testing machine with the capacity of 40T is used perform flexural test of beam. Results were presented graphically and tabulated as shown below.

Table 6 Compressive Strength of Concrete

Type of Mix	7 Days Strength (N/mm^2)	28 Days Strength (N/mm^2)
CC	33.93	47.33
LS_1	32.59	45.93
LS_2	22.74	33.41
LS_3	17.26	26.74
LS_4	13.33	21.34
RHA_1	33.93	47.56
RHA_2	28.00	41.76
RHA_3	24.29	40.00
FS_1	37.26	51.11
FS_2	34.00	47.63
FS_3	27.28	45.48
BM_1	29.41	44.0
BM_2	27.40	40.15
BM_3	28.52	42.82

The results of 28 days shows that the strength of RHA_1 is 0.49% higher,LS_1 is 2.96% lower, FS_1 is 7.98% higher, FS_2 is 0.68% higher, BM_1 is 7.04% lower, BM_2 is 15.2% lower and BM_3 is 9.53% lower. The above results were compared to conventional mix.

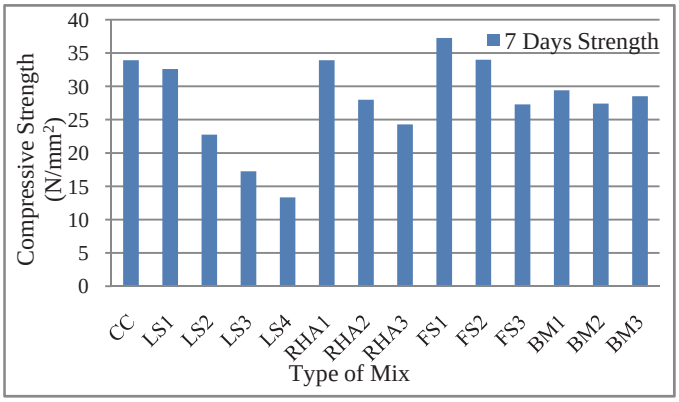

Fig.1 Compressive Strength of 7 Days

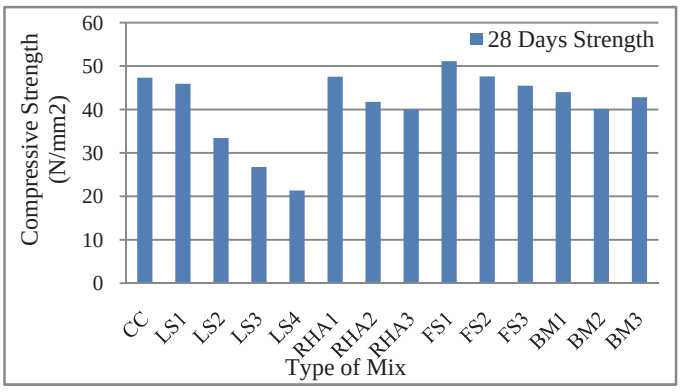

Fig.2 Compressive Strength of 28 Days

Table 7 Split Tensile Strength of Concrete

Type of Mix	7 Days Strength (N/mm^2)	28 Days Strength (N/mm^2)
CC	2.36	3.68
LS_1	2.19	3.63
LS_2	1.86	3.28
LS_3	1.43	2.97
LS_4	1.34	2.67
RHA_1	2.44	4.01
RHA_2	1.84	3.25
RHA_3	1.56	2.95
FS_1	2.57	3.75
FS_2	2.19	3.58
FS_3	2.09	3.43
BM_1	2.24	3.52
BM_2	2.24	3.37
BM_3	2.07	3.33

The results of 28 days shows that the strength of RHA_1 is 8.97% higher, LS_1 is 1.36% lower, FS_1 is 1.9% higher, FS_2 is 2.72% lower, BM_1 is 4.35% lower, BM_2 is 8.42% lower and BM_3 is 9.51% lower. The above results were compared to conventional mix

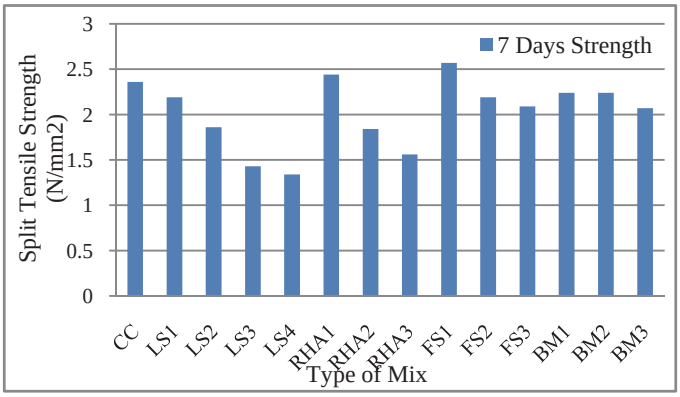

Fig.3 Split Tensile Strength of 7 Days

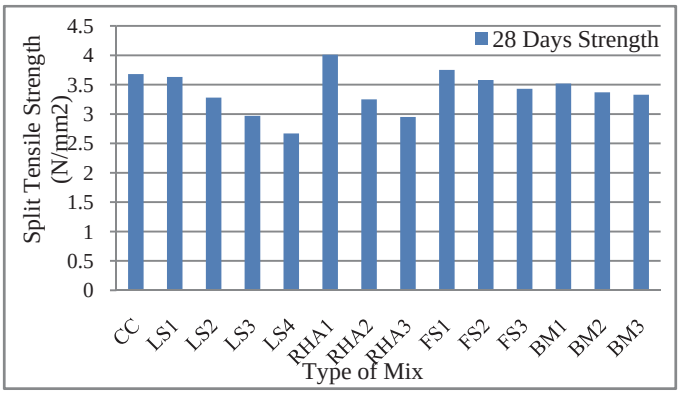

Fig.4 Split Tensile Strength of 28 Days

Table 8 Flexural Strength of Concrete

Type of Mix	28 Days Strength (N/mm^2)
CC	3.33
LS_1	3.31
LS_2	3.24
LS_3	3.17
LS_4	3.11
RHA_1	3.66
RHA_2	3.29
RHA_3	3.14
FS_1	3.31
FS_2	3.26
FS_3	3.24
BM_1	3.84
BM_2	3.64
BM_3	3.66

The results of 28 days shows that the of RHA_1 is 9.91% higher, LS_1 is 0.6% lower, FS_1 is 0.6% lower, FS_2 is 2.1% lower, BM_1 is 15.31% higher, BM_2 is 9.31% higher and BM_3 is 9.91% higher. The above results were compared to conventional mix.

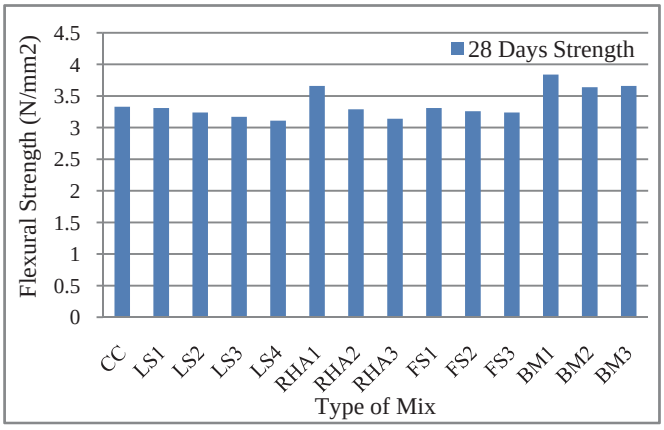

Fig.5 Flexural Strength of 28 Days

Table 9 Water Absorption of Concrete

Type of Mix	% of Water Absorption
CC	2.30
LS_1	2.82
LS_2	2.84
LS_3	2.90
LS_4	2.94
RHA_1	2.59
RHA_2	2.62
RHA_3	2.67
FS_1	1.78
FS_2	2.09
FS_3	2.26
BM_1	2.14
BM_2	2.31
BM_3	1.93

The result shows that percentage of water absorption is higher for RHA_{1-3}, LS_{1-4} and lower for FS_{1-3} and BM_{1-3}. The above results were compared to conventional mix.

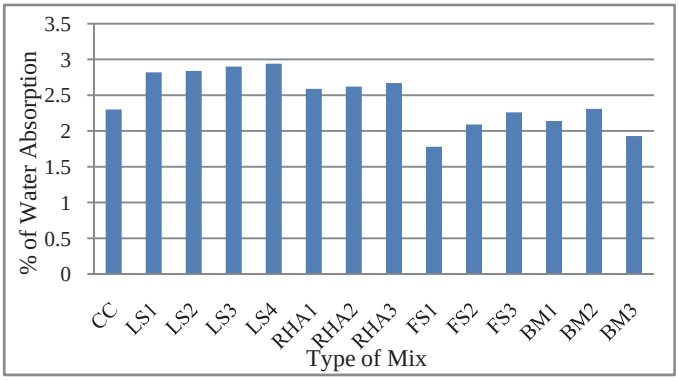

Fig.6 Water Absorption

VI. COST ANALYSIS

Concrete plays a vital role in construction industry because of its desired properties. But in present condition the cost of concrete is increasing due to the increase in cost of cement and natural resources such as fine aggregate and coarse aggregate. Hence to make concrete quite economical an alternative material can be used in the production.

In the present work cost analysis is carried for RHA_1, LS_1, FS_1, FS_2, and BM_{1-3}. The cost is compared with conventional concrete.

Table 10 Cost Comparison of Different Mixes with Conventional Mix

Sl. No.	Type of Mix	Cost /m^3
1	CC	3219.36
2	LS_1	3033.97
3	RHA_1	3228.60
4	FS_1	3192.71
5	FS_2	3166.26
6	BM_1	3201.93
7	BM_2	3007.33
8	BM_3	3016.50

The result shows that cost of LS_1 is 5.76% lower, RHA_1 is 0.28% higher, FS_1 is 0.83% lower, FS_2 is 1.66% lower, BM_1 is 0.54% lower, BM_2 is 6.59% lower and BM_3 is 6.30% lower. When compared to CC.

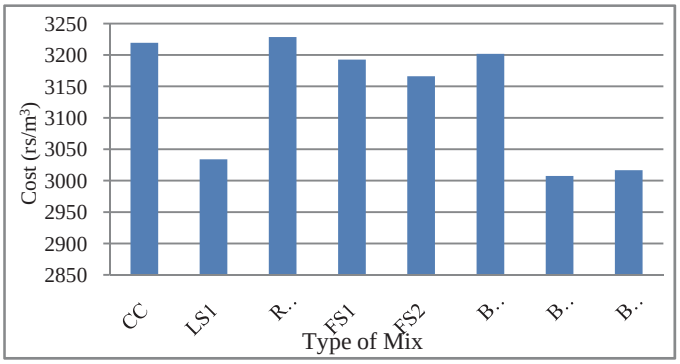

Fig.7 Cost Comparison

VII. CONCLUSION

- Test results show that these waste materials (LS, RHA and FS) can be efficiently utilized as a partial replacement of cement and fine aggregate.
- From the test results it's observed that the strength of concrete containing 6% RHA, 15% and 30% FS had shown a higher strength when compared to conventional concrete.
- The optimum strength of mix containing LS is achieved at 10% replacement, but obtained strength is relatively lower than conventional concrete.
- Strength of BM_1 is higher than BM_2 and BM_3, but obtained strength is relatively lower than conventional concrete.
- Strength goes on reducing with increase in content of RHA, LS and FS.
- From the obtained results it's found that, fine aggregate can be effectively replaced by 15% to 30% of FS.
- Cement can be effectively replaced by 0% to 10% of RHA and 0% to 10% of LS.
- Workability of RHA, LS and FS mixes is reduced when compared to CC.
- Water absorption of concrete increases with increase in content of RHA, LS and FS when compared to CC.
- From the cost analysis it shows that the cost of $FS_{1\text{-}2}$, $BM_{1\text{-}3}$ and LS_1 found to be economical and cost of RHA_1 is increased by 0.28% when compared to CC.
- Environmental pollution can be reduced by utilizing these wastes as alternative construction material.

ACKNOWLEDGMENT

The authors are thankful to our beloved HOD Dr. Srinath Shetty K, Principal Dr. N Chiplunkar and Faculty Members of Department of Civil Engineering NMAMIT, Nitte for their continuous support to carry out this research work.

REFERENCES

[1] Apurva Kulkarni, samruddha Raje, Juned Peerzada, Mamta Rajgor, "A Miiniscule Endeavour For Accomplishing Hypo Sludge Fly Ash Brick in Indian Contest", IJETT 2014 pp. 361-365.

[2] Ravindra Kumar, "Effect of Partial Replacement of Cement by Fly Ash and Lime Sludge on Strength Characteristics of Concrete", M.E Thesis, Thapar University Patiala, India 2013.

[3] Jayanthi Rajput, R K Yadav, R. Chandak, "The Effect of Rice-Husk Ash Used as Supplementary Cementitious Material on Strength of Mortar", IJERA 2013 pp. 133-136.

[4] www.ricehusk.com/details.htm

[5] Foundry Industry Recycling Starts Today, "Foundry Sand Facts for Civil Engineering", 2004.

[6] www.gitam.edu/resource/environmental/iwm_tsrinivas/pp_waste.htm

[7] Dr. Andrew M Duster, "Characterization of Mineral Waste Resource and Processing Technologies-Integrated Waste Management For the Production of Construction Material", 2007.

[8] Mamta B. Rajgor and Jayeshkumar Pitroda, "A Study on Paper Industry Waste: Opportunity for Development of Low Cost Concrete in Indian Contest", IJSR 2013 pp. 90-92.

[9] Vaishali Saho, V. Gayathri, "The use of Fly Ash and Lime Sludge as Partial Replacement of Cement in Mortar", IJETI 2014 pp. 30-37.

[10] E.B Oyetola and M Abdullahi, "The Use of Rice-Husk Ash in Low Cost Sandcrete Block Production", LEJPT 2006 pp. 58-70.

[11] A.A Ramezainan Pour, M. Mahdi Khani and Gh. Ahmadibeni, "The Effect on Mechanical Properties and Durability of Sustainable Concrete", IJCE 2009 pp. 83-91.

[12] Ghassan Abood Habeeb and Hilmi Bin Mahmud, "Study on Properties of Rice-Husk Ash and Its Use as Cement Replaced Mortar", 2010 pp. 185-190.

[13] Badoyul Hisham Abu Bakar, Ramadhansyah Putraja and Hamidi Abdulaziz, "Malaysian Rise-Husk Ash- Improving The Durability and Corrosion Resistance of Concrete: Pre-Review", APSEC 2010 pp. 6-13.

[14] Prof. R. Sathish Kumar, "Experimental Study on the Proportion of Concrete Made With Alternative Construction Material", IJMER 2012 pp. 3006-3012.

[15] Tarun R. Naik, Viral M. Patel, Dhaval M. Patel and Mathew P. Tharaniyil, "Utilization of Used Foundry Sand in Concrete", Journal of Material in Civil Engineering. 1994 pp 254-263.

[16] Tarun R. Naik, Shiw S. Singh, Mathew P. Tharaniyil and Robert B. Wendor, "Application of Foundry By-Product Materials in Manufacture of Concrete and Masonry Products", ACI Materials Journals. 1996 pp 41-50.

[17] Tarun R. Naik, Shiw S. Singh, "Flowable Slurry Containing Foundry Sands", Journal of Material in Civil Engineering. 1997 pp 93-102.

[18] Tarun R. Naik, Rudolph N. Kraus, Yoon-moon Chun, Bruce W. Ramme and Shiw S. Shingh, "Properties of Field Manufactured Cast-Concrete Products Utilizing Recycled Materials", Journal of Material in Civil Engineering. 2003 pp 400-407.

[19] Rafat Siddique, Geert De. Schutter and Albert Noumowe, "Effect of Used Foundry Sand on the Mechanical Properties of Concrete", Construction of Building Materials 2008 pp. 976-980.

[20] Bureau of Indian Standards 4031(part 5): 1988, "Method of Physical Test for Hydraulic Cement", New Delhi.

[21] Bureau of Indian Standards 383:1970, "Coarse and Fine Aggregates from Natural Sources for Concrete", New Delhi.

[22] Bureau of Indian Standards 2386(part 3):1963, "Methods of Test for Aggregates for Concrete", New Delhi.

[23] Bureau of Indian Standards 10262:2009, "Concrete Mix Proportioning", New Delhi.

[24] Bureau of Indian Standards 456:2000, "Plain and Reinforced Concrete", New Delhi.

[25] M. S. Shetty, Concrete Technology Theory and Practice, 7th edition S Chand Publication, 2013.

Effect of Partial Replacement of Cement and Complete Replacement of Fine Aggregate by Industrial Wastes on Strength Properties of Concrete Interlocking Paver Blocks

Gaurav P B[#], N Bhavanishankar Rao[*]

[#]*PG student, Department of Civil Engineering*
NMAMIT Nitte, Karkala, Udupi, Karnataka-574110, Affiliated to VTU - Belgaum
[1]gauravac39@gmail.com

[*]*Professor, Department of Civil Engineering*
NMAMIT NITTE, Karkala, Udupi, Karnataka-574110, Affiliated to VTU - Belgaum
[2]raonbs@yahoo.com

Abstract- **Concrete plays a vital role in most of the infrastructure development projects. Interlocking concrete paver blocks (IPB) now used extensively for pavements all over the world is also made up of concrete. The demand for cement is ever increasing which has also led to the overuse of river sand, limestone and other natural resources required for concrete manufacturing. There is a need to look for alternate construction material in order to adhere to sustainability and to overcome the problem of rising construction cost. In the present work an attempt has been made to study the suitability of using industrial wastes like Ground Granulated Blast Furnace Slag (GGBS) as a partial replacement to cement (10%, 20% and 30%) and quarry dust as a complete replacement for fine aggregate in concrete. Three different mixes are produced with cement partially replaced by GGBS and with quarry dust as fine aggregate.**

Keywords— **Interlocking paver block, ground granulated blast furnace slag, quarry dust, flexural strength, abrasion resistance.**

I. INTRODUCTION

A. General

Concrete is an important material in the construction field because of its ability to be cast into any shape when in plastic condition and as it hardens it possesses sufficient strength to withstand the loads acting on it. Concrete block pavement (CBP) was first used in the Netherlands in the early 1950s as a replacement for baked clay brick roads. The CBP gained popularity due to the fact that the cost of bitumen pavement was rising and also because of CBP's more aesthetic appearance, less construction cost and easy maintenance. Concrete is the most popular building material in the world. But production of cement consumes very high quantity of energy and has brought the limestone reserves to near depletion. River sand has been the most popular choice for the fine aggregate component of concrete in the past, but overuse of the material has led to environmental concerns, the depleting of securable river sand deposits and a concomitant price increase for the material. Therefore, it is desirable to obtain cheap, environmentally friendly substitutes for cement and river sand that are preferably by-products. [3] In the present work quarry dust is used as a complete replacement for fine aggregate and GGBS as a partial replacement for cement (10%, 20% and 30%).

B. GGBS

GGBS is obtained as a by-product in the manufacture of iron. Iron ore, coke and limestone are fed into the furnace and the resulting molten slag floats above the molten iron at a temperature of about 1500°C to 1600°C. Once the molten iron is tapped off, the remaining molten slag, which consists of mainly silicious and aluminous residue is then quenched rapidly using water, resulting in the formation of a glassy granulate. This glassy granulate is dried and ground to the required size, which is known as GGBS. GGBS has been in use for a reasonably long period due to the overall economy in its production as well as its improved performance characteristics in aggressive environments. In the last decade a great deal of research work has been conducted addressing the efficiency as GGBS is a kind of a industry waste that can act as economic and ecological resource for hardened concrete in enhancing its performance properties. [6]

C. Quarry Dust

Quarry dust can be defined as residue, tailing or other non-valuable waste material after the extraction and

processing of rocks to form coarse aggregate of various sizes. When boulders are broken into small pieces quarry dust is formed. It is grey in colour. Quarry dust is produced during the extraction and processing of stone aggregate. The quarry dust for the present work was obtained from Manjarpalke near Nitte, Karkala. The utilization of quarry fines is seen as a way to minimize the accumulation of unwanted material and at the same time to maximize resource use and efficiency.

II. LITERATURE REVIEW

- Ilangovana et al. (2008), carried out a study on the feasibility of the use of quarry rock dust as a complete substitution for fine aggregates in conventional concrete. Tests were conducted on cubes and beams to study the compressive and flexural strengths of concrete made of quarry rock dust. It was found that the strength of quarry rock dust concrete was comparatively 10-12% more than that of similar mix of conventional concrete.

- Hameed et al. (2009), studied the effect of crushed stone dust as fine sand and found the flexural strength increased than the concrete with natural sand upto an optimum level but the values decreased as the percentage of crusher dust was increased beyond that optimum value of replacement.

- Chandana Sukesh et al. (2013), carried out a study on partial replacement of sand with quarry dust in concrete. The study showed improvement in compressive strength of the concrete but the workability decreased with the increase in quantity of quarry dust. Adding fly ash in small quantities proved to improve the workability.

- El Nouhy, (2013) studied the effect and possibility of using Portland slag cement in the production of interlocking paving units. Tests were carried out in order to investigate the properties of the manufactured specimens at ages 28 and 180 days, respectively. Compressive strength and abrasion resistance tests were conducted according to the American Society for Testing and Materials (ASTM C418). Water absorption, split tensile strength, abrasion resistance, as well as, skid resistance tests were performed according to both Egyptian Standard Specifications (ESS 4382) and European Standard (EN 1338). The Egyptian standard is identical with the European standard. The results indicated that it is feasible to use Portland slag cement in the manufacture of paving blocks as the conditions of the conducted tests were satisfied at the age of 180 days except for the minimum split tensile strength test.

- Vijayakumar et al. (2013), in their study found that compressive strength increased with increase in glass powder. Based on the study, it was suggested that glass powder can be used as a cement replacement material up to particle size less than 75µm to prevent alkali silica reaction.

III. OBJECTIVES and AIM

This paper attempts to study the feasibility of the use of quarry dust as a complete substitution for fine aggregate in cement concrete with GGBS as partial replacement material for cement and thereby making concrete more economical.

IV. MATERIALS and METHODS

A. Cement

Ramco supergrade Portland Pozzolona flyash based cement conforming to IS1489 (Part-1) - 1991 is made use for the study [8]. Properties of the cement are given below.

TABLE 1
Properties of the PPC used

Property	Obtained value
Specific gravity	3.0
Initial setting time	130min
Final setting time	230 min
Normal consistency	31.75%

B. Fine Aggregate

Quarry dust was used as fine aggregates in this study. All the properties are tested as specified in IS: 2386 (Part III)-1963[7]. The results are shown below.

TABLE 2
Properties of Quarry Dust

Property	Value
Specific Gravity	2.68
Water Absorption	5%
Fineness Modulus	3.5
Surface Texture	Smooth

Quarry dust conforming to Zone III (As per IS: 10262-2009)

C. Coarse Aggregate

The coarse aggregate used are of 10mm and downsize. The properties of the aggregates as obtained from the tests performed according to IS: 2386 (Part III)-1963 are given below [7].

Table 3 Properties of Coarse aggregate

Property	Value
Specific Gravity	2.75
Fineness Modulus	6.29
Water Absorption	0.285

D. GGBS

Ground granulated blast furnace slag was obtained from JSW cement Ltd. Its specific gravity was 2.93. GGBS is a white colored fine powder.

E. Mix Proportioning

Mix design of concrete was carried out as per IS: 10262: 2009, IS: 10262:1982, IS: 456: 2000 and conforming to specification given by IRC: SP: 63: 2004. [9] [10] [11] [13].

TABLE 4
Mix Proportioning of Conventional Mix (CM)

Grade	Cement (Kg/m^3)	Fine Aggregate (Kg/m^3)	Coarse Aggregate (Kg/m^3)	Water ($liters/m^3$)
M40	410	907.63	972.58	180

Table 5 Type of Mixes

Mix Designation	Description
CM	Conventional Mix
GG_1	PPC+10% GGBS+ Quarry Dust+ CA
GG_2	PPC+20% GGBS+ Quarry Dust+ CA
GG_3	PPC+30% GGBS+ Quarry Dust+ CA

V. TESTS ON CONCRETE

Tests were conducted on the concrete to ascertain the strength parameters at age 7 and 28 days. Following tests were performed according to IS: 15658:2006[12]:-

- Compression test using Compression Testing Machine (CTM of 200T capacity).The compressive strength of individual paver blocks shall not be less than 85% of specified strength.
- Split tensile test –CTM.
- Flexural strength test- Universal Testing Machine.
- Abrasion test- Tile/Dorry Abrasion Testing Machine.
- Water absorption Test (should be less than 7%)

Table 6 Compression Test Results

Mix Type	Compressive Strength At 7 Days (N/mm^2)	Compressive Strength At 28 Days (N/mm^2)
CM	35.67	44.48
GG_1	36.44	45.78
GG_2	36.88	46.22
GG_3	37.33	47.56

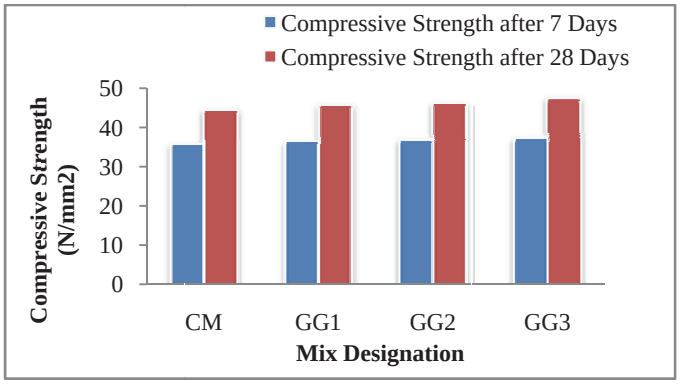

Fig.1 Effect of cement replacement percentages by GGBS on compressive strength.

Table 7 Tensile Splitting Test Results

Mix Type	Tensile Splitting Strength At 7 Days (N/mm^2)	Tensile Splitting Strength At 28 Days (N/mm^2)
CM	1.703	2.06
GG_1	1.92	2.13
GG_2	1.343	1.95
GG_3	1.229	1.77

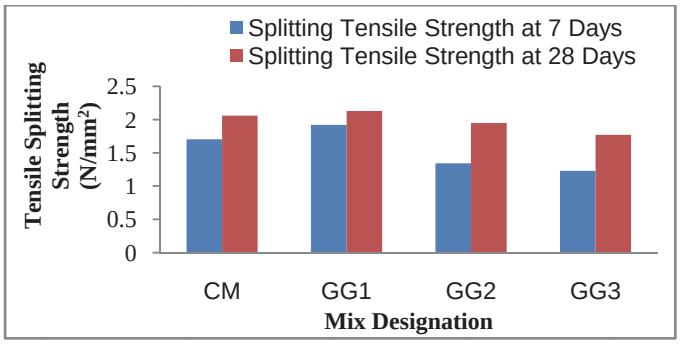

Fig.2 Effect of cement replacement percentages by GGBS on tensile splitting strength.

Table 8 Flexural Strength Test Results

Mix Type	Flexural Strength At 7 Days (N/mm^2)	Flexural Strength At 28 Days (N/mm^2)
CM	4.5	4.65
GG_1	4.55	4.83
GG_2	4.34	5.21
GG_3	3.96	5.35

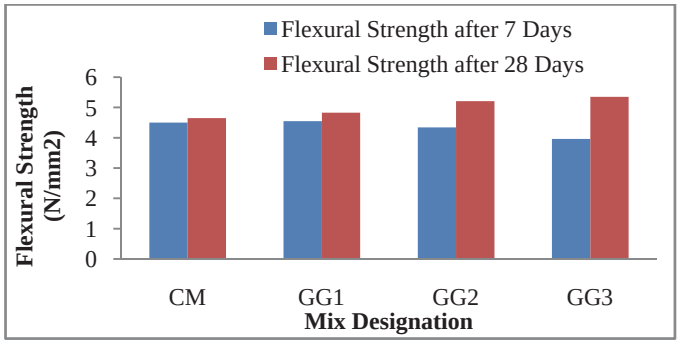

Fig.3 Effect of cement replacement percentages by GGBS on flexural strength

Table 9
Abrasion Test Results

Mix Type	Abrasion Value at 28 days (mm)
CM	1.36
GG_1	1.32
GG_2	1.41
GG_3	1.2

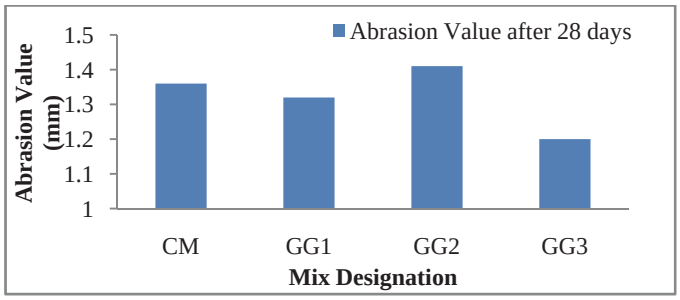

Fig.4 Effect of cement replacement percentages by GGBS on abrasion resistance

Table 10 Water Absorption Test Results

Mix Type	Water Absorption at 28 days (%)
CM	2.63
GG_1	2.87
GG_2	2.79
GG_3	2.67

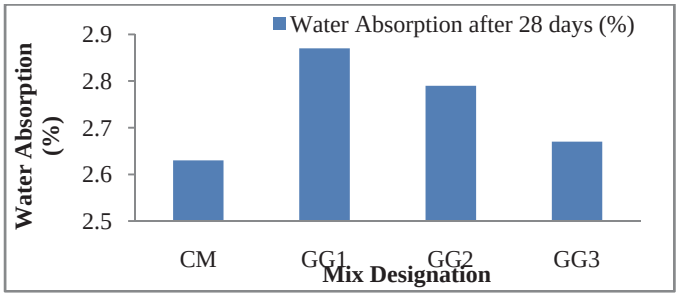

Fig.5 Effect of cement replacement percentages by GGBS on water absorption

VI. CONCLUSION

The following conclusions were drawn based on the above experimental results:

- Compressive strength requirement is met for all the specimens tested. As per IS: 15658:2006 the individual paver block strength shall not be less than 85 percent of the specified strength.
- Compressive strength and flexural strength are highest for the mix with 30% cement replacement by GGBS.
- The split tensile strength for the mix with 10% GGBS is higher than all other concrete mixes at both the testing ages.
- Increasing the GGBS content increases the flexural strength of the IPB at 28 days age. Flexural strength at 7 days decreased whereas at 28 days of curing the results at 30% cement replacement showed increase in strength. This shows slow early strength gain in GGBS concrete.
- The wearing depth was least for the specimen with 30% cement replacement in the abrasion resistance test.
- Water absorption of the specimens is slightly more than that of conventional mix but they are well within the permissible limits (<7% as per IS: 15658:2006).
- Hence the use of GGBS and quarry dust in concrete paver blocks is possible.

AKNOWLEDGEMENT

The authors are thankful to our beloved HOD Dr. Srinath Shetty K, Principle Dr. N Chiplunkar and faculty members of Department of Civil Engineering NMAMIT, Nitte for their continuous support to carry out this research work

REFERENCES

[1] R. Ilangovana, N. Mahendrana, K. Nagamanib, "Strength and Durability Properties of Concrete Containing Quarry Rock Dust as Fine Aggregate" ARPN Journal of Engineering and Applied Sciences, vol. 3, pp. 20-26, Oct. 2008.

[2] Hameed, M. S. And Sekar A. S. S., "Properties of green concrete containing quarry rock dust and marble sludge powder as fine aggregates", ARPN journal of Engineering and applied science, Vol.4(4), pp83-89, 2009.

[3] Chandana Sukesh, Katakam Bala Krishna, P. Lakshmi Sai Teja, S. Kanakambara Rao, "Partial Replacement of Sand with Quarry Dust in Concrete", IJITEE, Vol. 2, Issue-6, pp- 254-258, May 2013.

[4] G. Vijayakumar, H. Vishaliny, D. Govindarajulu, "Studies on Glass Powder as Partial Replacement of Cement in Concrete Production", IJETAE, vol. 3, pp. 153-157, Feb. 2013.

[5] Hanan A. El Nouhy, "Properties of paving units incorporating slag cement", HBRC, vol. 9, pp. 41-48, 2013.

[6] Euroslag Technical Leaflet, "Granulated Blastfurnace Slag", 2003.

[7] Bureau of Indian Standards 2386(part 3):1963, "Methods of Test for Aggregate for Concrete", New Delhi.

[8] IS: 1489-1991, Specifications for 53-Grade Portland Pozzolona cement, Bureau of Indian Standards, New Delhi, India.

[9] Bureau of Indian Standards 10262:2009, "Concrete Mix Proportioning", New Delhi.

[10] Bureau of Indian Standards 10262:1982, "Recommended Guidelines for Concrete Mix Design", New Delhi.

[11] IRC: SP: 63-2004 "Guidelines for Use of Interlocking Concrete Block Pavement" Indian Roads Congress.

[12] IS: 15658:2006 on "Precast Concrete Blocks for Paving – Specification," Bureau of Indian Standards.

[13] IS: 456: 2000 "Plain and Reinforced Concrete- Code of Practice," Bureau of Indian Standards.

Design of Piezoactuator Based Prototype Actuator with Hydraulic Displacement Amplification Using Metal Diaphragm

Mohith S[#1], Muralidhara[#2], Rathnamala Rao*[3]

[#] *Department of mechanical engineering,*

NMAMIT, Nitte, Karkala, Udupi, Karnataka - 574-110, Affiliated to VTU – Belgaum.

[1]mohith.sdattanagar@yahoo.com

[2]mr_kallya@yahoo.com

[*] *Professor, Department of Electronics and Communication,*

NMAMIT, Nitte, Karkala, Udupi, Karnataka - 574-110, Affiliated to VTU – Belgaum.

[3]malarathna@yahoo.com

***Abstract*—In recent years, there has been lot of advancement in the field of piezo-actuated systems which find extensive application in micro/nano positioning. The advantageous features of piezoactuators include high dynamic response, higher positioning accuracy, high stiffness, low wear and tear and compact design. The short range of motion and hysteresis between applied voltage and resulting displacement of piezoactuator has limited their application. In this work a novel piezo-actuator based prototype actuator with hydraulic displacement amplification mechanism based on area differential principle is proposed to overcome the problem of limited displacement range of piezoactuator. Piezo actuator is used as primary actuator which deflects the diaphragm in piezo hydraulic displacement amplifier (PHDA). Three types of diaphragms are considered for hydraulic displacement amplification system namely flat, corrugated and slotted diaphragms. Stiffness of each diaphragm is analysed using ANSYS analysis software. It is found from the analysis that the stiffness of corrugated diaphragm of 0.25mm thickness is equivalent to stiffness obtained by slotted diaphragm of thickness 2mm for same diaphragm material of spring steel.**

***Keywords*— Piezoactuator, PHDA (Piezo hydraulic displacement amplifier), APA 230L, Slotted diaphragm, Corrugated diaphragm,**

I. INTRODUCTION

Piezoelectric actuators are the type of actuators which make use of piezoelectric materials as the active materials. These actuators convert electrical signals into controlled physical displacement [1]. Piezoelectric actuators or piezoactuators are one of the most popular electro-mechanical devices. These actuators find extensive application in industrial devices requiring precision control. The precise control of movement achieved by piezoelectric actuators is used to finely adjust machining tool slide, lenses, mirrors, or other equipment to sub nanometre or to micrometer scale. The advantageous features of piezoactuators include high dynamic response, higher positioning accuracy, high stiffness, low wear and tear and compact design [2].

In spite of several advantageous features, the displacement range associated with piezoactuators is too small for any practical application. But the force generated and positioning accuracy of these actuators is sufficient enough to be used for micro and nano positioning applications. Present positioning application demand for macro positioning range with micro/nano positioning accuracy. Hence there is a need for suitable technique which can be incorporated to amplify the displacement of piezoactuator to make them suitable for macro/micro positioning applications.

In order to create larger displacement, there must be a mechanism which is capable of amplifying the actuator's movements. There are a number of mechanisms developed to amplify the displacement of piezoactuator. Flexural displacement amplification system, hydraulic displacement amplification system and mechanism based amplification system (e.g. inchworm actuators) are used to amplify the displacement of a stack actuator [3], [4]. Inchworm mechanism makes use of clamping and braking system used along with piezoactuator. These can produce stepped displacement with larger force [5]. The displacement limitations associated with piezoactuators can also be overcome by use of amplified piezoelectric actuators (APA) which makes use of flexural displacement amplification where piezo stacks are pre-stressed inside an elliptical frame [5]. These actuators can produce displacement amplification of 2 to 20 and have good mechanical efficiency. High displacement of APA is also combined with high force [6]. Hydraulic displacement-amplification mechanism can be effectively used for increasing displacement of piezoactuator. Piezo hydraulic displacement amplifier (PHDA) works on area differential principle. The output of piezoelectric

actuator will be amplified by difference in the cross sectional area of hydraulic chamber and the amplified displacement will be delivered to positioning mechanism [7, 8].

In the present work a piezoactuator based prototype actuator is developed with hydraulic displacement amplification mechanism using flat, corrugated and slotted diaphragm. The load deflection analysis of the corrugated and the slotted diaphragm is carried out and is compared with that of flat diaphragm.

II. PROPOSED DESIGN OF PIEZOACTUATOR BASED PROTOTYPE ACTUATOR WITH HYDRAULIC DISPLACEMENT AMPLIFICATION USING METAL DIAPHRAGM

In this work a prototype piezoactuator is developed with hydraulic displacement amplification mechanism as shown in Fig.1. The piezoactuator used is APA 230L which can produce maximum displacement of 230 μm. Characteristics of APA 230L are shown in Table I.

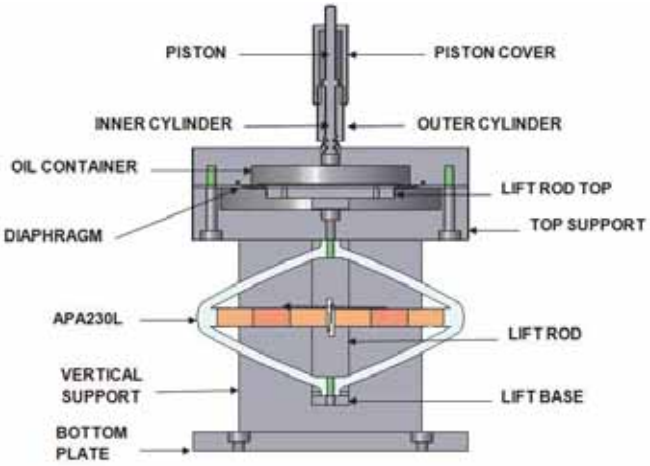

Fig. 1 Proposed design of piezoactuator based prototype actuator with hydraulic displacement amplification.

Table 1. CHARACTERISTICS OF THE APA230L PIEZOACTUATOR

References	**Unit**	**Value**
Displacement	μm	236
Voltage range	V	-20 to150
Stiffness	N/ μm	5.7
Resonance Frequency (Blocked Free)	Hz	850
Resonance Time(Blocked Free)	Ms	0.59
Force limit	N	700
Resolution	nm	2.4
Height(in actuation direction)	mm	85
Length and Width	mm	145.3 & 16

The amplification mechanism consist of two sections, one with larger cross sectional area i.e. oil container and other with smaller cross sectional area i.e. inner cylinder. One end of the reservoir is connected to a thin diaphragm which in turn is connected to lift rod. The displacement of the piezoactuator results in displacement of oil from the oil container to piston cylinder arrangement which moves the piston and hence results in amplification of displacement.

If V_1 is the volume of oil displaced from oil container and V_2 is the volume oil entering the inner cylinder, then

$$V_1=V_2 \quad (1)$$

$$A_1L_1=A_2 L_2 \quad (2)$$

Where A_1 is area of the center active region of the diaphragm assuming only center region of the diaphragm deflects and A_2 is the area of the inner cylinder, L_1 and L_2 displacement of piezoactuator and piston.

Thus the amplification factor can be obtained by the ratio

$$L_2/L_1=A_1/A_2 \quad (3)$$

Therefore the theoretical amplification factor is given by

$$L_2/L_1=D_1^2/D_2^2 \quad (4)$$

Where D_1 and D_2 are the effective diameters of diaphragm and inner cylinder diameter respectively

III. DESIGN OF SLOTTED DIAPHRAGM FOR PROTOTYPE ACTUATOR

Metallic diaphragms are thin circular discs which undergo elastic deformation when subjected to external pressure or axial load. The metallic diaphragms are widely used in the pressure measuring instruments. Thin metal diaphragms are also used in the pressure reducing valves (PRV). In PRV the pressure at downstream (outlet) side of the valve depends on the amount of deflection of metallic diaphragm [9].

In the present work, a slotted diaphragm is used to act as a barrier to oil container and transfer the deflection of piezoactuator through lift rod which causes the oil to displace from the oil container into the piston cylinder arrangement. The mechanical sensitivity of the slotted diaphragms can be improved by changing the geometric parameters of the diaphragms, such as depth of slot, thickness of diaphragm, width of slot and number of slots.

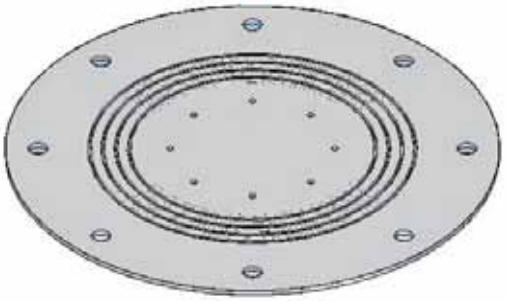

Fig. 2 Slotted diaphragm

TABLE 2. SPECIFICATIONS OF SLOTS USED IN SLOTTED DIAPHRAGM

Slot parameter	Value
Slot depth	1.45mm
Slot width	1mm
Gap between the Slots	1mm
No. of slots	8

The load-deflection behaviour of flat and slotted diaphragm is studied to access their suitability for PHDA. Fig. 2 shows the isometric view of the slotted diaphragm. Flat circular diaphragm is having outer diameter of 150 mm and center effective diameter of 70mm. The slotted diaphragm is also having same outer diameter of 150mm but the other parameters such as slot depth, slot width and number of slots are chosen according to the dimension shown in Table II. The thickness of both the diaphragms is maintained at 1.7mm. Material for both the diaphragm is spring steel. Table III shows the material property used for flat and slotted diaphragm. Fig. 3 (a) and 3 (b) show the dimensions of flat and slotted diaphragm used in the analysis.

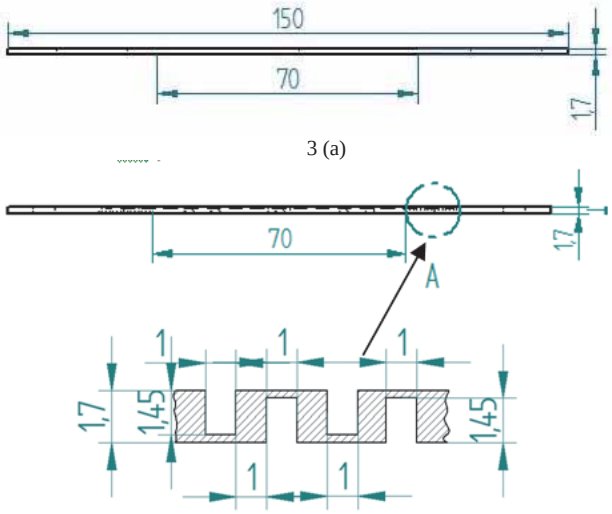

Fig. 3 Dimensions of (a) Flat Diaphragm (b) Slotted diaphragm used for load deflection analysis

TABLE 3. MATERIAL PROPERTY OF FLAT, SLOTTED AND CORRUGATED DIAPHRAGM

Material Property	Value
Young's modulus	203 GPa
Density	7830 kg/m^3
Poisson's ratio	0.305

The load-deflection analysis of diaphragms is carried out in ANSYS Simulation Software. The flat and slotted diaphragms are subjected to incremental pressure and deflection is analysed. The graph of force versus deflection is plotted as shown in Fig. 6. Deformation results obtained for flat and slotted diaphragm is shown in Fig. 7 and Fig.8.

IV. DESIGN OF CORRUGATED DIAPHRAGM FOR PROTOTYPE ACTUATOR

Corrugated diaphragms have improved sensitivity which can produce larger deflection when compared to flat diaphragms. The sensitivity of the corrugated diaphragm depends on its geometric parameters like depth of corrugation, thickness of diaphragm and number of corrugation. [9], [10].

Load deflection analysis is carried out for corrugated diaphragm which is compared with flat diaphragm similar to that the comparison between slotted and flat diaphragm. In the ANSYS simulation software the diaphragm is subjected to different pressure values and the deflection is analyzed. Fig. 4 shows the isometric view of the corrugated diaphragm.

The corrugated diaphragm acts as barrier which holds the oil above it in the PHDA. When input voltage is given to APA230L it produces deflection of the diaphragm causing oil to get displaced into the piston cylinder arrangement causing an amplified motion. The corrugated diaphragm used for load deflection analysis has an outer diameter of 150mm and centre effective diameter of 70mm. The dimensions of the corrugation are shown in Table IV.

TABLE IV
CORRUGATION PARAMETERS FOR CORRUGATED DIAPHRAGM

Corrugation parameter	Value
No. of corrugations	2
Thickness of corrugation	0.25mm
Inner radius of corrugation	3.25mm
Outer radius of corrugation	3.5mm
Corrugation pitch	13.75mm

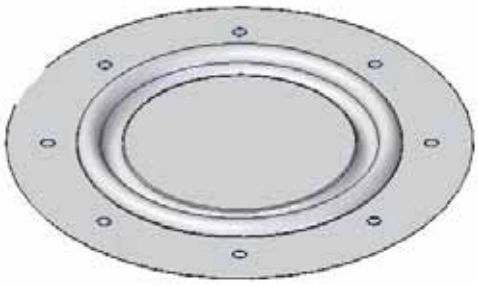

Fig. 4 Corrugated diaphragm

The deflection behavior of corrugated diaphragm is compared with that of flat diaphragm having same thickness. Material for both the flat and corrugated diaphragm is spring steel. Material property of flat and corrugated diaphragm is shown in Table III. Since the thickness of diaphragm is small a stiffener of thickness 4mm and diameter 50 mm is provided in the bottom part of the diaphragm over which the pressure is applied. Fig. 5 (a) and (b) shows the dimensions of flat and corrugated diaphragm used for analysis.

Deformation results obtained for flat and corrugated diaphragm are shown in Fig. 10 and Fig. 11.

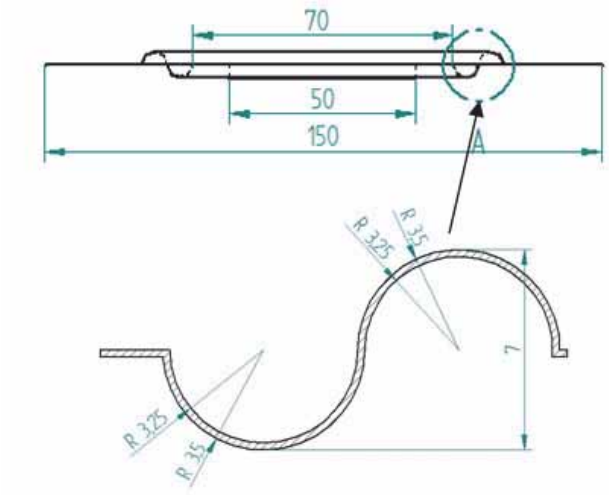

5 (a)

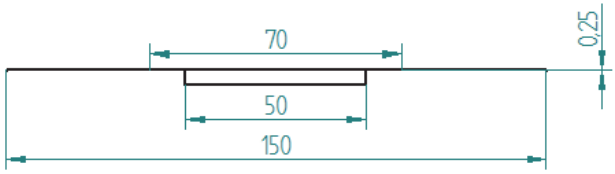

5(b)

Fig. 5 Dimensions of (a) Corrugated diaphragm (b) Flat diaphragm

V. RESULTS AND DISCUSSION

Force deflection relationship for flat and slotted diaphragm is shown in Fig. 6. From the graph it is observed that for a particular value of force, the deflection of the slotted diaphragm is more than that of the flat diaphragm. Stiffness of the diaphragm is also a major consideration when it is used along with the prototype actuator. From the Force versus Deflection plot it is found that stiffness of the slotted diaphragm is 1.59N/µm and that of the flat diaphragm is about 15.35 N/µm.

APA230L is designed to take up a maximum of 700 N. At maximum displacement of the APA i.e, 230 µm the load on the slotted diaphragm is about 365.7 N which is below the maximum load limit of APA. The remaining 334.3 N of force can be utilized for performing useful work at the out shaft of the prototype actuator. Considering the similar effect for flat diaphragm, in order to do useful work of 334.3N the deflection of flat diaphragm must be within 23.82µm. Due to this lower deflection, the volume of oil displaced from oil container reduces which proportionally reduces the amplified displacement. Hence, for same thickness, the slotted diaphragms will have lower stiffness and higher displacement amplification in the prototype actuator when compared to that flat diaphragm.

Fig.7 and Fig.8 shows the deflection produced in ANSYS simulation under same working pressure of 3MPa. The slotted diaphragm has maximum deflection of 7.2388mm and flat diaphragm has maximum deflection of 0.7518mm which is very less when compared with slotted diaphragm.

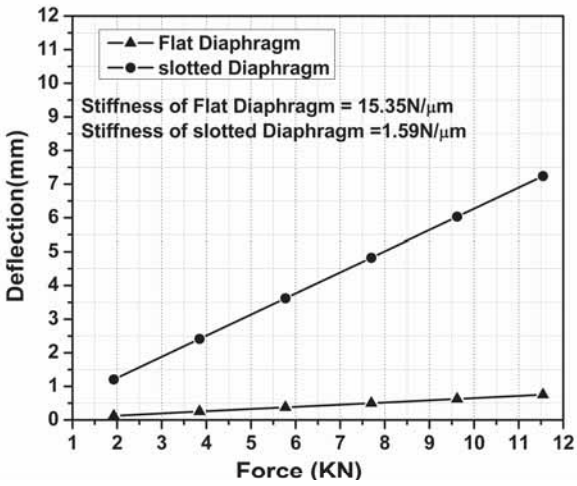

Fig. 6 Load Vs Deflection curve for slotted and flat diaphragm

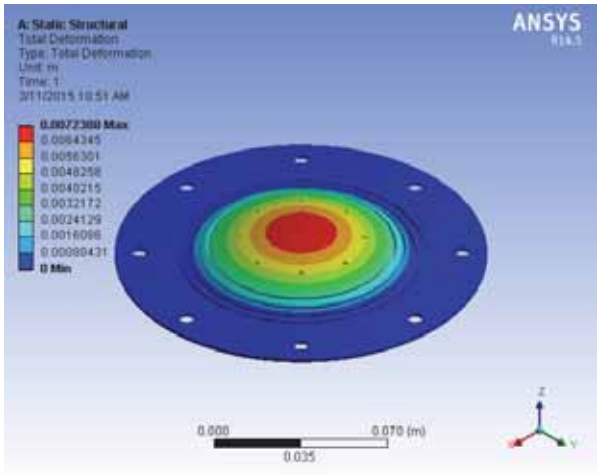

Fig. 7 Slotted diaphragm under a pressure of 3MPa.

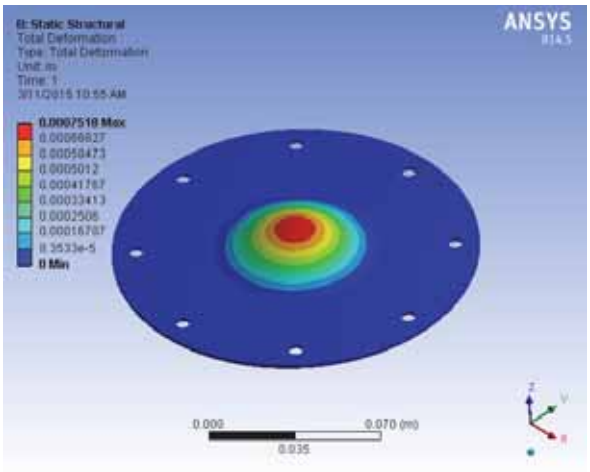

Fig. 8 Flat diaphragm under a pressure of 3 MP

The force deflection relation for corrugated and flat diaphragm is shown in Fig.9. From the force versus deflection curve it was observed that the deflection of corrugated diaphragm is more than the flat diaphragm of same thickness.

From the graph the stiffness of corrugated diaphragm is found to be 1.50N/µm which is smaller compared to that of flat diaphragm which is about 24.42N/µm. Since the thickness of diaphragm is very small a stiffener is used for both flat and corrugated diaphragm which contributes to the increased stiffness. However the corrugated diaphragms have smaller stiffness due to the presence of corrugation which is a major requirement when used with PHDA.

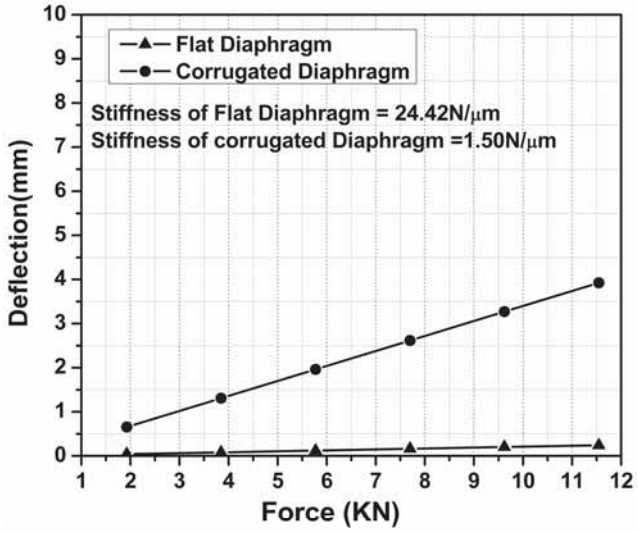

Fig. 9 Load Vs deflection curve for corrugated and flat diaphragm

At maximum displacement of the piezoactuator the load on corrugated diaphragm will be 345N which is below the load carrying capacity of APA. The remaining load of 355N can be used to do useful work. Considering the similar effect for flat diaphragm the deflection is limited to 14.12µm which effectively reduced the volume of oil displaced. Since the amplified displacement is directly proportional to volume of oil displaced, the amplified displacement decreases considerably. Thus for the same thickness and material the corrugated diaphragm has lower stiffness which produces larger amplified displacement in the prototype actuator when compared to that of flat diaphragm.

Fig.10 and Fig.11 show the deflection produced in ANSYS simulation under same working pressure of 3MPa. The corrugated diaphragm has maximum deflection of 3.9243mm and flat diaphragm has maximum deflection of 0.24114mm which is very less when compared with corrugated diaphragm.

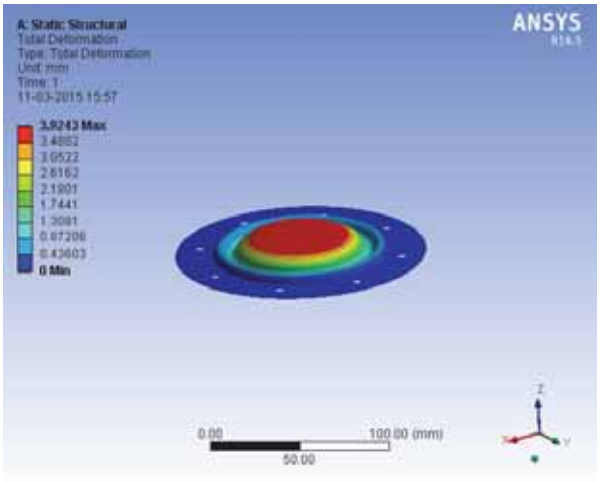

Fig. 10 Corrugated diaphragm under a pressure of 3MPa.

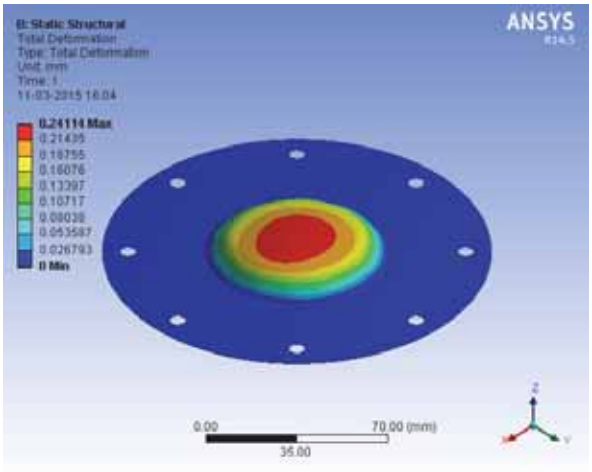

.

Fig 11 Flat diaphragm under a pressure of 3MPa

VI. Conclusion

In the present work a piezoactuator based prototype actuator with hydraulic displacement amplification mechanism is designed which works on area difference principle. Metal diaphragm is used as a barrier which holds the oil. Metal diaphragm undergoes deflection due to deflection of the piezoactuator. Three types of diaphragms are designed for PHDA namely flat, slotted and corrugated diaphragm. Load deflection analysis is carried out for both slotted and corrugated diaphragm and deflection behaviour is compared with that of the flat diaphragm. From the load deflection analysis it is found that the presence of slots and corrugation effectively increased the deflection when compared to flat diaphragms. The stiffness of slotted diaphragm is found to be 1.59 N/µm and that of corrugated diaphragm is 1.50 N/µm which is well suited for present application. The fabrication of corrugated diaphragms needs special type of dies for producing specific dimension of the corrugation. Hence cost of fabrication is high. Here in the present application slotted diaphragms is fabricated using

CNC machine. Therefore cost of fabrication of slotted diaphragm is less when compared to corrugated diaphragm.

ACKNOWLEDGEMENT

This research group would like to acknowledge the financial support extended by SERB, Department of Science and Technology, Government of India (Grant Ref. No. SR/FTP/ETA-0117/2011).

REFERENCES

[1] Pramathesh.T and Ankur.S "Piezoelectric Crystals: Future Source of Electricity" International Journal of Scientific Engineering and Technology, Volume 2 Issue 4, pp : 260-262, 1 April 2013

[2] https://www.americanpiezo.com/piezotheory/actuators.html#cat

[3] Muralidhara, Rithesh Baliga., Gokul R., Gregory Prashanth Dsouza, and Gireesh Madev moger, "Experimental Investigation on Piezoelectric based Prototype Actuator" in Trends in intelligent Robotics, Automation, and Manufacturing, Communications in Computer and Information Scinece volume 330,2012,pp 272-279, springer publication.

[4] Yung-Tien Liu,Bo-Jheng Li "Precision positioning device using the combined piezo-VCM actuator with frictional constraint" Journal of Precision Engineering 34 (2010) 534–545,Elsevier

[5] Jian Li, Ramin Sedaghati, Javad Dargahi ,David Waechter "Design and development of a new piezoelectric linear Inchworm actuator" Jounl of Mechatronics 15 (2005) 651–681, Elsevier

[6] Frank Claeyssen,R. Le Letty, F. Barillot, And O. Sosnicki "Amplied Piezoelectric Actuators: Static & Dynamic Applications" Ferroelectrics, 351:3—14, 2007 Taylor and Francis, 2007

[7] Hui Tang, Yangmin Li and Xiao Xiao "Development and Assessment of a Novel Hydraulic Displacement Amplifier for Piezo-Actuated Large Stroke Precision Positioning" 2013 IEEE International Conference on Robotics and Automation (ICRA) Karlsruhe, Germany, May 6-10, 2013

[8] T. Ninomiya, Y. Okayama, Y. Matsumoto, X. Arouette, K. Osawa, N. Miki "MEMS-based hydraulic displacement amplification mechanism with completely encapsulated liquid" Sensors and Actuators A 166 (2011) 277–282, Elsevier

[9] Gawade S. S., Chavan D. S. "Load-deflection analysis of flat & corrugated stainless steel diaphragms by theoretical & finite element method" International Journal of Engineering Research and Applications Vol. 3, Issue 4, Jul-Aug 2013, pp.799—802

[10] Mohammed Midhat Hasan "Theoretical Study and Simulation of Corrugated Silicon Diaphragm", The Iraqi Journal For Mechanical And Material Engineering, Special Issue (D)

Theoretical Investigation on Piezowafer Actuated Micropump

Astron Manoj Tauro [#1], Veeresha R.K[#2], Muralidhara[#3], Rathnamala Rao[*4]

[#] *Department of Mechanical Engineering,*
NMAMIT, Nitte, Karkala, Udupi, Karnataka - 574-110, Affiliated to VTU – Belgaum.
[1]astro.babba@gmail.com
[2]veereshark@nitte.edu.in
[3]mr_kallya@yahoo.com

[*] *Department of Electronics and Communication Engineering,*
NMAMIT, Nitte, Karkala, Udupi, Karnataka - 574-110, Affiliated to VTU – Belgaum.
[4]malarathna@yahoo.com

***Abstract*—Micropump is an integrated part of microfluidic system, is a boon to the field of miniaturization, owing its helping hand in numerous applications mainly in biomedical, electronic cooling, fuel cells, space craft etc. Actuation of micropump plays a prominent role in the working of micropump. In this paper an experimental and analytical method is employed to find out the pumping volume of piezowafer. This piezowafer is used as a actuation unit in micropump. The maximum displacement of 59.05µm was obtained for an applied input voltage of 150V. The actual volume that a piezowafer could pump considering hysteresis into account was found to be $1.344*10^{-8}m^3$ for an input voltage of 150V.Futher a coupled field analysis was carried out for piezowafer and the maximum displacement obtained was 64.7µm with estimated volume of $1.587*10^{-8}m^3$. Experimental and analysis results of estimated pumping volumes are in good agreement with each other.**

***Keywords*—Micropump, Piezowafer, Laser displacement sensor, ANSYS simulation**.

I. INTRODUCTION

Micropumps are now being a key component in various fields where miniaturization pumping plays a prominent role. Basically micropump is a miniature pumping device where a metered quantity of working fluid is transferred from reservoir to target. This device finds its importance in various domains because they provide efficient space exploration in an integrated system and also adding to the fact that these pumps can generate a flow rates in the range of millilitres to microliters per second or minute [1]. Some applications like drug delivery system [2] , microelectronic devices, micrototal analysis systems (μTAS) [3], portable DNA testing devices, electronic refrigeration systems and Fuel delivery in a fuel cell system [4] integrate micropump.

Micropumps are actuated by a physical actuator for the pumping. The actuation system may be mechanical type or non-mechanical type. Some mechanical types of actuations are electrostatic, thermopneumatic, piezoelectric, electromagnetic [5]. Non-mechanical actuations system includes electro-osmatic, electro-hydrodynamic, electrochemical, magneto-hydrodynamic [5]. Accounting for all actuations systems piezoelectric actuation is widely adopted because of its ease in controlling and cheaper in cost. In piezoelectric actuations, piezowafer is the driving unit or actuating source for the micropump to work and also the piezowafer decides the pumping volume that a micropump can pump when actuated at a particular voltage. Piezowafers are in form of disk or plate and are available in various sizes. They key is to actuate piezowafer at a particular voltage depending on amount of fluid is to be pumped where applications demands. The efficiency of micropump is decided by the pumping capability of the actuation system which indeed plays a major role in describing the micropump efficiency.

From literature only analytical analysis of circular PZT actuator is carried out [6], there no experimental work carried out on piezowafer for its parametric study whereas analysis of diaphragm is carried out which would be actuated by piezowafer , choosing different materials for diaphragm [7].

In this paper a 35mm piezowafer is experimentally tested for peak displacement when subjected to different voltages and maximum volume that a micropump can pump is obtained. Following to this a coupled field analysis is carried out to know the peak displacement of the piezowafer and the corresponding volume is calculated.

II. EXPERIMENTAL DETERMINATION OF PUMPING VOLUME USING PIEZOWAFER ACTUATION

A piezowafer of 35mm diameter was used to find experimental peak displacement and volume of the piezowafer when actuated for different input voltages. Piezowafer used in the experiment was mounted on a fixture to find the maximum displacement as shown in Fig.1.

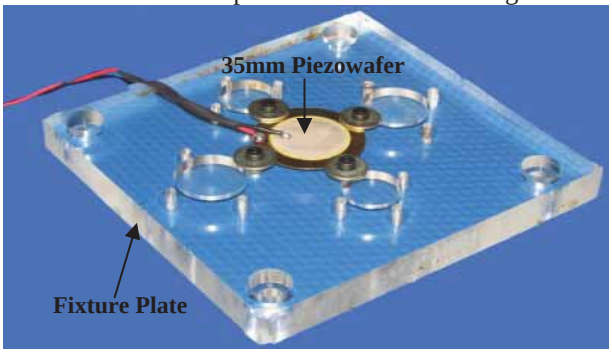

Fig.1 Fixture to find the displacement of 35mm diameter piezowafer

Experimental setup shown in Fig.2, consists of data acquisition card (National Instruments, NI PXIe-6363, consisting of 4 analog output and 32 analog input channels) was used in the setup. National Instruments LabVIEW software was used to generate an analog output signal and acquire the analog input signal. The generated amplified signal is fed to the piezowafer (35mm diameter) and corresponding displacement of the piezowafer is acquired using laser displacement sensor (ILD 2220-20, Measuring Range 20mm, 0.3µm Resolution, from Micro-Epsilon, Germany). The setup also consists of a motorized X stage (8MT175-50mm, Standa UAB, Lithuania) for movement of piezowafer in X direction.

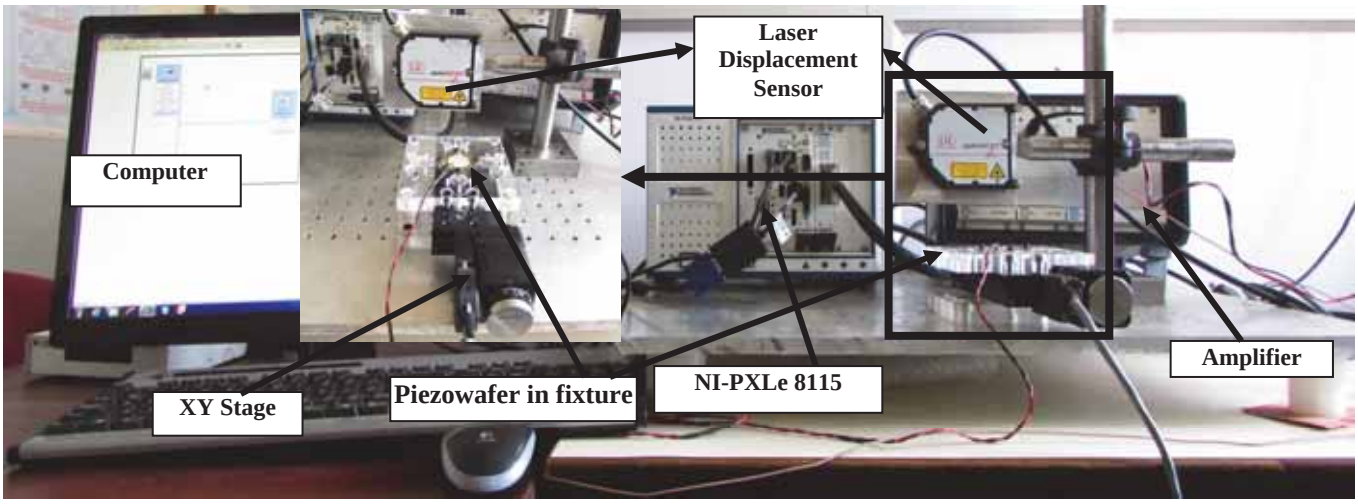

Fig.2 Experimental setup for testing of piezowafer

The piezowafer was excited for different input voltages from 0V to 150V with an increment of 25V. Meanwhile in order get the length of the conducting piezo-material patch, the piezowafer was moved in X direction so the displacements is traced from one end to the other end of the piezowafer and corresponding displacement of the piezowafer is acquired using laser displacement sensor as shown in Fig.2.

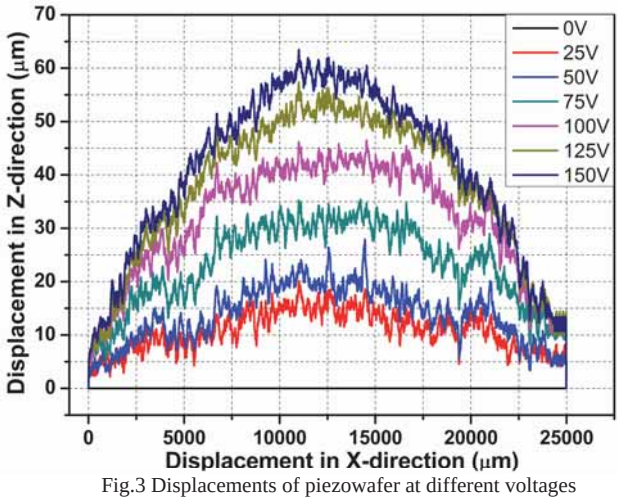

Fig.3 Displacements of piezowafer at different voltages

From the Fig.3 it was observed that peak displacement was at the centre of the piezowafer which is deformed as convex in shape. This plot was obtained by moving the piezowafer in X direction which enables to get deflection from the radius to centre of piezo-material patch. The deflection of the piezowafer can be assumed as partial sphere as shown in Fig.4. Hence volume of the partial sphere can be considered as volume that could be pumped by the piezowafer when integrated in a micropump.

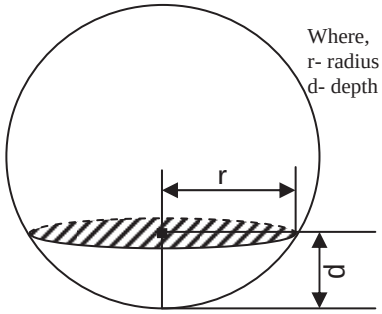

Where,
r- radius of the partial sphere
d- depth of the partial sphere

Fig.4 Detailed view of Partial sphere

..... (1)

The volume of the partial sphere can be given as

$$V = \frac{\pi}{6} d\left(3r^2 + d^2\right)$$

Above equation is used to calculate the pumping volume by considering peak displacement of piezowafer for an applied input voltage of 0-150V with an increment of 25V. The experimental peak displacement of the piezowafer and estimated volume reading have been plotted to obtain the

calibration curve for the 35mm diameter piezowafer as shown in Fig.5.

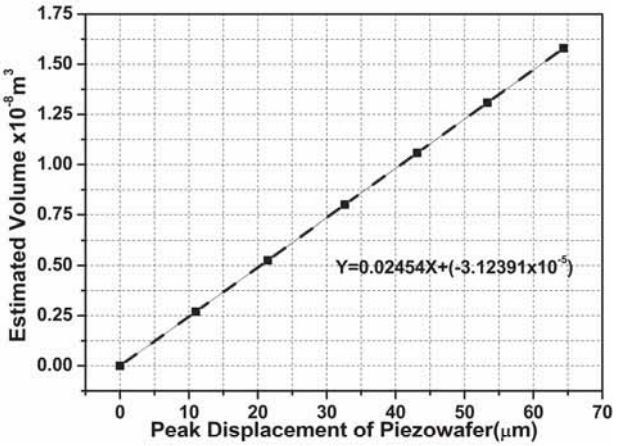

Fig.5 Experimental Evaluation of Volume by Displacement of Piezowafer

The relationship between the estimated volume and peak displacement of the piezowafer is found to be linear and is given by the equation.

$$y = 0.02454x + \left(-3.12391 \times 10^{-5}\right) \quad \text{.....(2)}$$

Where y= Estimated Volume (m^3)
x= Peak displacement of the piezowafer (μm)

It is evident from Fig.5 that estimated volume varies linearly with the peak displacement of piezowafer with slope of 0.02454.Therefore greater the displacement greater will be the volume pumping capability of the piezowafer. The above estimated volume also helps in selecting the applied voltage when the required outflow from the micropump is known for 35mm piezowafer which is shown in Fig 6.

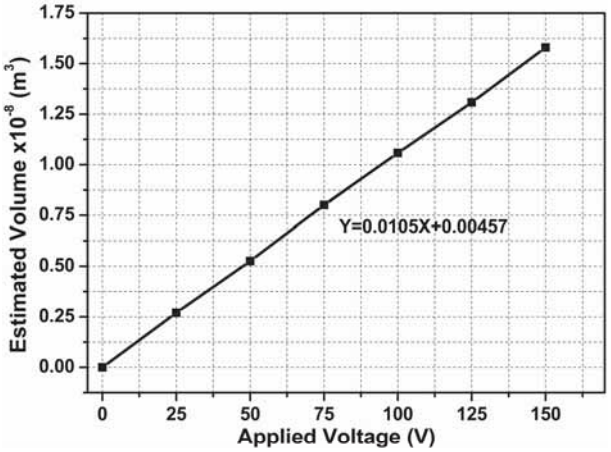

Fig.6 Experimental Evaluation of Volume by Applied Voltage of Piezowafer

The relationship between the applied voltage and estimated volume of the piezowafer is found to be linear and is given by the equation.

$$y = 0.0105x + 0.00457 \quad \text{.....(3)}$$

Where y= Estimated Volume (m^3)
x= Voltage applied on the piezowafer (μm)

Thus from Fig 5 and Fig 6 it is clear that as applied voltage increases the pumping volume also increases. The estimated volume of $1.58*10^{-8}$ m^3 is observed for an applied voltage of 150V.

The 35mm diameter piezowafer was subjected to input voltage of 150V at 0.2Hz frequency the maximum displacement of piezowafer was observed to be 59.05μm for an input voltage of 150V with a hysteresis of 4.31μm.

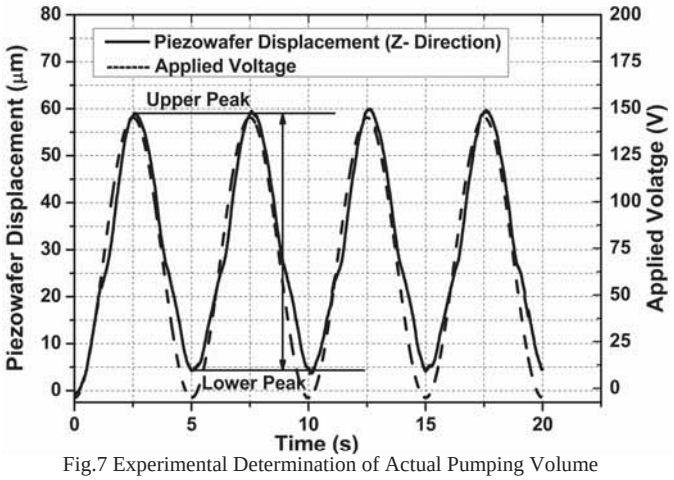

Fig.7 Experimental Determination of Actual Pumping Volume

Figure 7 shows the piezowafer displacement at 0.2Hz frequency, in order to calculate the actual pumping volume due to the actuation of piezowafer the upper peak displacement and lower peak displacement is noted. The lower peak point should have been 'zero' but there is an remnant displacement of 4.31μm, considering this effect of hysteresis the lower point is as chosen as 4.31μm shown in Fig.7, thus corresponding volume is calculated by using the equation 1, the difference of volume corresponding to these two peak points gives the actual pumping volume of micropump with actuation by piezowafer of 35mm diameter at 150V.

Volume estimated at upper peak point which is 59.05μm

$$V = \frac{\pi}{6} d\left(3r^2 + d^2\right)$$

$$V = \frac{\pi}{6}\left(59.05 * 10^{-6}\right) * \left[3 * \left(12500 * 10^{-6}\right)^2 + \left(59.05 * 10^{-6}\right)^2\right]$$

$$V = 1.449 * 10^{-8} m^3 \quad \text{.....(4)}$$

Volume estimated at lower peak point which is 4.31μm

$$V = \frac{\pi}{6} d\left(3r^2 + d^2\right)$$

$$V = \frac{\pi}{6}\left(4.31*10^{-6}\right)*\left[3*\left(12500*10^{-6}\right)^2 + \left(4.31*10^{-6}\right)^2\right]$$

$$V = 0.105*10^{-8}\, m^3 \quad \text{.....(5)}$$

The actual volume pumped is calculated as

$$Volume_{Total} = Volume_{Upperpeak} - Volume_{Lowerpeak}$$

$$Volume_{Total} = 1.449*10^{-8} - 0.105*10^{-8}$$

$$Volume_{Total} = 1.344*10^{-8}\, m^3 \quad \text{.....(6)}$$

Equation 6 is the actual volume pumped by an micropump which is integrated with piezowafer of 35mm diameter actuated at an voltage of 150V and frequency of 0.2Hz.

III. ANALYSIS OF PIEZOWAFER

The coupled field analysis was performed over 35mm diameter piezowafer in ANSYS 14.5 to find the maximum displacement of the piezowafer with an input voltage of 0-150V with 25V as increment. In this analysis 20 noded solid 226 elements was chosen for piezo material patch and 20 noded solid 186 elements for the brass plate over which the piezo material is deposited.

TABLE 1. SHOWS THE PROPERTIES USED FOR THE ANALYSIS.

Component	Material Properties	Value
Brass Plate (20 node solid 186)	Young's Modulus	102GPa
	Poisson's Ratio	0.3
	Density	8400 kg/m^3
Piezowafer (20 node solid 226)	Stiffness matrix at constant E field	$\begin{pmatrix} 12.6 & 7.95 & 8.4 & 0 & 0 & 0 \\ 7.95 & 12.6 & 8.4 & 0 & 0 & 0 \\ 8.41 & 8.41 & 11.7 & 0 & 0 & 0 \\ 0 & 0 & 0 & 2.3 & 0 & 0 \\ 0 & 0 & 0 & 0 & 2.3 & 0 \\ 0 & 0 & 0 & 0 & 0 & 2.32 \end{pmatrix} 10^{10}$ N/m^2
	Relative Permittivity	$\begin{pmatrix} 1700 & 0 & 0 \\ 0 & 1700 & 0 \\ 0 & 0 & 1470 \end{pmatrix}$
	Piezoelectric matrix [e]	$\begin{pmatrix} 0 & 0 & -6.5 \\ 0 & 0 & -6.5 \\ 0 & 0 & 23.3 \\ 0 & 17 & 0 \\ 17 & 0 & 0 \\ 0 & 0 & 0 \end{pmatrix}$ C/m²
	Density	7500 kg/m^3

The above properties are used to find the maximum displacement of piezowafer for an applied voltage of 150V using ANSYS and corresponding displacement shown in Fig 8(a) & Fig 8(b).

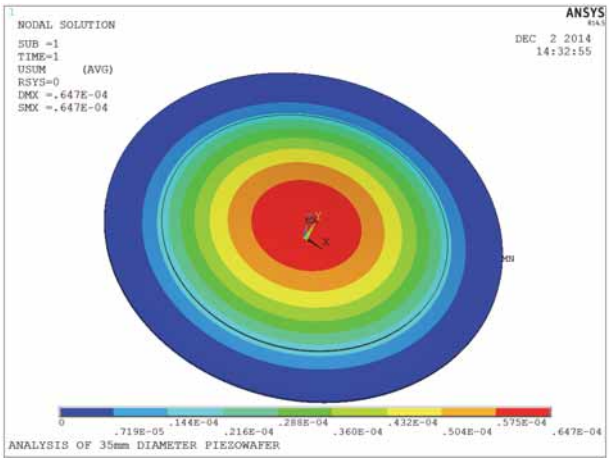

Fig.8(a) Displacement of Piezowafer at 150V

From the analysis Fig.8(a) the peak displacement of piezowafer at an input voltage of 150V was found to be 64.7 µm. The deflection gradually increases from the outer radius of piezo-material to centre where the deflection is maximum shown in Fig 8(b). This deflection at centre obtained from the analysis is same as seen in Fig.3 which was obtained experimentally. The coupled field analysis was extended to different voltages of the piezowafer and the peak displacements were noted.

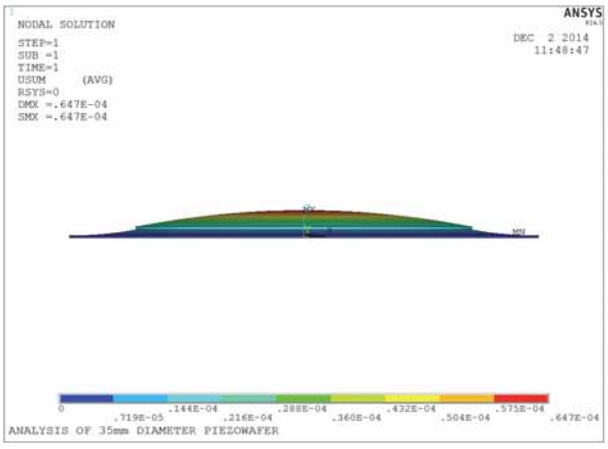

Fig.8(b) Front view of Displacement of Piezowafer at 150V

The peak displacements at different voltages from 0-150V with 25V as increment were used to estimate the volume pumped by the piezowafer using equation 1. Estimated volume was plotted against peak displacement of piezowafer as well as with applied voltage which is shown in Fig 9. At a voltage of 150V the volume estimated was found to be $1.587*10^{-8}$m^3 with peak displacement of 64.7 µm. It is evident

from the plot that volume varies increasingly linear to peak displacement of piezowafer and applied voltage.

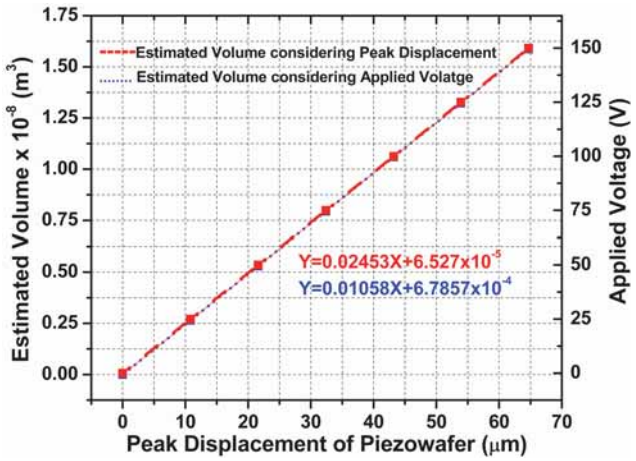

Fig.9 Estimation of volume using theoretical value (ANSYS)

The relationship between the estimated volume and peak displacement of the piezowafer is found to be linear and is given by the equation.

$$y = 0.02453x + 6.527 \times 10^{-5} \quad \text{.....(7)}$$

Where y= Estimated Volume (m^3)

x= Peak displacement of the piezowafer (μm)

The relationship between the applied voltage and estimated voltage of the piezowafer is found to be linear and is given by the equation.

$$y = 0.01058x + 6.7857 \times 10^{-4} \quad \text{.....(8)}$$

Where y= Estimated Volume (m^3)

x= Applied voltage on the piezowafer (μm)

IV. CONCLUSION

In this paper theoretical and experimentation was carried out to find the estimated volume of the 35mm piezowafer used as an actuator in micropumps for pumping fluids. The experimentation and analysis of piezowafer at different voltages has shown an increasing trend with respect to estimated volume. Hence for the high outflow of the micropump maximum allowable voltage should be chosen .

At 150V the experimentally obtained displacement was 59.05μm and considering the volume loss because of hysteresis the actual volume that could be pumped by piezowafer was found to be $1.344*10^{-8}m^3$. Meanwhile the analysis of piezowafer was carried out in ANSYS which owed a maximum displacement of 64.7μm with estimated volume as $1.587*10^{-8}m^3$.

On comparing experimental and analysis result for estimated volume it is found that a maximum error of 15% is obtained , this is because the ANSYS simulation does not consider hysteresis behaviour into account during the simulation. Therefore the experimental and analysis results of estimated volumes are in good agreement.

ACKNOWLEDGEMENT

The research group would like to acknowledge the financial support extended by **Vision Group on Science and Technology** (VGST), Department of Information Technology, Biotechnology and Science and Technology , Government of Karnataka (**Grant Ref. No. VGST/TRIP/127/2014-15**).

REFERENCE

[1]. Farideh Abhari, Haslina Jaafar, Nurul Amzaih, and Md Yunus," *A Comprehensive study of micropump technologies* " , International Journal of Electrochemical Science,7: 9765-9780, 2012 .

[2]. D. Maillefer., S. Gamper., B. Frehner., P. Balmer., H. Van Lintel., and P. Renaud, "*A high-performance silicon micropump for disposable drug delivery systems*", in: The 14th IEEE International Conference on MEMS, 2001.

[3]. A. Manz, N. Graber, H.M. Widmer, "*Miniaturized total chemical analysis systems: a novel concept for chemical sensing*", Sensors and Actuators B1, pp 244–248,1990.

[4]. T. Zhang., Q. Wang.," *Valveless piezoelectric micropump for fuel delivery in direct methanol fuel cell (DMFC) devices*", Journal of Power Sources ,vol 140, pp. 72–80, 2005.

[5]. Nam-Trung Nguyen, Xiaoyang Huang, TohKok Chua, "*MEMS-Micropumps: A Review*", Journal of Fluids Engineering, vol 124, pp. 1-9 , 2002.

[6]. Shifeng Li, Shaochen Chen, *"Analytical analysis of a circular PZT actuator for valveless micropumps"* Sensors and Actuators A , vol 104 , pp.151–161,2003.

[7]. Y. H. Mu, N. P. Hung and K. A. Ngoi, "*Optimisation Design of a Piezoelectric Micropump*", International Journal of Advanced Manufacturing Technology, vol 15, pp.573–576, 1999.

[8]. Jiashi Yang, "*Analysis of Piezoelectric Devices* ", World Scientific Publishing Co. Pte. Ltd., pp: 503-506, 2006.

[9]. Autar K. Kaw, "*Mechanics of Composite Materials - Ed 2* ", Taylor & Francis Group, LLC, New York , pp : 79-87, 2006.

Perturb and Observe for Maximum Power Point Tracking

Raghavendra Rao P[1], Prof. K.Vasudeva Shettigar[2]
[1]*M.Tech, 4th Semester (Microelectronics and Control Systems),* [2]*Associate Professor*
Department of Electrical and Electronics Engineering
NMAM Institute of Technology, Nitte, Udupi-574110
[1]praghavendrarao@ymail.com
[2]kvshettigar@nitte.edu.in

***Abstract*- Among renewable sources available, solar energy is one of the abundant sources of energy which is widely available throughout the globe. Solar electricity or photovoltaic (PV) technology converts sunlight directly into electricity. This project describes how to extract the Maximum power from the PV panel by making them to operate at the most efficient voltage. Improving the maximum power point with new control algorithms is less expensive and can be implemented very easily. Boost converter is used as an interface between PV panel and load. In this paper Perturb and Observe control algorithm is used to track the Maximum power point and hence generate PWM signals for MOSFET. This is implemented on PIC16F877A microcontroller from Microchip. Matlab software is used to simulate PV panel, Boost converter and Maximum power point tracking algorithm.**

***Keywords*- Maximum Power Point Tracking (MPPT), Pulse Width Modulation (PWM), Perturb and Observe (P&O), Photo-Voltaic (PV).**

I. INTRODUCTION

We primarily use fossil fuels and also use non-renewable energy sources like coal, oil, water and natural gas for meeting our energy demand, but we have a limited supply of the above fuels on the Earth. We use them much more rapidly than they are being created. Eventually, they get depleted in early years. Renewable energy sources are continually replenished by nature. Among all the renewable sources of energy, solar energy is one of the most abundant and widely available sources, which is available throughout the globe. Solar electricity or photovoltaic (PV) technology converts sunlight directly into electricity. Solar electricity has been a prime source of power. Photovoltaic (PV) power generation has an important role to play due to the fact that it is a clean energy source. PV modules are made of silicon cells. These modules are connected in series and parallel to obtain higher power output forming PV array.

The major principle of MPPT ([3]-[5], [7]-[11]) is to extract the maximum available power from PV module by making them operate at the most efficient voltage (maximum power point). Improving the maximum power point tracking with new control algorithms is easier, less expensive and can be implemented very easily in the existing plant that has been incorporating other algorithms for maximum power point tracking. There are different types of DC-DC converters that can be used as an interface between PV panel and the load depending on the applications. In this paper, Boost converter is used as an interface between panel and load. The input to the converter is fed from the output of the PV panel and is controlled to regulate the operating point of the array. The project aims at implementation of control algorithm for a PV system so as to extract maximum power and also to charge a battery of 24V, 7.2Ah Lead-Acid rechargeable battery.

II. OVERVIEW

The overall system consists of PV panel, Boost converter, MPPT control block and a 24V, 7.2Ah Battery that acts as a load. This can be shown as in Fig. 1.

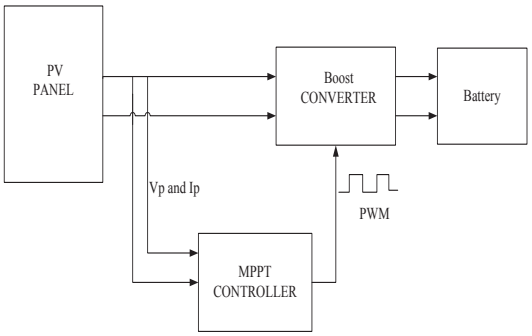

Fig. 1 Block Diagram

A. PV Panel

A solar panel is a set of photovoltaic modules electrically connected and mounted on a supporting structure. A PV module is a packaged, connected assembly of solar cells. Number of PV modules can be connected in series or parallel to increase the current and voltage rating of PV panel.

B. Boost Converter

When the Switch 'S' is closed, Vs =V_L and diode is reverse biased. When the Switch is open, the voltage across the output will be the sum of input voltage (V_s) and inductor voltage (V_L). Hence the output voltage is always greater or equal to input voltage [6]. In this IRFZ44 MOSFET is used as a switch with the maximum drain current of 50A.This is driven by driver IC, TLP250.

Fig. 2 shows the block diagram of Boost converter.

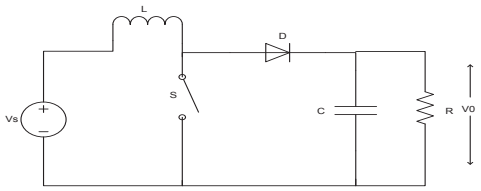

Fig. 2 Boost Converter

C. MPPT Controller

A non MPPT controller connects PV panel to load or battery. In this paper, a 20W PV panel is used whose maximum Voltage is 17.64V. This cannot charge a battery of 24V. Hence Boost converter is used as an interface for this purpose that boosts the voltage and lowers the current and balances the input and output power. The switching of the converter is done by using controller for which suitable algorithm is applied so that closed loop control of the panel can be provided.

To understand the working of non MPPT controller more precisely, consider an example of the panel whose rating is 20W and is used to charge a battery of 6V. The battery will pull down the module operating voltage to 6V at 1.18A which is the maximum current of the panel. So we are using only 7.08W out of 20W when a panel is able to supply. Hence MPPT process is used wherein a converter is used as an interface to lower the voltage and increase the current so that the input power and output power is same. If a MPPT controller i.e. buck converter is used as interface in this case, then this DC-DC converter lowers the voltage to battery voltage thus raising the current up to 3.33A giving effective power of around 20W which is the maximum power that a panel is able to supply. The converter is designed properly for the specific power rating.

MPPT controller is used to produce PWM signals to drive the gate of MOSFET. P&O control algorithm is applied generate PWM signals. The controller used here is PIC16F877A. The Schematic of PIC16F877A is as show in Fig. 3.

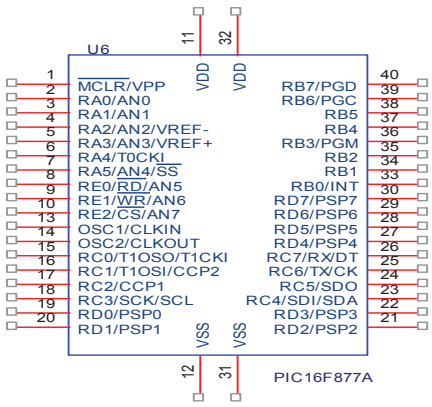

Fig. 3 PIC16F877A

Some of its features include

a) Operating speed: DC - 20 MHz clock input
b) Up to 8K x 14 words of FLASH Program Memory
c) Up to 368 x 8 bytes of Data Memory (RAM)
d) Wide operating voltage range: 2.0V to 5.5V
e) High Sink/Source Current: 25 mA
f) Interrupt capability (up to 14 sources)
g) Watchdog Timer (WDT) with its own on-chip RC oscillator for reliable operation
h) Power-on Reset (POR)
i) Low-power consumption
j) Two Capture, Compare, PWM modules. PWM maximum resolution is 10-bit
k) 10-bit multi-channel Analog-to-Digital converter.

The flowchart of P&O algorithm [1] is as shown in Fig. 4. In this, the panel voltage and current is tracked continuously. Voltage divider is used as a voltage sensor to track voltage. Panel current is sensed by IC WCS2720. This has been used since the internal conductor resistance is 0.4Ω, which accounts for very low power dissipation.

Initially the voltage and current at $(k-1)^{th}$ stage is taken as zero. The k^{th} stage voltage and current is tracked using voltage and current sensors. The power of both k and (k-1) stages are calculated. If the present power is greater than the previous, it means that the operating point of the panel is increasing either from the left side or right side of P-V curve as shown in Fig. 5. Hence to determine the position of the operating point, the panel voltage of k and (k-1) stage has to be compared. If the present i.e. voltage at 'k' stage is greater than (k-1) stage, then operating point is at the left side of the P-V curve. Hence duty cycle has to be decreased in order to increase the panel tracking voltage; else the duty cycle has to be increased in order to decrease panel voltage so that tracking power is increased.

Similarly if the present power is less than previous power, the operating point is decreasing either in the right side or decreasing in the left side of the P-V curve. So in order to determine the operating point the voltages are compared. If the present voltage is greater than the previous voltage, then the operating point is at the right side of the P-V curve and duty cycle has to be increased in order to decrease the panel voltage so that it reaches its maximum point (V_m). If voltage is lesser than previous voltage then the operating point is at the right side and the duty cycle has to be decreased in order to increase the panel tracking voltage.

The 'V_{ref}' value determines the incremental steps to be taken that decide how fast the algorithm can track the maximum power. If 'V_{ref}' is taken very high value then there is a possibility that while increasing or decreasing the duty cycle, the operating point may not get fixed to a point wherein maximum power is obtained i.e. the operating point may get fixed either on the right side or left side of the curve. If 'V_{ref}' value is taken very less exact maximum power is tracked, but the tracking time will be more. In my paper, 'V_{ref}' value taken is 0.01 i.e. 1%.

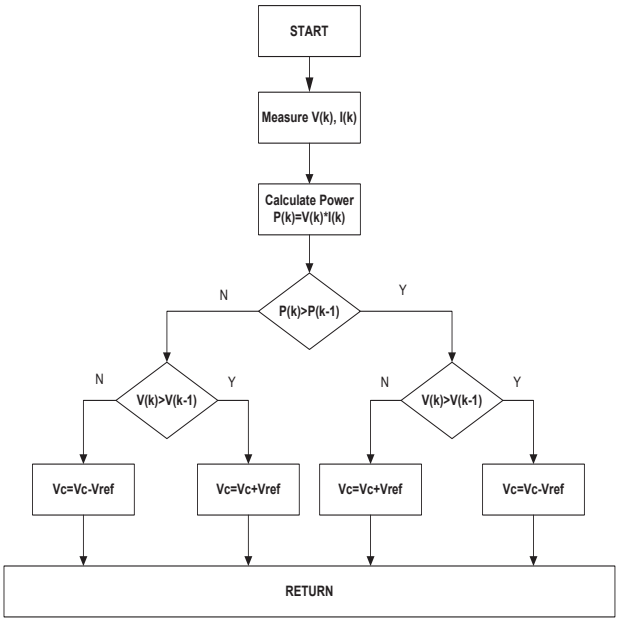

Fig. 4 P&O Flowchart

III. SIMULATION RESULTS

A 20W PV module is chosen to charge a battery of 24V, 7.2Ah battery that acts as a load. Specification of 20W panel is given in TABLE I.

TABLE I
20W SPECIFICATIONS

Parameters	Value
Maximum Power (P_m)	20W
Maximum Voltage (V_m)	17.64V
Maximum Current (I_m)	1.18A
Open Circuit Voltage (V_{oc})	21.64V
Short Circuit Current (I_{sc})	1.23A

Power output from the PV panel changes with the change in radiation, temperature and orientation of the panel. Fig. 5 and Fig. 6 shows the typical P-V and I-V curves at different radiation levels.

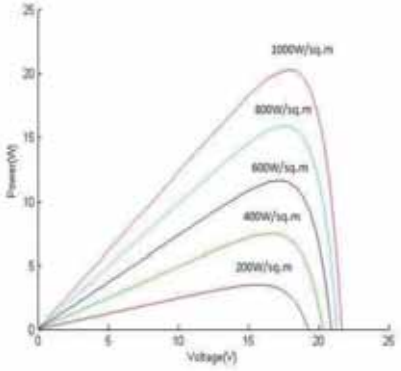

Fig. 5 Power versus Voltage curves at different radiation levels

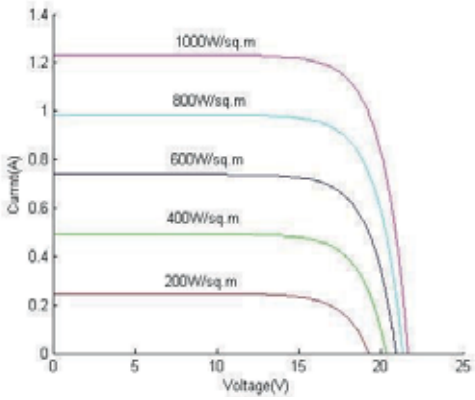

Fig. 6 Current versus Voltage curves at different radiation levels

There exists only one maximum power at each radiation level. It is desired to operate the panel at its peak power. When the panel is directly connected to the load, it operates at load voltage than the voltage at its peak power point. Hence this project makes use of Boost converter as an interface between panel and load. By changing the duty cycle, the impedance of the load as seen by the source can be varied and matched so that maximum power is transferred to the load.

A. PV Panel Modeling

Single solar cell can be represented by an equivalent circuit as shown in Fig. 7.

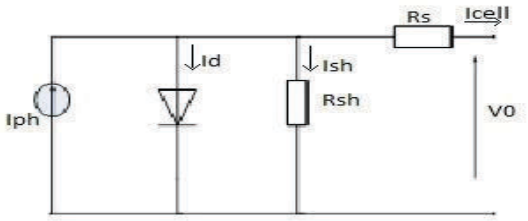

Fig. 7 Solar cell

The symbols in Fig. 7 are defined as follows.
I_{ph}: photocurrent
I_d: current at parallel diode
I_{sh}: shunt current
I_{cell} (I_c): output current
V_0: output voltage
R_{sh}: Parallel Resistance
R_s: Series Resistance
The equations as in [2] are used to model the PV panel.

$$I_c = I_{ph} - I_0 \left[\exp\left(\frac{q(V+RsI)}{AKT}\right) - 1\right] - \left(\frac{V+RsI}{Rsh}\right) \ldots\ldots\ldots (1)$$

The term $(V+R_sI)/R_{sh}$ can be ignored, because it is far less than I_{sh}. Equation (1) can be written as

$$I = I_{sc}\left(1 - C_1\left(\exp\left(\frac{V}{C2Voc}\right) - 1\right) \ldots\ldots\ldots\ldots\ldots (2)$$

Where I: output current of PV panel
C_1, C_2: undetermined coefficients
Under maximum power output condition, equation (2) can be written as

$$I_m = I_{sc}\,(1\text{-}C_1\,(\exp\,(\frac{Vm}{C2Voc})\,\text{-}1))\ldots\ldots\ldots\ldots\ldots\ldots\ (3)$$

Where

$$C_1 = (1\text{-}\frac{Im}{Isc})\,\exp\,(\frac{-Vm}{C2Voc})\ldots\ldots\ldots\ldots\ldots\ldots\ (4)$$

$$C_2 = ((\frac{Vm}{V0c})\text{-}1)/\,\ln(1-(\frac{Im}{Isc}))\ldots\ldots\ldots\ldots\ldots\ (5)$$

Considering the changes of temperature and radiation [2], the output current is given by equations below.

$$\Delta T = T\text{-}T_{ref}\ldots\ldots\ldots\ldots\ldots\ldots\ldots\ldots\ldots\ (6)$$

$$\Delta I = \alpha\frac{S}{Sref}\,\Delta T + (\frac{S}{Sref}\text{-}1)\,Isc\ldots\ldots\ldots\ldots\ldots\ (7)$$

$$I^1 = I + \Delta I\ldots\ldots\ldots\ldots\ldots\ldots\ldots\ldots\ldots\ (8)$$

Where
T, $T_{ref:}$ Current temperature and reference temperature.
S, S_{ref}: Solar insolation and Current solar insolation.
α, β:Temperature coefficients of current and voltage.
The equations mentioned are used to model the PV panel. The Simulink model of the Solar panel is as shown in Fig. 8.

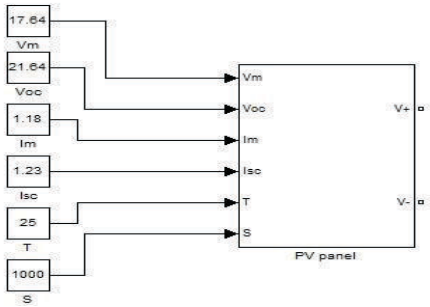

Fig.8 Simulink Model of PV panel

B. Boost Converter Modeling

The Simulink model of Boost converter is as shown in Fig. 9 with following specifications

TABLE II
SPECIFICATIONS OF BOOST CONVERTER

Parameter	**Value**
Inductor	650µH
Filter Capacitor	100µF
Frequency of Switching	25KHz

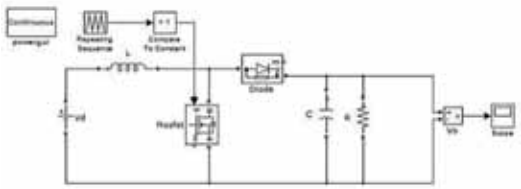

Fig. 9 Boost Converter

C. Modeling entire System

Fig. 10 shows the Simulink model of the entire system

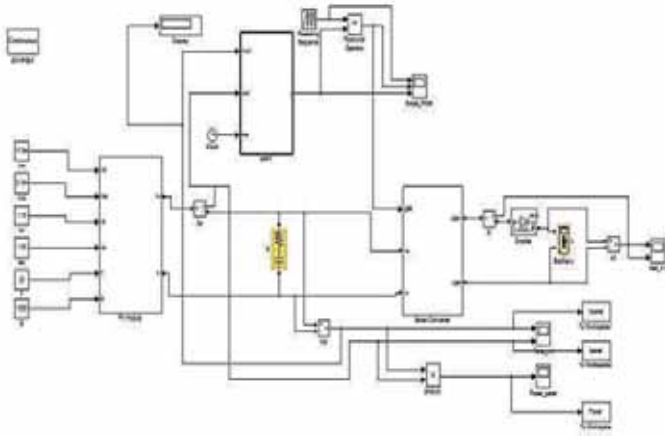

Fig. 10 Simulink model of the entire system

Fig. 10 shows the system depicting PV panel, Boost converter, MPPT block and Battery as load. The panel power can be seen in Fig. 11 when P&O algorithm is applied.

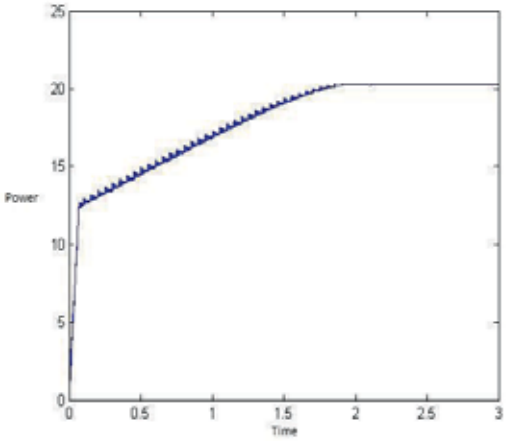

Fig. 11 Panel Power when MPPT applied

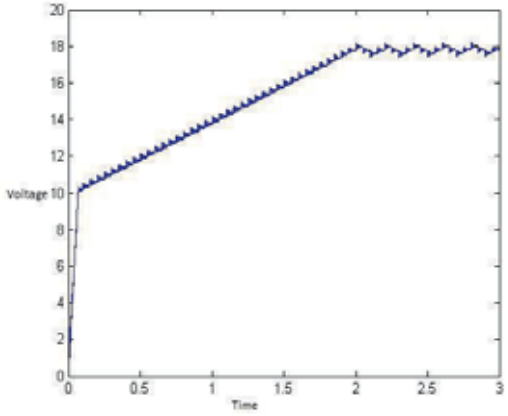

Fig. 12 Panel Voltage at MPP

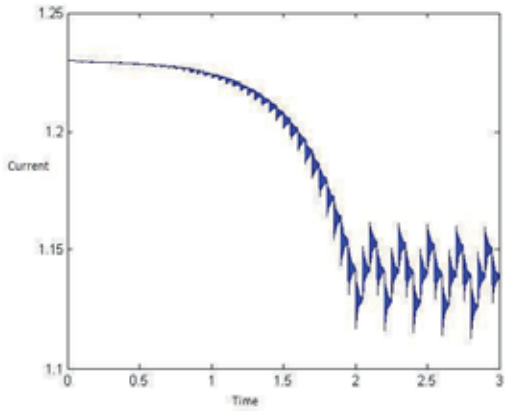

Fig. 13 Panel current at MPP

From Fig. 11, Fig. 12 and Fig. 13 we can see that maximum power is obtained at simulation time 2s and it oscillates at its peak power of 20W. Peak power is obtained at a voltage of 17.7V and current at 1.16A.

IV. HARDWARE RESULTS

Fig. 14 shows the plot in Matlab obtained when perturb and Observe algorithm is applied to the controller and load as Rheostat of 100Ω. In this we can see that without MPPT, maximum power is obtained at 11.01W at a particular load, radiation and Temperature.

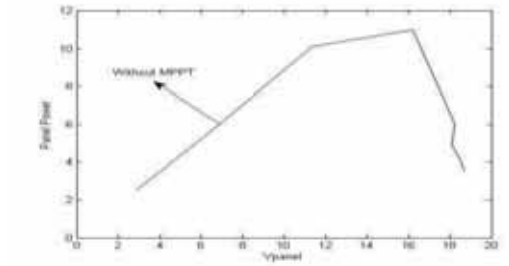

Fig. 14 P-V plot without MPPT

Fig. 15 shows the hardware setup of the complete system and the result when P & O is applied to the controller thus charging a battery of 24V, 7.2Ah Lead-Acid rechargeable Battery.

Fig. 15 Hardware setup of the system

From the hardware setup we can see that the panel voltage is fixed at 9.23V with panel current 1.19 A with an effective power of 10.98W at that temperature and radiation. Thus without MPPT we can see that there is only single maxima power at a particular load and then it decreases as compared to MPPT where the Maximum power is tracked and oscillates at peak point.

V. CONCLUSION

It can be concluded that the proposed P&O method is very easy to simulate and implement on a controller or processor. It can be seen that maximum power is tracked through this algorithm. But there is a compromise on tracking speed when the radiation level changes suddenly. Furthermore there are oscillations at its MPP. Further improvement of this technique can be addressed by Advanced Perturb and Observe technique and hence tracking speed can be made faster than the conventional P&O.

REFERENCES

[1] D. K. Sharma and G. Purohit, *Advanced Perturbation and Observation (P&O) based Maximum Power Point Tracking (MPPT) of a Solar Photo-Voltaic System*, IEEE 2012.

[2] Kun Ding, XinGao Bian, HaiHao Liu, *Matlab-Simulink Based Modeling to Study the Influence of Nonuniform Insolation Photovoltaic Array,* IEEE 2011.

[3] Ahmed M. Atallah, Almoataz Y. Abdelaziz, and Raihan S. Jumaah, *Implementation of Perturb and Observe MPPT of PV System with Direct Control Method using Buck and Buck-Boost Converters*, Emerging Trends in Electrical, Electronics & Instrumentation Engineering: An International Journal (EEIEJ), Vol. 1, No. 1, February 2014.

[4] Azadeh Safari and Saad Mekhilef, *Simulation and Hardware Implementation of Incremental Conductance MPPT with Direct control method using Cuk Converter*, IEEE Transactions on Industrial Electronics, VOL. 58, NO. 4, APRIL 2011.

[5] Manoj Kumar, Dr. F. Ansari, Dr. A. K. Jha, *Maximum Power Point Tracking using Perturbation and Observation as well as Incremental Conductance Algorithm*, ISSN: 2294-3905.

[6] Marian Gaiceanu, *MATLAB/Simulink-Based Grid Power Inverter for Renewable Energy Sources Integration*, Volume 3, 2012 Gaiceanu,licensee, InTech.

[7] A. Yafaoui., B. Wu , R. Cheung, *Implementation of Maximum Power point Tracking Algorithm for Residential Photovoltaic Systems*, 2nd Canadian Solar Buildings Conference, Calgary, June 10 – 14, 2007.

[8] Dezso Sera, Laszlo Mathe, Tamas Kerekes, Segiu Viorel, Spataru, Remus Teodorescu, *On- the Perturb and – Observe and Incremental Conductance MPPT Methods for PV Systems*, IEEE JOURNAL OF PHOTOVOLTAICS, VOL., 3, No. 3, JULY 2013.

[9] Tarak Salmi, Mounir Bouzguenda, Adel Gastli, Ahmed Masmoudi, *MATLAB/Simulink Based Modelling of Solar Photovoltaic Cell,* International Journal of Renewable Energy Research, Vol. 2, No. 2, 2012.

[10] Bikram Das et al., *New Perturb and Observe MPPT Algorithm and its Validation using Data from PV Module,* International Journal of Advances in Engineering and Technology, July 2012. ISSN: 2231-1963.

[11] Umashankar Patel et al., *Maximum Power Point Tracking using Perturb and Observe Algorithm and compare with another Algorithm,* IJDACR, Vol. 2, Issue 2, Sept. 2013. ISSN: 2319-4863.

Investigations On The Displacement Control Of APA230L Piezoelectric Actuator

Mokshitha[#1], Rathnamala Rao[#], Muralidhara[*]

[#]*PG Student, Department of Electronics and Communication Engineering*

NMAMIT, Nitte, Karkala, Udupi, Karnataka - 574-110, Affiliated to VTU – Belgaum.
[1]mokshitha1991@gmail.com

[#]*Professor, Department of Electronics and Communication Engineering*

NMAMIT, Nitte, Karkala, Udupi, Karnataka - 574-110, Affiliated to VTU – Belgaum.
[2]malarathna@yahoo.com

,[*]*Professor, Department of mechanical Engineering*

NMAMIT, Nitte, Karkala, Udupi, Karnataka - 574-110, Affiliated to VTU – Belgaum.
[3]mr_kallya@yahoo.com

***Abstract*—A piezoelectric actuator is an electrically controllable positioning element, which functions on the basis of the piezoelectric effect. The piezoelectric actuators transform electrical signals into mechanical displacement and vice versa. The displacement of piezoelectric actuators has a strong nonlinear dependency on voltage which is known as hysteresis. There are several methods for compensating the hysteresis. In this work Bouc-Wen model is used to study the hysteresis behavior and then inverse Bouc-Wen model is used to remove the hysteresis effect. Later Feed forward-Feedback control system is proposed to compensate the hysteresis. A control system includes PID controller to minimize the error in plant output. To check the effectiveness of the model used, it is compared with the compensation model of open loop system. In the present work the model is simulated using Matlab/Simulink for MLA10×10×20 and APA230L piezoelectric actuator for 0.1Hz, 1Hz and 10Hz frequencies.**

***Keywords*— Bouc-Wen model, hysteresis, PID controller, open loop control system, Feedforward-Feedback control system**

I. INTRODUCTION

A piezoelectric actuator converts an electrical signal into a precisely controlled physical displacement. The word Piezoelectric is derived from the Greek word piezein, which means pressure, to squeeze or press [1]. Piezoelectric actuators (PEAs) utilize the inverse piezoelectric effect of piezoelectric materials to generate forces and displacements. It is the ability of certain materials to generate an electric charge or voltage in response to applied mechanical stress or vibrate when voltage is applied [2].

Piezoelectric actuators suffer from some undesirable effects which are responsible for the accuracy of the designed system using piezo actuator. Hysteresis, resonant frequency and creep behaviours of piezoelectric actuator affect the performance such as inaccuracy or oscillation and may lead to instability [3]. Hysteresis is a non-linear phenomenon and can be determined by hysteresis model. Then it is removed using hysteresis compensation model to obtain desired displacement, but it is not straightforward to treat mathematically.

Models for describing the hysteresis nonlinearity characteristics can be divided into physics based model and phenomenological model [4]. Bouc-Wen model which is the simplest model with few parameters has advantage over other hysteresis model and can be applied for real time applications. The inverse of the model is then obtained and subsequently used in a Feed-forward scheme to compensate for this nonlinearity. Compensation method can be divided into two methods. Open loop control which does not require sensor [5] and close loop feedback control which require sensor [6].

Many methods in literature are proposed to compensate hysteresis [7] - [10]. Control system can be modified to get the good response. Feed-forward control loop can be associated with feedback control loop to effectively diminish the hysteresis effect [11]. PID control is the most common control algorithm used in industry and is widely accepted. It is one of the early control strategies and has a simple control structure which operates on plant to produce the correct response. Thus by using inverse Bouc-Wen model in feed-forward loop and PID controller in feedback loop, control system can be designed to nullify the effect of hysteresis.

II. PIEZOELECTRIC ACTUATOR MODEL

Bouc-wen model is a simple model and can match the behaviour of a wide class of hysteresis systems. As it can be easily implemented in real time, it has been extensively adopted in many engineering fields to represent the hysteresis behaviour of engineering elements and structures.

A. Forward model of piezoelectric actuator[12]

Bouc –Wen model can be described by a non-linear differential equation as

$$m\ddot{x} + b\dot{x} + kx = k(du - h) \quad (1)$$

$$\dot{h} = \alpha d\dot{u} - \beta|\dot{u}|h - \gamma\dot{u}|h| \quad (2)$$

Where u is the input voltage to the piezoelectric actuator

x is the displacement of the piezoelectric actuator

m, b, k, is the effective mass, damping, mechanical stiffness of the piezoelectric actuator

d is effective piezoelectric coefficient

α, β and γ are parameters of the hysteretic loop's magnitude and shape

n controls the smoothness of transition from elastic to plastic region.

h indicates the variable obtained from the hysteretic nonlinear dynamics.

Fig. 1 shows the MLA10×10×20 piezoelectric actuator implemented in Simulink using equation 2 and equation 1 is implemented as shown in Fig. 2.

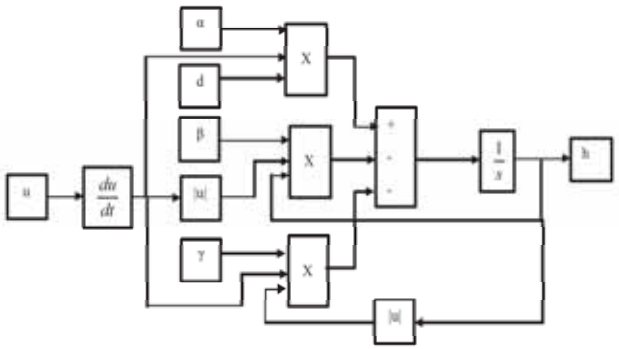

Fig. 1 Bouc-Wen model

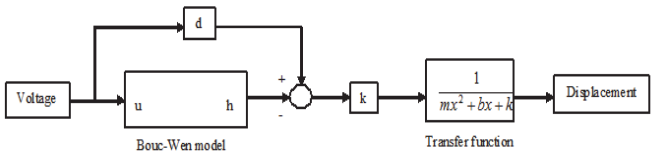

Fig. 2 Forward Bouc-Wen model of hysteresis for MLA10×10×20 piezoactuator

APA230L piezoelectric actuator has 6 stacks of MLA10×10×20 piezoelectric actuator. Thus hysteresis model for APA230L piezoelectric actuator can be obtained by modifying the model of MLA10×10×20 piezoelectric actuator. The APA230L piezoactuator model incorporating hysteresis behaviour is represented by modifying equation 1 and 2 as equation 3 and 4 [12].

$$m\ddot{x} + b\dot{x} + k = k(du - h) - 3k_s \quad (3)$$

$$\dot{h} = \alpha d\dot{u} - \beta|\dot{u}|h - \gamma\dot{u}h \quad (4)$$

The parameters of APA230L piezoelectric actuator is shown in Table I. Fig. 3 represents the Simulink block diagram of equation 3 with an amplifier amplification factor of 4.05.

TABLE 1. PARAMETERS OF APA230L PIEZOELECTRIC ACTUATOR

Parameters	Values	Unit
m	0.0150	Kg
b	150	Ns/m
k	7089000	N/m

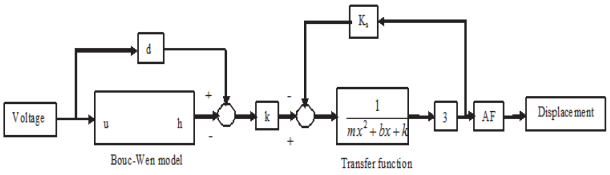

Fig. 3 Forward Bouc-Wen model of hysteresis for APA230L piezoactuator

B. Inverse model of piezoelectric actuator

The forward actuator model describes how actuator responds to the actuating signal. However for the actuator control inverse model is necessary. The inverse model calculates the actuating voltage required for given displacement.

The required voltage for given displacement can be computed by rearranging equation 1 for MLA10×10×20 actuator as given by equation 5 and its implementation is shown in Fig. 4.

$$u = \left(\frac{m}{k \times d}\right)\ddot{x} + \left(\frac{b}{k \times d}\right)\dot{x} + \frac{1}{d}[x + h] \quad (5)$$

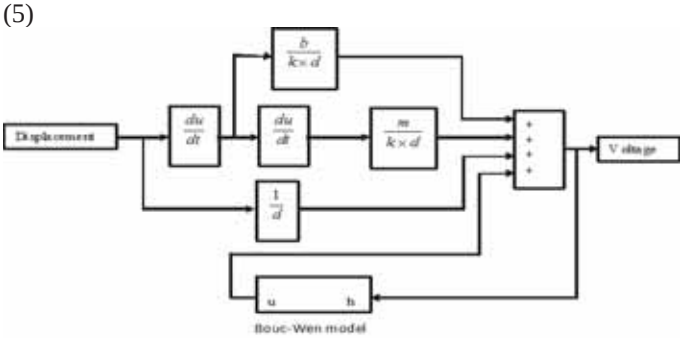

Fig. 4 Inverse Bouc-Wen model for hysteresis compensation (MLA10×10×20 piezoactuator)

Inverse model for APA230L actuator can be designed by rearranging equation 3 which is given in equation 6.

$$u = \left(\frac{m}{k \times d}\right)\ddot{x} + \left(\frac{b}{k \times d}\right)\dot{x} + \left(\frac{1}{d} + \frac{3k_s}{k \times d}\right)x + \left(\frac{h}{d}\right) \quad (6)$$

Equation 6 can be modelled in Matlab/Simulink as shown in Fig. 5.

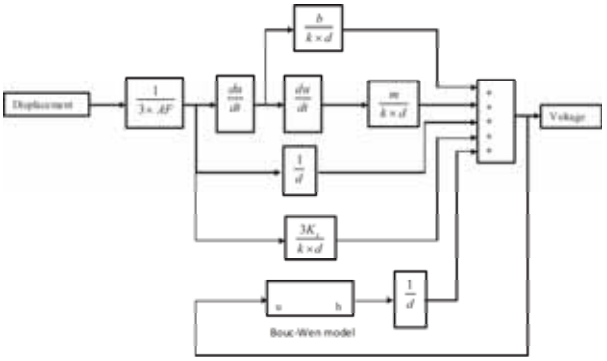

Fig. 5 Inverse Bouc-Wen model for hysteresis compensation (APA230L piezoactuator)

Now control system can be designed which compensate hysteresis for APA230L piezoelectric actuator and produces the desired displacement.

III. HYSTERESIS COMPENSATION MODEL

Compensation model is used to remove the hysteresis effect and get the desired displacement from the plant. Plant in this case is an APA230L piezoelectric actuator. To carry out simulation in Matlab/Simulink, the actuator is replaced with a forward model, wherein, the actuator dynamics are defined with different mathematical equations than that of Bouc-Wen model. In this work PI (Prandtl-Ishlinskii) model is used to represent the actual actuator. Two control systems are designed and effectiveness of the model is compared. These compensation models are then simulated for different frequencies and dependency of the hysteresis model on frequency is studied.

A. Open loop control system

Open loop control system consists of a Feed-forward controller of inverse hysteresis model to remove the hysteresis effect. Therefore inverse Bouc-Wen model shown in Fig. 5 is used in Feed-forward loop. The desired displacement signal is given as input to the inverse Bouc-Wen model, which generates the voltage to drive the piezoelectric actuator. Actuator will then produce the displacement as per the voltage applied to it. The model implemented in Matlab/Simulink is shown in Fig. 6.

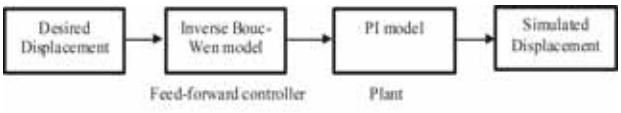

Fig. 6 Open loop control system for hysteresis compensation

B. Feedforward-Feedback control system

This is the modified control system which combines Feed-forward and Feedback loop. The Feed-forward controller makes use of the inverse model of the hysteresis (Bouc-Wen model) and the Feedback controller makes use of conventional PID or lead-lag controller. The desired displacement is given as reference signal and this when applied to the inverse Bouc-Wen model it will produce voltage as output which is later given to plant. The implemented control system is given in Fig. 7.

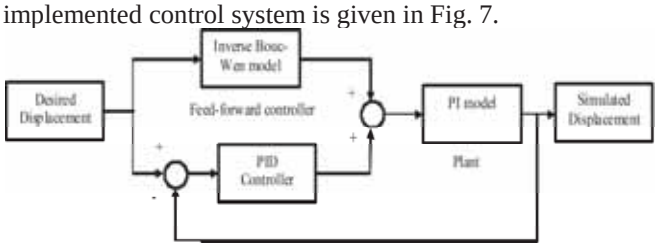

Fig. 7 Feedforward-Feedback control system for hysteresis compensation

Controller used here is a PID controller and this controller algorithm with its three gain terms will generate a response which will help the plant to follow the given reference signal. The input to the PID controller is an error signal which can be defined as difference between the reference signal and the output signal from the plant. Tuning will help to minimize this error.

IV. RESULTS AND DISCUSSION

The experiment is carried out for piezoelectric actuator for sinusoidal voltage of 0 to 150V, at different frequencies to get a displacement of around 19.7 μm for MLA10×10×20 and 230μm for APA230L piezoelectric actuator. Then the designed models (Fig.2-7) are simulated in Matlab/Simulink.

A. Validation of Forward and Inverse Bouc-Wen model

In order to validate the implemented forward and inverse Bouc-wen model, it is simulated in Matlab/Simulink for MLA10×10×20 and APA230L piezoelectric actuator. Initially model parameters have to be estimated from experimental displacement characteristics of MLA10×10×20 piezo actuator. Hence an experiment is conducted at 1Hz frequency to obtain the displacement characteristics and its setup is shown in Fig. 8. The estimated parameters are tabulated in Table II.

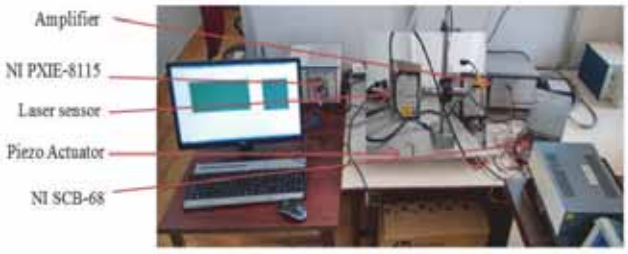

Fig. 8 Experimental setup to obtain displacement data for applied voltage for 1Hz frequency

TABLE 2. ESTIMATED VALUES OF ACTUATOR FOR BOUC-WEN MODEL

Parameters	Values	Unit
m	0.0150	Kg
b	150	Ns/m
k	200000000	N/m
d	1.507e-07	m/V
α	0.2218	-
β	0.0196	-
γ	-0.008	-

Thus the Simulink model shown in Fig. 2 for MLA10×10×20 and Fig. 3 for APA230L actuator can be simulated with the estimated parameters shown in Table II. The simulation results of these forward models are shown in Fig. 9 and Fig. 10.

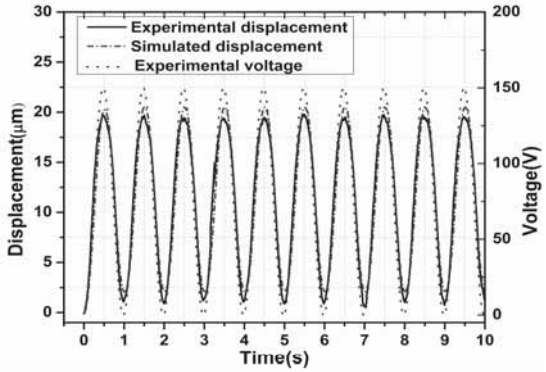

Fig. 9 Comparison of simulated displacement with actual displacement using forward Bouc-Wen model for MLA10×10×20 piezoelectric actuator

As can be seen from the figure forward Bouc-Wen model gives an approximation of actuator displacement for a given input voltage applied to it. Here in the subsequent cycle displacement will not reach zero when voltage reduces to zero. This is due to hysteresis effect. Thus displacement can be reduced to zero if negative voltage is applied to it.

Model shown in Fig. 3 (for APA230L piezoelectric actuator) uses same estimated parameters given in Table II that gives the displacement characteristic with slight mismatch near the peak in comparison to experimental displacement. This can be seen in Fig.10.

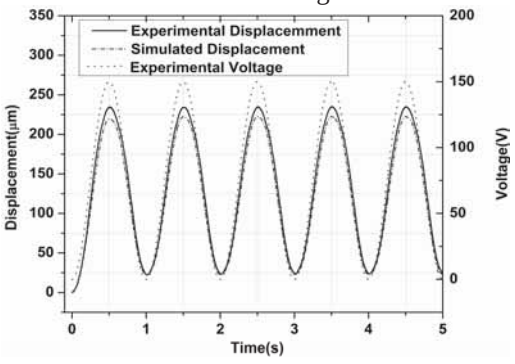

Fig.10 Comparison of simulated displacement with actual displacement using forward Bouc-Wen model for APA230L piezoelectric actuator

In the same way inverse Bouc-Wen model is simulated using inverse model shown in Fig. 4 and Fig 5. Fig. 11 and 12 shows the plot of the voltage calculated by inverse Bouc-Wen model for a reference displacement which is applied to MLA10×10×20 and APA230L piezoelectric actuator. As seen from the figure, for obtaining zero displacement, a negative voltage has to be applied to the actuator.

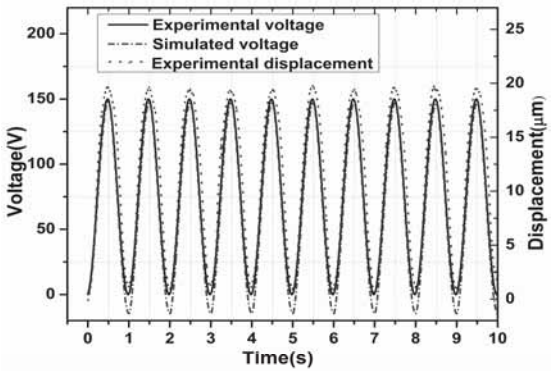

Fig. 11 Actuating voltage calculated using inverse Bouc-Wen model for MLA10×10×20 piezoelectric actuator

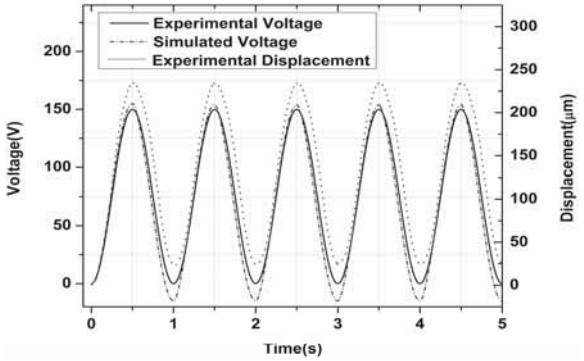

Fig. 12 Actuating voltage calculated using inverse Bouc-Wen model for APA230L piezoelectric actuator

B. Experimental result of compensation model

The compensation model of Fig. 6 is simulated for different frequencies. Fig. 13-15 shows the plot of desired displacement and simulated plant output (i.e. actuator displacement) as a function of time for 0.1Hz, 1Hz and 10 Hz frequency respectively.

As can be seen in Fig. 13 open loop control system gives an error of 9.32% in tracking the desired displacement.

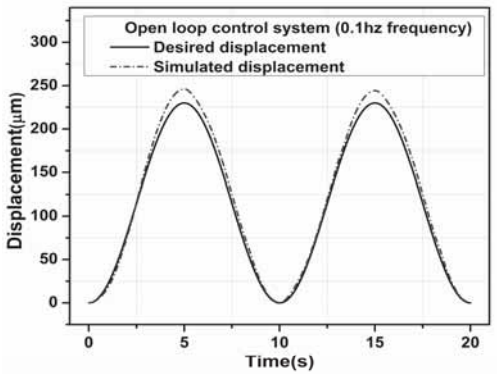

Fig. 13 Simulation result of open loop control system for 0.1Hz frequency

Simulated displacement for 1Hz frequency has an error near peak which can be seen in Fig.14 that has an error of around 9.44%. Similarly tracking error of 10.91% can be seen in Fig.15 which is simulated for 10Hz frequency.

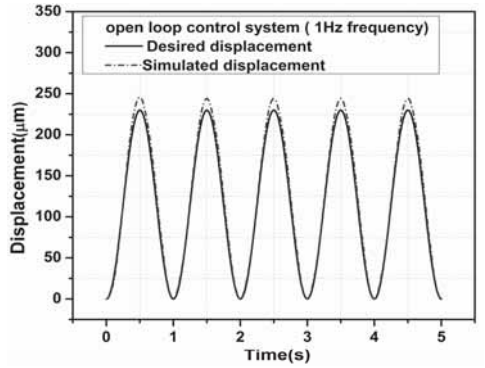

Fig. 14 Simulation result of open loop control system for 1Hz frequency

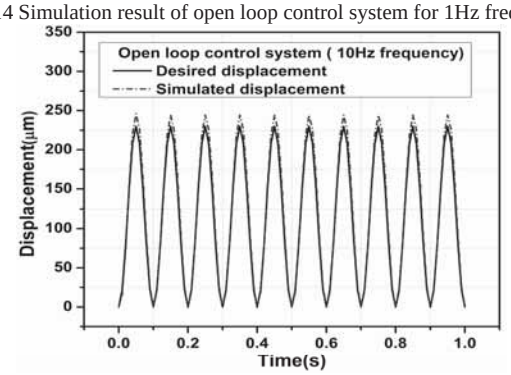

Fig.15 Simulation result of open loop control system for 10Hz frequency

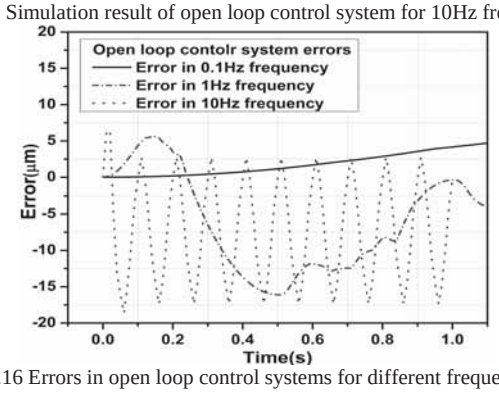

Fig.16 Errors in open loop control systems for different frequencies

The tracking error (i.e. desired displacement–actuator displacement) of a Feed-forward control system (Fig. 6) as a function of time for 0.1Hz, 1Hz and 10Hz frequencies is shown in Fig. 16. The plot shows that increase in frequency increases the tracking error.

The compensation model shown in Fig. 7 has a PID controller in feedback loop. Simulink library browser has a PID controller block which is used in this model as a controller and can be tuned to produce a response and the proper values for three gain terms. Three gain terms are initialized to a value of 1 and tuning is commenced. While tuning if the response produced by the controller is not acceptable, user is allowed to vary the response time and hence can vary the three gain terms as required. The values of controller after tuning are shown in Table III.

TABLE 2. THE GAIN VALUES SET BY THE CONTROLLER AFTER TUNING

Control Parameters	Tuned values
P	15329741.4740764
I	447.768091402849
D	0.000182792263411982

Fig. 17-19 shows the plot of desired displacement and simulated plant output (i.e. actuator displacement) as a function of time with the Feedforward-Feedback control system (Fig. 7) for 0.1Hz, 1Hz and 10Hz frequency respectively.

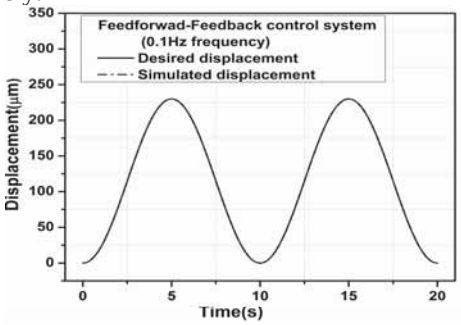

Fig. 17 Simulation result of Feedforward-Feedback control system for

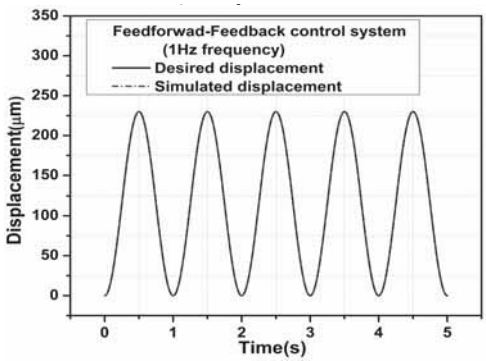

Fig. 18 Simulation result of Feedforward-Feedback control system for 1Hz frequency

PID controller in the feedback loop effectively reduces the error in the simulated displacement. Thus Fig. 17, which is simulation of Fig. 7 for 0.1 Hz frequency gives a small error in tracking the desired displacement and is found to be 0.0000016%. Fig. 7 is simulated for 1Hz frequency which is shown in Fig.18 gives an error of around 0.037% in acquiring the displacement.

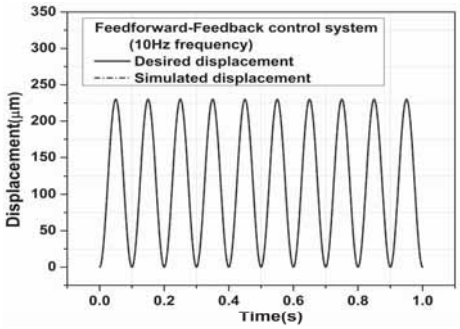

Fig. 19 Simulation result of Feedforward-Feedback control system for 10Hz frequency

In the same way Fig. 19 which is the plot of simulated displacement of Feedforward-Feedback control system for 10Hz frequency tracks the desired displacement with an error of 0.081%. The tracking error of Feedforward-Feedback control system as a function of time for 0.1Hz, 1Hz and 10Hz frequencies are shown in Fig. 20. This shows that Feedforward-Feedback control system gives the desired displacement with a minimum error. Maximum error of 0.081% is found for 10Hz frequency.

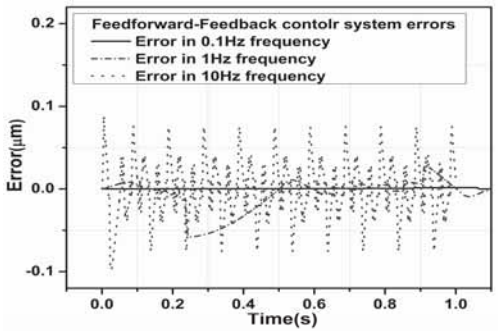

Fig.20 Errors in Feedforward-Feedback control system for different frequencies

Fig. 21-23 shows the comparison of tracking error between open loop and Feedforward-Feedback control system as a function of time for 0.1Hz, 1Hz and 10Hz frequencies respectively. Both open loop and Feedforward-Feedback control system gives a small error for 0.1 Hz frequency which is shown in Fig. 21. Error in open loop control system is approximately 9% more than Feedforward-Feedback control system.

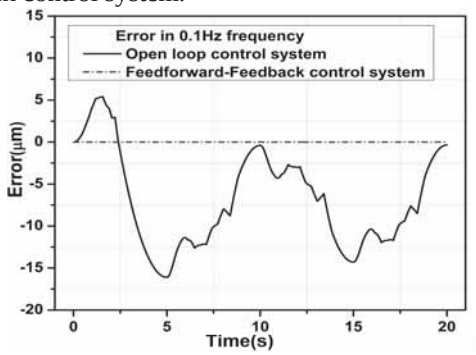

Fig. 21 Error plot for 0.1Hz frequency

Fig. 22 shows the comparison of open and Feedforward-Feedback control system for 1Hz frequency where error is increased compared to simulation of 0.1Hz frequency shown in Fig. 21.

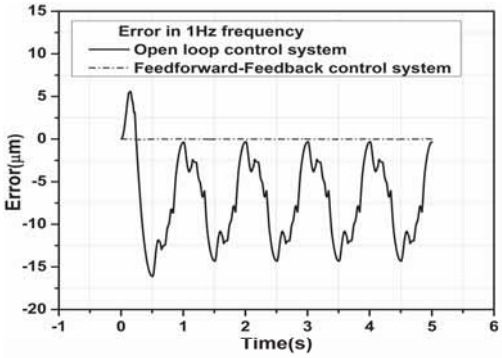

Fig. 22 Error plot for 1Hz frequency

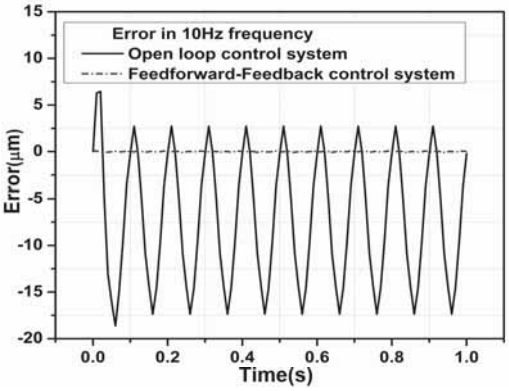

Fig.23 Error plot for 10Hz frequency

Fig. 23 is the tracking error plot of 10Hz frequency for two compensation models (Fig. 6 and Fig. 7). There is 10% increase in error for open loop control system compare to Feedforward-Feedback control system.

As seen from Fig 21-23, the open loop control system induces error in tracking control of actuator. The Feedforward-Feedback control system tracks the desired output accurately. Thus PID controller helps to minimize the error.

The model parameters are estimated for 1Hz frequency. As it is assumed that hysteresis model designed are rate independent, these model are simulated for all frequencies with the same estimated parameters. The percentage error in the two control system for different frequencies is tabulated in Table IV. As can be seen from table, there is a small percentage of tracking error in Feedforward-Feedback control system and also there is an increase in error for 10Hz frequency compare to 0.1Hz and 1Hz in both control systems. This is due to the dependency of model on frequency.

TABLE 4. ERROR IN CONTROL SYSTEM FOR DIFFERENT FREQUENCIES

Frequency (Hz)	**Control system Error(Peak -Peak) (%)**	
	Open-loop	**Feedforward-Feedback**
0.1	9.35	1.69e-3
1	9.44	0.037
10	10.91	0.081

V. CONCLUSIONS

Piezoelectric actuator is widely used in engineering application especially in Nano positioning field. The importance of this actuator is limited by the nonlinear hysteresis. Hence hysteresis compensation is required. This can be implemented using compensation model for hysteresis.

In this work forward Bouc-Wen model is used for characterizing hysteresis behaviour and then designing inverse model to remove the hysteresis effect. This inverse model is used as Feed-forward control and an open loop system is designed to compensate hysteresis. Finally PID controller is used in feedback loop along with Feed-forward system to minimize the error. Both open loop and Feedforward-Feedback control systems are simulated for 0.1Hz, 1Hz and 10 Hz frequencies. The simulation results indicate that the control method overcomes the influence of hysteresis and the closed loop system can give better tracking control of the piezo actuator. Simulation results also show that proposed model depends on frequency which will increase the error as frequency is increased.

REFERENCES

[1] Website[Online]:http://www.robotplatform.com/knowledge/actuators/types_of_actuators.html.

[2] Webste[Online]:http://www.applied-piezo.com/about/piezoelectric-effect.phpn

[3] Website.[Online]:http://en.wikipedia.org/wiki/Hysteresis

[4] Ziqiang Chi and Qingsong Xu, “Recent Advances in the Control of Piezoelectric Actuator,” International Journal of Advanced Robotic System, pp. 1–11, Feb. 2014.

[5] J.A. Dzoleko Dongmo, “Control of an experimental piezoelectric actuators System,” Master’s thesis, Eindhoven University of Technology, Aug. 2010.

[6] http://en.wikipedia.org/wiki/Control_theory

[7] Vahid Hassani, Tegoeh Tjahjowidodo, Thanh Nho Do, “A survey on hysteresis modeling, identification and control,” Mechanical System and Signal Processing, vol. 49, pp. 209-233, Apr. 2014.

[8] Jin-Wei Liang, Hung- Yi Chen, Lung Lin, “Model-Based Control for Piezoelectric-Actuated System using Inverse Prandtle-Ishlinskii Model and Particle Swarm Optimization,” International Journal of Mechanical, Aerospace, Industrial and Mechatronics Engineering, vol. 8, pp. 609–614, 2014.

[9] Chih-Jer Lin and Sheng-Ren Yang, “Precise Positioning of Piezo-Actuated Stages using Hysteresis-Observer Based Control,” Da-yeh University, 2005.

[10] Cunyin Hu and Xianmin Zhang, “Closed-loop Control System of Piezoceramic Actuators with Improved Preisach Model,” in *Proc. World Congrss on Intelligent Control and Autometion*, p. 7385, 2008.

[11] Website.[Online]:https://www.clear.rice.edu/engi128/Handouts/Lec10-Control.pdf

[12] Veeresha R. K., Astron Manoj Touro, Muralidhara, Rathnamala Rao, “Investigation on Open loop Position Control of Amplified Piezoactuator” in *Proc. NSMT*, p. 53, 2000.

A Comparative Study of Securing Visual Cryptographic Shares using Public Key Encryption and Genetic Algorithm

Anisha Maria Coelho Prabhu[#], Pradyumna G.R[*]

[#]*PG Student, Department of Electronics and Communication Engineering*
NMAMIT, Nitte, Karkala, Udupi, Karnataka - 574-110, Affiliated to VTU – Belgaum.
[1]anishamcprabhu@gmail.com

[2]*Assistant Professor, Department of Electronics and Communication Engineering*
NMAMIT, Nitte, Karkala, Udupi, Karnataka - 574-110, Affiliated to VTU – Belgaum.
[2]pradyumnabhat@gmail.com

***Abstract*—Visual Cryptography (VC) is a special type of encryption technique where decryption is done by the Human Visual System (HVS) - the eyes. VC scheme encrypts an image by breaking it down into shares. The shares are then printed on transparencies. Decryption is done by superimposing the shares. Thus one can visually decode the secret image without computation. However, this property makes VC insecure as a third party can easily retrieve the secret information if he obtains the transparencies. The VC shares can be made more secure by encrypting them using Public Key Encryption or Genetic Algorithm. Overlapping these encrypted shares reveals no information about the secret image, increasing the security of the VC scheme.**

***Keywords*—Visual Cryptography, Public Key Encryption, Genetic Algorithm, Information Security.**

I. INTRODUCTION

The Internet has greatly changed humanity's way of life. Digital information and data are being transmitted over the internet more than ever before due to the availability and efficiency of computer networks for the communication of digital information and data. Digital images, video and audio can be captured, stored, transmitted and even manipulated, earning them a role in a variety of fields. Distortion free transmission, compact storage and easy editing has generated many benefits for digital multimedia field along with the various facilities being available for storing, transmitting and accessing the data.

Increasing access to the Internet and networks has a great impact on one's day to day life. Humans are more dependent on computer systems and networks more than ever before. There is an increase in the amount of information being stored and transmitted. This dependency has brought many threats to information security. The computer attacks and break-ins are increasing. Storing multiple copies of important and sensitive information gives a greater chance to intruders to access it. On the other hand, having only one copy of this information means it cannot be retrieved if it is destroyed during an attack. Hence, there is a great need to handle information in a secure and reliable way.

Secret sharing is a good solution to this problem. Secret sharing or secret splitting refers to a method for distributing a secret among a group of participants, each of whom is allocated a share of the secret. The secret is reconstructed only when all or a sufficient number of shares are combined together. No information is conveyed by individual shares. Thus, intruders need to obtain the sufficient amount of shares to retrieve the information or destroy all the shares if they are seeking to destroy the information.

Visual Cryptography (VC) is a special type of encryption technique where the decryption is done by the Human Visual System (HVS) without any computation. This technique was proposed by Naor and Shamir [1] in 1994. According to them VC is a scheme where a secret image is broken down into *n* shares and printed on transparencies. Only when *n* transparencies were stacked one above the other the secret was revealed, while any *n*-1 shares revealed no information about the original image. Here, there is no need for any complicated computations in order to get back the image, rather it is just done by superimposing the shares.

Since one can visually decode the secret image without computation, VC isn't secure as a third person can easily retrieve the secret image if he obtains the transparencies or if the shares are passing in sequence over the network. Thus, there is a need to secure the shares before sending them over a network or printing them.

This paper aims at securing the VC shares using public key encryption and Genetic Algorithm (GA).

II. RELATED WORK

Various researches have been carried out to improve the security of the VC shares and to prevent unauthorized use of information:

Kandar *et al.* [2] proposed a scheme where a given secret image was broken down into *n* shares and then these *n* shares were embedded into *n* envelope images using LSB

replacement. The secret image was recovered by retrieving the shares from the LSB of the envelope images and then performing the OR operation. Since the shares are embedded into meaningful envelope images a hacker will not notice the presence of the shares. However using *n* envelope images increases the memory and bandwidth requirement.

Liu *et al.* [3] suggested a scheme which shared a colour secret image over (*n*-1) arbitrary natural images and one noise-like share image. Instead of altering the contents of natural images, the encryption process extracted feature images from each natural image. Feature extraction was carried out on the (*n*-1) natural images and then bitwise XOR was performed on the (*n*-1) feature images and the secret image to obtain (*n*-1) share images and one noise-like image. Upon reception of the *n* sharing images, decryption end separately extracted feature image from the natural sharing images. Then the (*n*-1) feature images and received noise-like share image was decrypted to obtain the secret image. This approach effectively reduced the transmission risk and made it possible to recover secret images without any distortion. However, the use of (*n*-1) natural images increases storage requirement and also an extra overload on the network.

Nakajima and Yamaguchi [4] proposed a new method of VC for natural images. This paper presented a system which took three images as inputs where one was the secret image and the other two were used for encryption. The encryption process consisted of determining the arrangement of transparent sub-pixels on each of the three images. The two output images were printed on transparencies and stacked together to obtain the secret image. The drawback of this scheme is the deterioration of the image quality of the revealed image.

Sharma *et al.* [5] enhanced the security in VC systems by using Cover Image Share Embedded Security Algorithm (CISEA). Here they first generated the two share images (X1 and X2) of the secret image using VC. Next a cover image C was selected and embedded images were generated with the help of compliment images (C1 and C2) of this cover image. Then four embedded images (X11, X12, X21, X22) to be transmitted were generated. These embedded images were generated by embedding shares X1 and X2 into both the compliments of the cover image. Visual decryption was done by the human visual system without any complex computation. The images in which the shares were embedded were simply stacked over each other to get back the original secret image. Even though this technique provides more security than when water marking is used it still poses a danger that the secret image maybe revealed if hackers find all the shares and overlap them.

It has thus been observed that VC does not secure the shares. The schemes that used cover images to carry the secret information resulted in overload to the network and required extra storage space. Yet, in other techniques the quality of recovered images was very poor. All these limitations led to finding an alternate way to enhance the security of VC.

III. Algorithms Used

A. Visual Cryptography

VC is a special type of encryption method where the decryption is done by the HVS, the eyes. No complex computation is required for the decryption as it is done by the eyes. VC was introduced by Naor and Shamir in 1994 [1]. It is a type of secret sharing scheme used for the encryption of images. Secret sharing is a method where a secret can be distributed among a group of participants, where each participant only gets a share of the secret. These individual shares reveal no information; but when all shares are combined together, the secret can be reconstructed.

k-out-of-*n* or (*k*,*n*) is a general scheme of visual cryptography, where *k* is the threshold and *n* is the number of shares. Here, a secret image is cryptographically encoded into *n* random shares. These *n* shares are meaningless images that are then printed on transparencies and can be distributed among *n* participants. No participant has any knowledge about another's share. Also, as the shares are randomly generated, one participant cannot predict any other share. Any *k* or more participants can reconstruct the secret image by superimposing the *k* transparencies together. *k-1* or fewer participants cannot gain any information about the secret, despite having infinite computational power. If *k*=*n*, i.e., *n*-out-of-*n* scheme, all shares are needed to successfully reconstruct the secret.

1) VC Scheme (2 sub-pixels): The simplest VC scheme is the (2,2) visual threshold scheme, where for every pixel *p* in the secret binary image, a pair of black and white sub-pixels are generated in each of the two share images. If *p* is black, one of the two columns under the black pixel in Fig. 1 is selected. If *p* is white, one of the two columns under the white pixel is selected. The column is randomly selected and each column has 0.5 probability of being chosen. Then, the first pair of sub-pixels in the selected column is assigned to share 1 and the second pair of sub-pixels in the column is assigned to share 2. Irrespective of whether a pixel is black or white, the pixel *p* is encoded into a black-white or white-black pair of sub-pixels of equal probability. Thus an individual share gives no clues as to whether the pixel *p* is black or white. Also, as each pixel is independently encoded, a group of pixels can reveal no information about the value of *p*. The superposition of the two shares is as shown in the last row of Fig. 1. If the pixel *p* is black, the superimposition yields two black sub-pixels. If the pixel *p* is white, the output is one black and one white sub-pixel irrespective of the column being chosen during encoding. The decoded pixel is clearly visible, although some contrast loss is observed [6], [7].

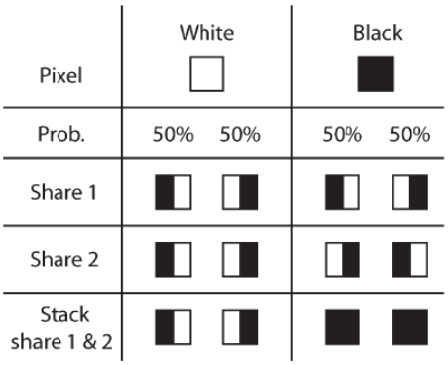

Fig. 1: (2,2) Visual cryptography scheme; a secret pixel is encoded into two sub-pixels in each of the two shares.

Mathematically, the white pixel is represented by 1 and the black pixel by 0. For (2,2) VC scheme, the basis matrices S^0 and S^1 are as follows:

$$S^0 = \begin{bmatrix}1 & 0\\ 0 & 1\end{bmatrix} \qquad S^1 = \begin{bmatrix}1 & 0\\ 1 & 0\end{bmatrix}.$$

There are two collection of matrices, C^0 for encoding black pixels and C^1 for encoding white pixels. They are formed by permuting the columns of basis matrices as follows:

C^0=

$$\left\{\text{Matrices obtained by permuting the columns of } \begin{bmatrix}1 & 0\\ 0 & 1\end{bmatrix}\right\}$$

C^1=

$$\left\{\text{Matrices obtained by permuting the columns of } \begin{bmatrix}1 & 0\\ 1 & 0\end{bmatrix}\right\}.$$

That is,

$$C^0 = \left\{\begin{bmatrix}1 & 0\\ 0 & 1\end{bmatrix}, \begin{bmatrix}0 & 1\\ 1 & 0\end{bmatrix}\right\} \text{ and}$$

$$C^1 = \left\{\begin{bmatrix}1 & 0\\ 1 & 0\end{bmatrix}, \begin{bmatrix}0 & 1\\ 0 & 1\end{bmatrix}\right\}.$$

To share a black pixel, one of the matrices in C^0 is randomly selected, and to share a white pixel, one of the matrices in C^1 is randomly selected. The first row of the chosen matrix is used for share 1 and the second is used for share 2 [7], [8].

(2,2) VC scheme with two sub-pixels can be illustrated with an example as shown in Fig. 2. The secret image in (a) is encoded into two shares (b) and (c). The secret is retrieved by superimposing the two shares as shown in (d). This decoded image has some contrast loss, however, the secret is easily identified. Some pixels appear 'grey' due to the shrinking of the image for viewing purpose. Since each pixel is encoded into two sub-pixels, the width of the secret image is twice that of the original image. This effect is referred to as *pixel expansion*.

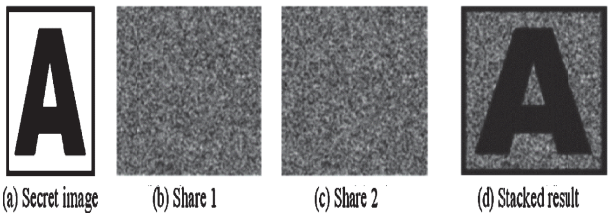

Fig. 2: Example for (2,2) visual cryptography scheme with two sub-pixels.

B. Public Key Encryption

Public-key cryptography is also known as asymmetric-key to distinguish it from the symmetric-key cryptography. Symmetric-key cryptography is a mechanism where the same key is used for encryption and decryption. It is similar to the locking and unlocking of a door where a single key is used for both. Since only one key is used, this mechanism requires a very strong and sophisticated mechanism to distribute this secret key to the two parties involved in communication. On the other hand, public-key cryptography uses key pairs: one for encrypting, called public-key and the other for decrypting, called private-key. This a clever and attractive approach and has the following advantages over symmetric-key:

- Simplified key distribution
- Digital signature
- Long-term encryption.

1) RSA Crypto-system: RSA is one of the first practicable public-key cryptosystems and it is widely used for secure transmission. RSA stands for Ron Rivest, Adi Shamir and Leonard Adleman who first publicly described the algorithm in 1977. RSA algorithm has three main steps: key generation, encryption and decryption.

a) Key Generation: The key pair for RSA algorithm is generated as follows:

1. Choose two distinct prime numbers p and q.
2. Compute $n = pq$.
3. Compute $\varphi(n) = (p-1)(q-1)$, where φ is Euler's totient function.
4. Choose an integer e such that $1 < e < \varphi(n)$ and e and $\varphi(n)$ are co-prime i.e., $\gcd(e,\varphi(n)) = 1$.
5. Determine d as $d \equiv e^{-1} \pmod{\varphi(n)}$ i.e., d is the multiplicative inverse of e modulo $\varphi(n)$.

The public key constitutes of the modulus n and the public (or encryption) exponent e. The private key consists of the modulus n and the private (or decryption) exponent d which is kept secret. p, q and $\varphi(n)$ are also to be kept secret as they can be used to calculate d.

b) Encryption: Alice transmits her public key (n,e) to Bob and keeps the private key d secret. Now Bob wishes to send a message to Alice. He coverts the message M into an integer m. Next he encrypts the message to get the ciphertext c as

$$c \equiv m^e \pmod{n} \quad (1)$$

This ciphertext c is then transmitted to Alice.

c) Decryption: On receiving c Alice can use her private key exponent d to obtain m as

$$m \equiv c^d \pmod{n} \quad (2)$$

Once m is computed, she can obtain the message by converting it back to text [9].

C. Genetic Algorithm

Genetic algorithm is a search technique used to find solutions to optimization and search problems. GAs were invented by John Holland in the 1960s and were developed

by Holland and his students and colleagues at the University of Michigan in the 1960s and the 1970s.

The algorithm first creates an initial population of possible solutions to the problem and lets them evolve over multiple generations to find better and better solutions. The new population is used in the next iteration of the algorithm. The algorithm terminates when either a maximum number of generations has been produced, or a satisfactory fitness level has been reached for the population [10].

The new population is generated using two main processes:

1) Crossover: Crossover is when vector entries from a pair of individuals in the current population are combined to form a child. Crossover using individuals from current population to create two offsprings who have characteristics of both parents. For example, parent1 is 111***01***011 and parent2 is 010***11***010. After crossover the offspring produced are 111***11***011 and 010***01***010.

2) Mutation: Mutation is when a child is created by applying random changes to one individual in the current population. An individual may or may not undergo mutation and the points at which it mutates is random. Two individuals before and after mutation are as shown:

Original Offspring1: 01001010
Mutated Offsprng1: 01***1***0101***1***
Original Offspring2: 00010100
Mutated Offsprng2: 0***1***010100 [11].

IV. Proposed System

The proposed scheme, as shown in Fig. 3, first generates shares of the Secret Binary Image using (2,2) VC Scheme. In the next step, either RSA algorithm or GA, is used to encrypt the generated shares in order to make them more secure and prevent duplication or unauthorized access of information. At the receiving end, the shares are decrypted using RSA or GA decryption algorithm and the decrypted shares are stacked together to obtain the secret image. The entire process can be divided into four main phases.

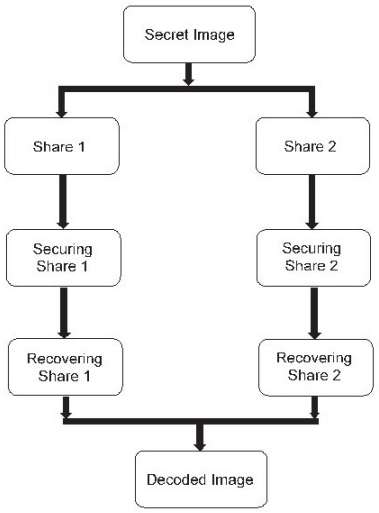

Fig. 3: Methodology or structure of the proposed scheme

A. PHASE 1 – Generating shares of secret image

VC Encryption is implemented in this phase. Here (2,2) VC scheme is used generate shares of the secret binary image. Each pixel in the secret image is replaced by four sub-pixels, two sub-pixels in each share. The sub-pixels are randomly chosen with respect to the encoding scheme shown in Fig. 1.

B. PHASE 2 – Encrypting the generated Shares

The second phase deals with encrypting the shares generated in Phase 1 by using RSA or GA. First the key for encryption is generated and the shares are encrypted using this key. The output of this stage is the two encrypted shares.

C. PHASE 3 – Decrypting the Shares

This phase takes place at the destination of the secret image. RSA or GA decryption is performed on the received shares to obtain the shares in their original form.

D. PHASE 4 - VC decryption

In this phase the secret image is got back by performing VC decryption. The two shares are overlapped by performing AND operation on the decrypted shares in order to retrieve the secret image.

V. Results and Discussions

The proposed scheme is implemented in MATLAB 8.3. The entire process with RSA as the encryption algorithm is shown in Fig 4. Whereas, Fig. 5 shows the images produced using GA as the encryption algorithm.

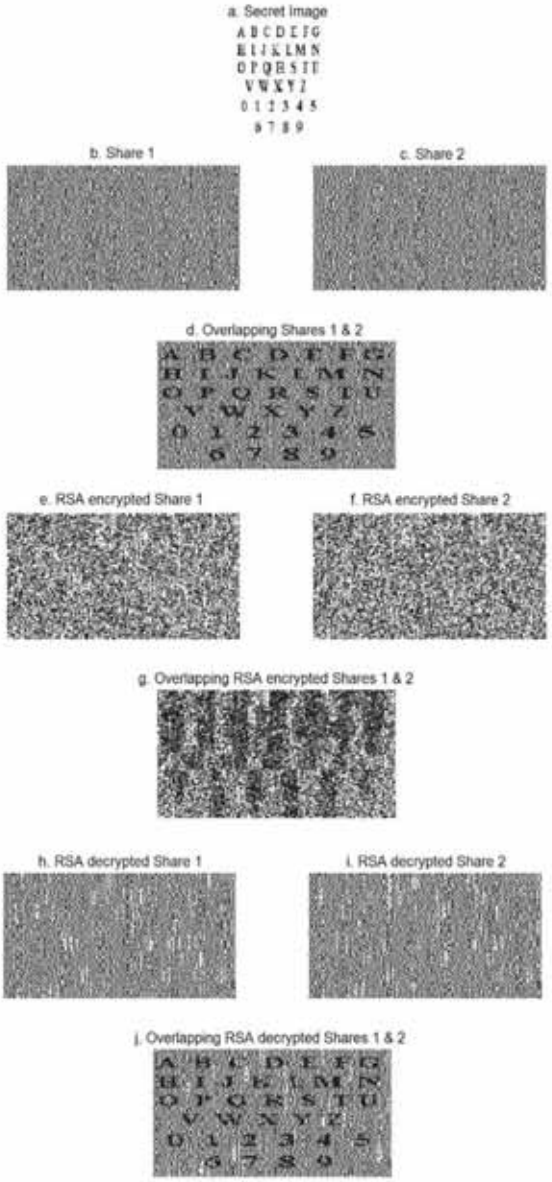

Fig. 4: Securing visual cryptographic shares using RSA algorithm

A secret binary image of size 128x128, shown by 'a' in Fig.4 and Fig. 5, is taken as input, (2,2) VC is performed in order to obtain the two shares of the secret image, denoted by 'b' and 'c' in the figures. The two shares should reveal the secret image on overlapping as shown in 'd'. Next, the two shares are encrypted using RSA or GA. First the keys are generated and then the two shares are encrypted. In the figures, 'e' and 'f' are the encrypted shared. It can be observed from 'g' in figures that overlapping the two encrypted shares revealed no information about the secret image. Thus an opponent cannot obtain the secret image without the secret key. On obtaining the encrypted shares at the receiving end, RSA or GA decryption is performed on them in order to obtain the original shares. First the key for decryption are generated and then the shares are decrypted using this key. Once the original shares, shown in 'h' and 'i' are obtained, VC decryption is performed using AND operation on the shares in order to obtain the original image back, shown in 'j' in Fig.4 and Fig. 5.

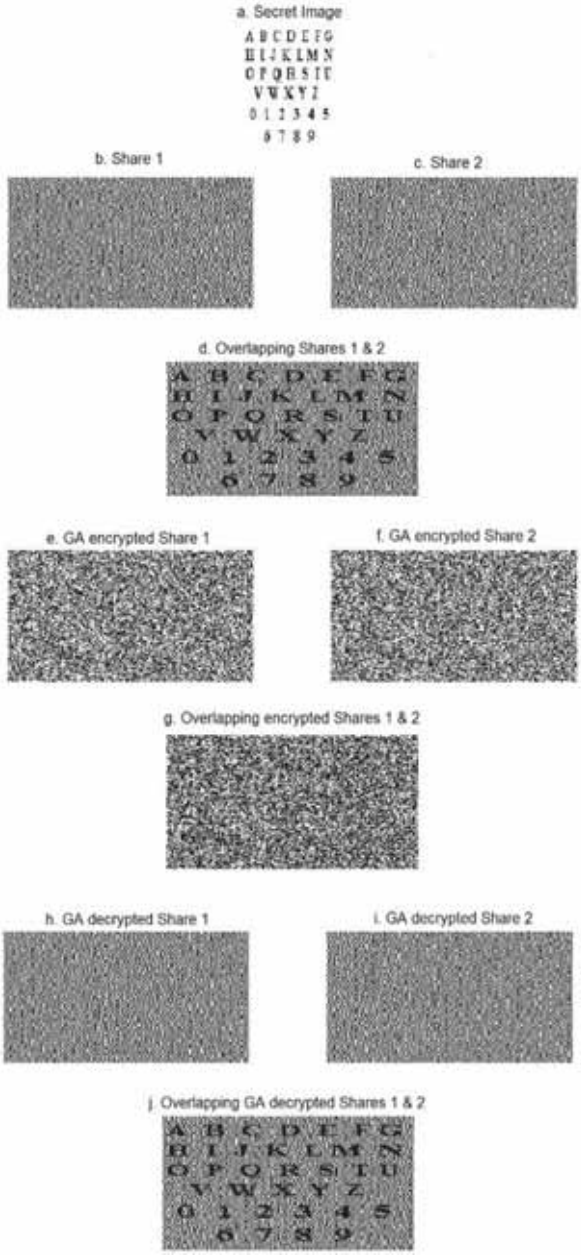

Fig. 5: Securing visual cryptographic shares using genetic algorithm

The system performance in terms of time taken for encryption and decryption for images of different sizes, using RSA is shown in Table I and GA in Table II. It is visually represented in Fig. 6 and Fig. 7 respectively.

TABLE I

SYSTEM PERFORMANCE USING RSA

Image Size	Key Length	Time Taken (s)		
		VC	Encryption	Decryption
64x64	16	0.109	220.856	220.029
	32		231.079	230.831
	64		248.196	285.827
128x128	16	0.375	1079.480	1101.569
	32		1096.761	1129.346
	64		1134.944	1161.262
256x256	16	1.885	4250.425	4150.933
	32		4323.340	4283.119
	64		4396.375	4341.327

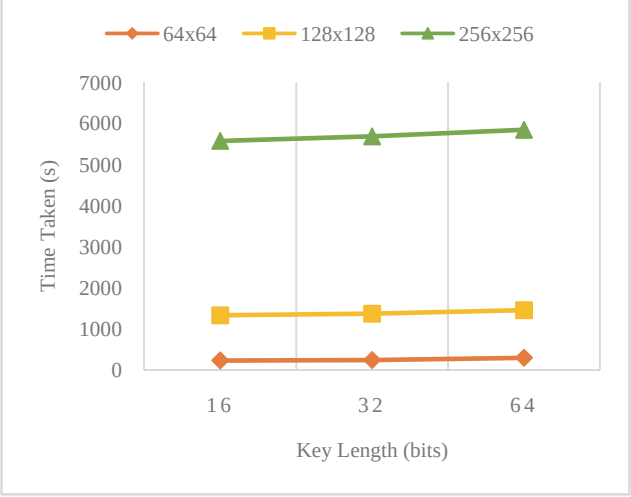

Fig. 6: Time taken for encryption using RSA algorithm for various sized images with different key lengths

The time taken for encryption and decryption varies only a little as the key length is increased. Hence, the system is secure as lager key lengths provide better security for the same time requirement. However, as the size of the image increases, the time taken for encryption increases greatly. This can be observed in Table I and Fig. 6. This large time requirement is infeasible.

TABLE II

SYSTEM PERFORMANCE USING GA

Image Size	Key Length (bits)	Time Taken (s)		
		VC	Encryption	Decryption
128x128	16	0.391	26.854	27.349
	64		8.072	8.019
	256		4.164	3.813
	1024		2.903	2.847
256x256	16	1.424	109.553	106.533
	64		33.663	34.540
	256		15.337	16.258
	1024		13.731	14.053
512x512	16	6.359	417.126	430.655
	64		150.306	152.051
	256		72.574	72.058
	1024		56.782	56.441

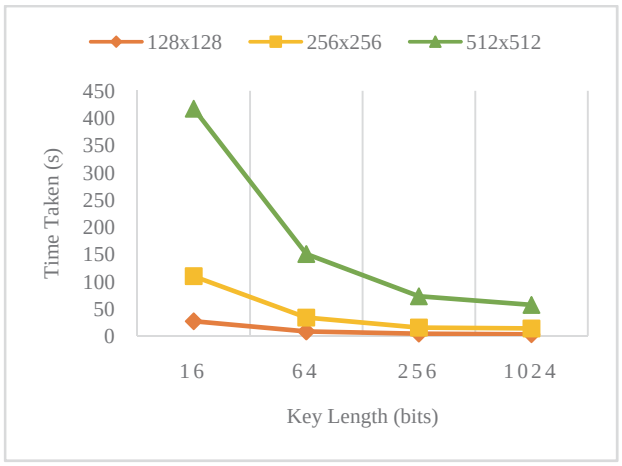

Fig. 7: Time taken for encryption using genetic algorithm for various sized images with different key lengths

From Table II and Fig. 7 it can be observed that as the size of the image increases, the time taken for VC, encryption and decryption increases as in the case of RSA. However, the time requirement isn't as great as in the case of RSA. Also, when GA is used, the time taken for encryption and decryption reduces with the increase in key length. Larger key lengths provide more security. Thus, GA provides a faster crypto-system with larger key lengths.

VI. Conclusion

Visual Cryptography is a simple algorithm which can be used to encrypt documents or images. It has a lower computational cost as decryption is done by the eyes and there is no need for a decryption algorithm. This advantage can however turn into a drawback if a hacker comes across both the shares as he has to only overlap the two to recover the secret image. Securing these shares using RSA or GA prevents the hackers from obtaining information by simply overlapping the shares. Even if he obtains the two secured shares and overlaps them he will not be able to retrieve the secret information. This scheme does not have large memory or bandwidth requirement as it doesn't use any cover images. The image quality of the retrieved image is of a visually acceptable level. Comparing the two methods, it can be observed that GA can provide better security with a smaller time requirement.

The system can be further improved by

- Implementing it for coloured images.
- Implementing it for various image formats.
- Using a more sophisticated public key cryptosystem for faster encryption.

References

[1] M. Naor and A. Shamir, "Visual cryptography", Advances in Cryptology EUROCRYPT '94, Lecture Notes in Computer Science, vol. 950, pp. 1-12, 1995.

[2] Shyamalendu Kandar, Arnab Maiti and Bibhas Chandra Dhara, "Visual cryptography scheme for colour image using random number with enveloping by digital watermarking", IJCSI International Journal of Computer Science Issues, vol. 8, issue 3, no. 1, pp. 543-549, 2011.

[3] Xiao-Yi Liu, Ming-Song Chen and Ya-Li Zhang, "A new colour visual cryptography scheme with perfect contrast", 2013 8th International ICST Conference on Communications and Networking in China, pp. 449-454, 2013.

[4] Mizuho Nakajima and Yasushi Yamaguchi, "Extended visual cryptography for natural images", Department of Computer Science, University of Toronto, 2002.

[5] Himanshu Sharma, Neeraj Kumar and Govind Kumar Jha, "Enhancement of security in visual cryptographic system using cover image share embedded security algorithm (CISEA)", 2011 2nd International Conference on Computer and Communication Technology, IEEE, pp. 462-467, 2011.

[6] Zhi Zhou, Gonzalo R. Arce and Giovanni Di Crescenzo, "Halftone visual cryptography", IEEE Transactions on Image Processing, vol. 15, issue 8, pp. 2441-2453, 2006.

[7] Nitty Sarah Alex and L. Jani Anbarasi, "Enhanced image secret sharing via error diffusion in halftone visual cryptography", 2011 3rd International Conference on Electronics Computer Technology (ICECT), pp. 393-397, 2011.

[8] Thomas Monoth and Babu Anto P, "Contrast-enhanced visual cryptography scheme based on additional pixel patterns", 2010 International Conference on Cyberworlds, pp. 171-178, 2010.

[9] William Stallings, "Cryptography and network security", 5th ed., Pearson, 2010, pp. 266-299.

[10] Melanie Mitchell, "An introduction to genetic algorithms", 1st ed., 1998, pp. 8-10.

[11] Scott M. Thede, "An introduction to genetic algorithms", Journal of Computing Sciences in Colleges, vol. 20, issue 1, pp. 115-123, 2004.

GUIDELINES FOR AUTHORS

The contributors are expected to highlight their research work with sufficient details & discussion of results.

The original research paper should be limited to 6 and short communication to 3 printed pages of the journal in double column standard IEEE format. Please refer to IEEE website for the standard format.

Manuscripts must be submitted online to nmamit.arj@gmail.com in .docx format.

Enough precaution should be taken to make the manuscript error free.

The papers that are not in the standard format may be rejected

Submission of an article implies that the work described has not been published previously (except in the form of an abstract or as part of a published lecture or academic thesis), that it is not under consideration for publication elsewhere, that its publication is approved by all authors and tacitly or explicitly by the responsible authorities where the work was carried out.

Authors of the selected papers have to send the final camera ready paper (both in MS Word &PDF) for final print

After the review process, the selected papers will be published in the Journal.

Article structure

Subdivision - numbered sections

Divide your article into clearly defined and numbered sections. Subsections should be numbered 1.1 (then 1.1.1, 1.1.2, ...), 1.2, etc. (the abstract is not included in section numbering). Use this numbering also for internal cross-referencing: do not just refer to 'the text'. Any subsection may be given a brief heading. Each heading should appear on its own separate line.

Introduction

State the objectives of the work and provide an adequate background, avoiding a detailed literature survey or a summary of the results.

Material and methods

Provide sufficient detail to allow the work to be reproduced. Methods already published should be indicated by a reference: only relevant modifications should be described.

Theory/calculation

A Theory section should extend, not repeat, the background to the article already dealt with in the Introduction and lay the foundation for further work. In contrast, a calculation section represents a practical development from a theoretical basis.

Results

Results should be clear and concise.

Discussion

This should explore the significance of the results of the work, not repeat them. A combined Results and Discussion section is often appropriate. Avoid extensive citations and discussion of published literature.

Conclusion

The main conclusions of the study may be presented in a short Conclusions section, which may stand alone or form a subsection of a Discussion or Results and Discussion section.

Appendices

If there is more than one appendix, they should be identified as A, B, etc. Formulae and equations in appendices should be given separate numbering: Eq. (A.1), Eq. (A.2), etc.; in a subsequent appendix, Eq. (B.1) and so on. Similarly for tables and figures: Table A.1; Fig. A.s1, etc.

NMAM INSTITUTE OF TECHNOLOGY, NITTE – 574110

NMAM Institute of Technology was started in the year 1986, as a part of Nitte Education Trust, Mangalore and is celebrated its Silver Jubilee in 2011. The Institute is named in fond memory of Nitte Mahalinga Adyanthaya, a distinguished engineer of the district. It is affiliated to the Visvesvaraya Technological University, Belgaum, enjoying academic autonomy and is recognized by the All India Council for Technical Education, New Delhi. It is accredited by the National Board for Accreditation and is certified to the ISO 9001 – 2008 standards for quality education by KEMA, Netherlands. The Institute has been recognized as Lead Institute under TEQIP- I Project of World Bank.

The Institute offers B.E, M.Tech and Ph.D pragrammes in various Engineering and Technology disciplines. The graduate programs comprise of 7 branches of Engineering – Electronics & Communication Engineering, Computer Science & Engineeing, Civil Engineering, Electrical & Electronics Engineering, Information Science & Engineering, Bio-Technology and Mechanical Engineering. The Institute's postgraduate programs include, Master of Technology in five disciplines, Master of Computer Applications and Master of Business Administration. The Visvesvaraya Technological University has opened a postgraduate extension centre at NMAMIT, offering M.Tech in Micro-electronics & Control Systems. Besides these, students also pursue their M.Sc(Eng.) and Doctoral Programs at the Institute. The Institute got academic autonomy in the year 2007, bringing in the much needed flexibility to innovate in terms of curriculum, education delivery and evaluation. Institute entered into collaboration with Penn State University, Harrisburg, USA and started offering 2+2 twinning program in Engineering since 2011.